Cell Reports
Physical Science

CellPress
OPEN ACCESS

Article

SARS-CoV-2 evolved variants optimize binding to cellular glycocalyx

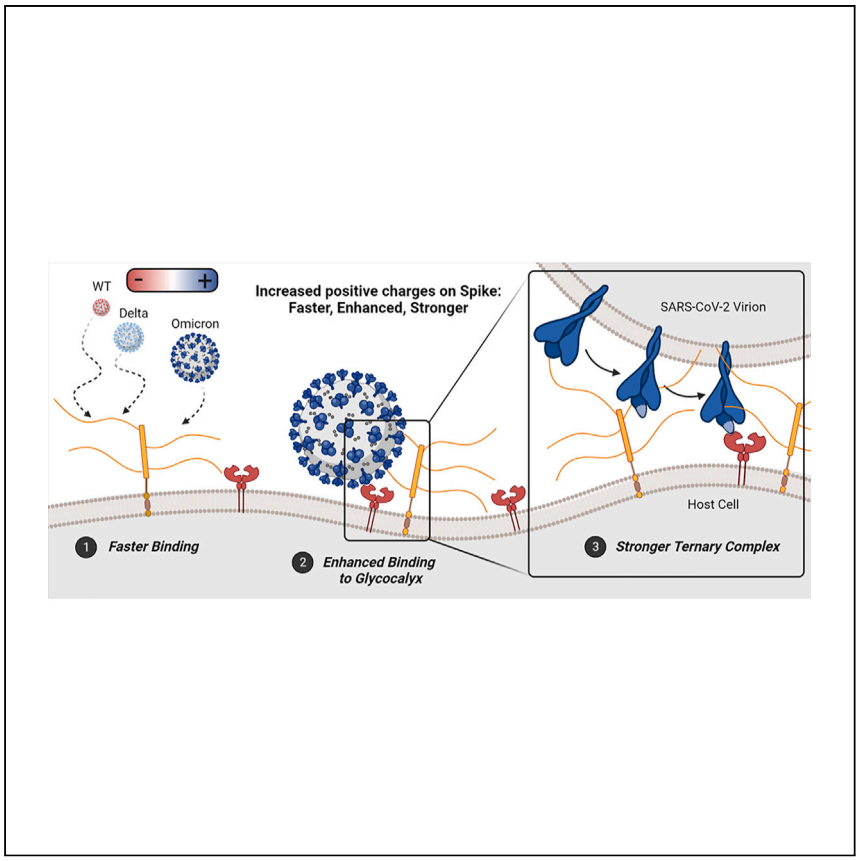

Kim et al. uncover how SARS-CoV-2 variants evolve to be more dependent on heparan sulfate in viral attachment and infection. A combination of computational and experimental techniques reveal that increased positive charge on spike proteins leads to enhanced binding to heparan sulfate, informing the design of rapid diagnostics for COVID.

Sang Hoon Kim, Fiona L. Kearns, Mia A. Rosenfeld, ..., Micah Papanikolas, Rommie E. Amaro, Ronit Freeman

ramaro@ucsd.edu (R.E.A.)
ronifree@email.unc.edu (R.F.)

Highlights

SARS-CoV-2 spike proteins evolve to have increased and remapped positive charges

Omicron spike interactions with heparan sulfate are significantly enhanced

Omicron spike stabilizes formation of a spike-heparan sulfate-ACE2 ternary complex

Spike binding to heparan sulfate and ACE2 is leveraged to rapidly detect all variants

Kim et al., Cell Reports Physical Science 4, 101346
April 19, 2023
https://doi.org/10.1016/j.xcrp.2023.101346

Cell Reports
Physical Science

CellPress
OPEN ACCESS

Article

SARS-CoV-2 evolved variants optimize binding to cellular glycocalyx

Sang Hoon Kim,[1,3] Fiona L. Kearns,[2,3] Mia A. Rosenfeld,[2,3] Lane Votapka,[2] Lorenzo Casalino,[2] Micah Papanikolas,[1] Rommie E. Amaro,[2,*] and Ronit Freeman[1,4,*]

SUMMARY

Viral variants of concern continue to arise for SARS-CoV-2, potentially impacting both methods for detection and mechanisms of action. Here, we investigate the effect of an evolving spike positive charge in SARS-CoV-2 variants and subsequent interactions with heparan sulfate and the angiotensin converting enzyme 2 (ACE2) in the glycocalyx. We show that the positively charged Omicron variant evolved enhanced binding rates to the negatively charged glycocalyx. Moreover, we discover that while the Omicron spike-ACE2 affinity is comparable to that of the Delta variant, the Omicron spike interactions with heparan sulfate are significantly enhanced, giving rise to a ternary complex of spike-heparan sulfate-ACE2 with a large proportion of double-bound and triple-bound ACE2. Our findings suggest that SARS-CoV-2 variants evolve to be more dependent on heparan sulfate in viral attachment and infection. This discovery enables us to engineer a second-generation lateral-flow test strip that harnesses both heparin and ACE2 to reliably detect all variants of concern, including Omicron.

INTRODUCTION

Several SARS-CoV-2 variants of concern (VOCs) have emerged over the course of the COVID-19 pandemic, including Alpha, Beta, Gamma, Delta, and Omicron, the latter with its own sub-lineages BA.1, BA.2, BA.3, BA.4, and BA.5.[1–3] Each of these VOCs are characterized by key mutations throughout the genome.[1–3] The SARS-CoV-2 viral envelope is studded with approximately 30 homotrimer glycoproteins, called spike proteins, which play the primary role in initiating host-cell entry via their receptor binding domains (RBDs). Genomic mutations to the spike protein sequence have been implicated in increasing infectivity and/or immune escape.[4–8] The Alpha, Beta, Delta, and Omicron BA.1 genomes, for example, contain 8, 8, 9, and 34 mutations in their spike mRNA sequences relative to the original "wild-type" (WT) 2019 strain[9–13] (see Table S1 for complete list of mutations considered in this work).

The high number of sequence mutations characteristic of the Omicron variant presented a concern for potential impact on initial PCR detection.[14,15] Rapid antigen detection was also impaired for Omicron variants even though these commercially available kits detect nucleocapsid proteins that incur a lower rate of mutation.[14,15] Furthermore, the newer subvariants of Omicron, particularly BA.5, could completely escape from detection in current rapid kits.[16] To overcome the reduced sensitivity of the rapid kits, the Food and Drug Administration recommended (August 11, 2022) repeated testing within 48 h.[17] Rapid antigen detection of variant spike proteins is even more challenging considering the spike genome's high mutation rate, often

[1]Department of Applied Physical Sciences, University of North Carolina — Chapel Hill, 1112 Murray Hall, CB#3050, Chapel Hill, NC 27599-2100, USA

[2]Department of Chemistry and Biochemistry, University of California, San Diego, 4238 Urey Hall, MC-0340, La Jolla, CA 92093-0340, USA

[3]These authors contributed equally

[4]Lead contact

*Correspondence: ramaro@ucsd.edu (R.E.A.), ronifree@email.unc.edu (R.F.)

https://doi.org/10.1016/j.xcrp.2023.101346

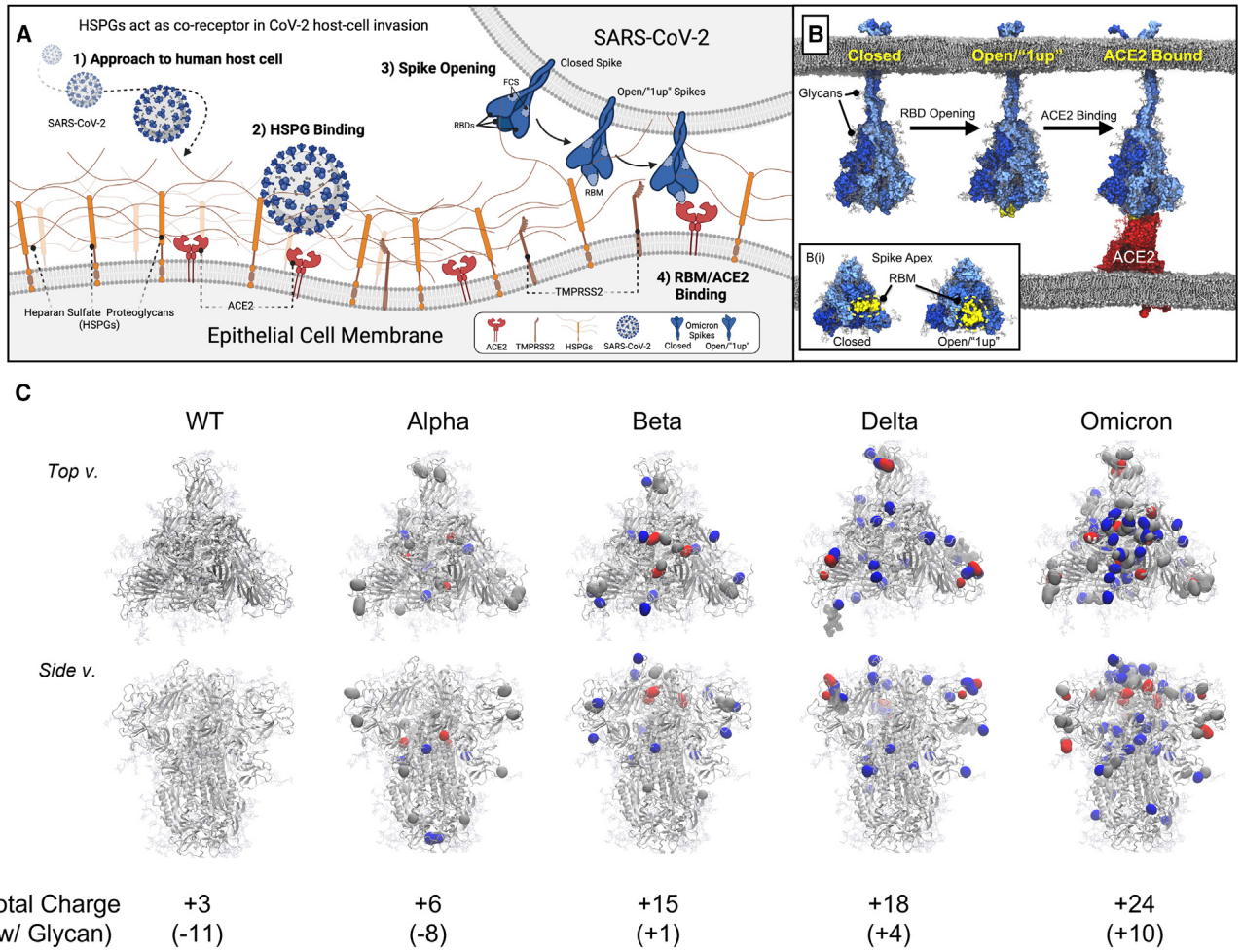

Scheme 1. Illustration of SARS-CoV-2 host-cell invasion and mutations on the VOC spike proteins

(A) Scheme depicting initiation of host-cell invasion process through HS/ACE2/spike ternary complex formation via (1) SARS-CoV-2 approach to the human host-cell, (2) SARS-CoV-2 viral binding to heparan sulfate proteoglycans (HSPGs) on the host-cell membrane, (3) conformational change of SARS-CoV-2 spike proteins from a closed to open state, open spike demonstrating 1 receptor binding domain (RBD) in the "up" state with an exposed RBM, i.e., a "1up" spike, and finally (4) spike/ACE2 binding mediated by the receptor binding motif (RBM).

(B) Molecular models depicting steps 3 and 4 from (A).[27] (B(i)) Inset illustrating an apical view of the spike head highlighting the RBM's relative exposure in closed and open spike conformations.

(C) Mutations on the VOC spike protein, introduction of positive charges due to mutation on spike protein marked as blue, negative charges as red, and neutral as gray. Total charge of each spike protein head domain (residues 13 to 1,140, residues titrated to pH 7.4 with PROPKA[28]) given in parentheses next to the strain indicator.

necessitating re-screening of spike antibodies, a step that can cause significant lag time behind the emergence of new variants.[18–20]

Elucidating the factors affecting spike binding kinetics and stability at the host-cell surface will help predict further mutations or gains of function, as well as aid in developing variant-specific antiviral therapies and better antigen testing platforms. As the SARS-CoV-2 virion approaches the cell surface (Step 1 in Scheme 1A), it encounters the glycocalyx, a dense sugary matrix extending from the epithelial cell membrane.[21,22] Heparan sulfate proteoglycans (HSPGs), key components of the glycocalyx, are known to serve as attachment factors for many viruses and likely to make first contact with SARS-CoV-2.[23–25] HSPGs contain long, intrinsically disordered protein backbones decorated with longer (40–400 monomeric units) poly-sulfated and

densely negatively charged glycosaminoglycans (GAGs).[26] Heparan sulfate (HS) itself is biosynthesized natively in repeating dimeric units of N-acetyl-D-glucosamine and D-glucuronic acid; post-processing enzymes then add sulfate groups to certain positions along an HS sequence, and epimerization enzymes may convert some D-glucuronic acid monomers to L-iduronic acid. Neither sulfation nor epimerization reactions go to completion, thus there exist locally controlled regions of high/low sulfation/epimerization proportions further contributing to vast degree of glycocalyx heterogeneity. HS regions with particularly high proportions of sulfation and L-iduronic acid are referred to as "heparin-like" domains, calling on their similarity to short-chain medicinal heparin (HEP), which is almost completely sulfated and epimerized.[26]

Several studies in early 2020 first illustrated that the SARS-CoV-2 spike protein, particularly the RBD, can bind to HS and/or HEP,[29–32] and that cellular HS was required for SARS-CoV-2 host-cell invasion.[21] With these prior results, the second step in the viral invasion process comes into focus, as shown in Scheme 1A: Binding of the virion to HSPGs, likely through direct spike-HS interactions as shown by us[33] and others.[21,22,29–31,34–42] This step may increase virion residence time at the host-cell surface, thereby increasing the likelihood of encountering angiotensin converting enzyme 2 (ACE2), SARS-CoV-2's primary host-cell receptor.[38,39,43] The spike protein binds to ACE2 via a highly specialized interface within the RBD called the receptor binding motif (RBM).[44–49] Each of the spike's three RBDs (1 RBD per spike protomer, 3 RBDs per trimer spike complex, 1 RBM per RBD, 3 RBMs per trimer spike complex) may often occupy a "closed" or "down" conformational state wherein these RBMs are largely shielded from recognition.[50–53] Thus, before spike-ACE2 binding can occur, at least one of these RBDs needs to emerge from its down/"shielded" state to an "up"/"open" state, to expose its RBM (Scheme 1B(i)).[50,51] While this step (Scheme 1B) can occur anytime along the spike conformation switching, Clausen et al. report that short-chain HEP is capable of inducing spike RBDs to move into the up-state, suggesting that RBD opening could be induced after spike binding to HS and/or HEP within the glycocalyx.[21] With the RBM exposed, ACE2 can bind, further stabilizing the virion at the host-cell surface. Finally, with the spike protein immobilized by HS and/or ACE2, TMPRSS2 can cleave the spike S2′ site.[54–58] Next, the S1 domain peels off from the S2, revealing the spike's fusion peptide, which then penetrates the host-cell membrane and initiates membrane fusion.[59–61]

Recent studies have demonstrated that the Omicron SARS-CoV-2 virion relies less on membrane fusion as catalyzed by TMPRSS2 cleavage than earlier strains, and rather more on endocytosis. Indeed, syncytial formation—neighboring SARS-CoV-2 infected cells fusing together, a phenomenon indicative of TMPRSS2 activity—was reduced for Omicron-infected tissues.[62,63] Furthermore, infection of TMPRSS2 knock-out cells by SARS-CoV-2 was increased for Omicron relative to other VOCs.[63,64] This mechanistic change could be due to Omicron sequence mutations near the S2′ site causing decreased recognition by TMPRSS2.[62–64] Furthermore, recent research suggests that mutations in the Delta and Omicron RBMs result in altered binding affinities to ACE2 compared with WT.[65–70] Several past works have identified that charge-charge interactions heavily stabilize the WT spike-ACE2 interface,[71] and that increasing spike charge over the course of SARS-CoV-2 evolution potentially increases electrostatic recognition of ACE2 at long range and increases immune escape,[41] especially for Omicron, as its spike's RBM is more positively charged than other spikes.[42] While the role of evolving positive charge on spike proteins has begun to be unraveled for ACE2,[41,42,65–70] this investigation was done in isolation from its required co-factor, HS.[71] As HS is a long,

negatively charged polysaccharide, the growing positive charge on spike virions, especially for Omicron, is expected to impact the stability of interactions with the HS-rich glycocalyx. In addition, since HS was previously shown to stabilize spike-ACE2 interactions, an altered affinity to HS may in turn also affect binding to ACE2.

Here, we probe the interactions between HS, ACE2, and the spike proteins of WT, Alpha, Beta, Delta, and Omicron SARS-CoV-2 variants. We propose how the positively charged Omicron spike may unlock a critical HS/ACE2 synergy. By harnessing the power of the primary and secondary cell receptors in the glycocalyx, we show how the performance of HEP-anchored test strips can co-evolve with the SARS-CoV-2 genome for robust and rapid sensing of Omicron. Finally, given that our synthetic glycocalyx test strips represent a minimal model for the cell surface, we discuss the potential implications our results may have on understanding SARS-CoV-2 infection dynamics at large.

RESULTS AND DISCUSSION

Spike mutations increase binding affinity to ACE2 and heparin

Previous work has demonstrated mixed results with respect to relative binding affinities between ACE2 and different spike protein sequences. Some groups report the Omicron spike protein binds to ACE2 with highest affinity, while others report there is no significant difference in binding affinity between all variants.[65–70] Herein, we have used bio-layer interferometry (BLI), enzyme-linked immunosorbent assays (ELISA), and molecular dynamics (MD) simulations to estimate relative binding affinities between WT, Alpha, Beta, Delta, and Omicron BA.1 spike proteins to ACE2. BLI results indicate similar binding affinities within nanomolar range for all protein complexes, with Beta and Delta having the highest affinity, followed by Omicron BA.1, WT, and finally Alpha (Figures 1A and S1). ELISA results show a clearer trend: Delta and Omicron spikes similarly show higher affinity to ACE2 than all other spike proteins (Figure 1B). Our BLI and ELISA results were consistent with previous reports showing affinities of Delta and Omicron similarly increased compared with WT.[65,66,69,70]

We also performed MD simulations of WT, Delta, and Omicron RBDs bound to ACE2 (supplemental experimental procedures). From these simulations we see interactions at the RBD/ACE2 interface that may explain increased binding affinity of Omicron spike relative to WT. Barros et al. discuss the relative contact frequencies of three subregions within the RBM to ACE2: the L3 loop, the central beta-strands, and the right-hand loops (Figure S2).[47] They demonstrate that contacts formed between the central beta-strands and ACE2 are the strongest and maintain almost completely during their 3 replicas of 1 μs each of conformational sampling, whereas contacts formed between the L3 loop and right-hand loops to ACE2 are weaker, measured by decreased contacting frequency. From our MD simulations, we see the Omicron RBM (Figure S2), with 10 total mutations, both strengthens interactions to ACE2 within the central beta-strands (addition of salt bridge between Q493R to ACE2's E35) but also increases stabilization within the weaker right-handed loops through an aromatic interaction (N501Y pi-stacking with ACE2's Y41), and a tight hydrogen bonding network (Y505H tightly supporting a hydrogen bond between RBD's Y495 and ACE2's K353). These interactions, as also elucidated by Han et al.,[72] potentially explain the strengthening of affinity between Omicron spike and ACE2 relative to the WT.

Next, we investigated the binding affinity between the variant spike proteins and HEP. BLI and ELISA results illustrate a significant increase in affinity between HEP and

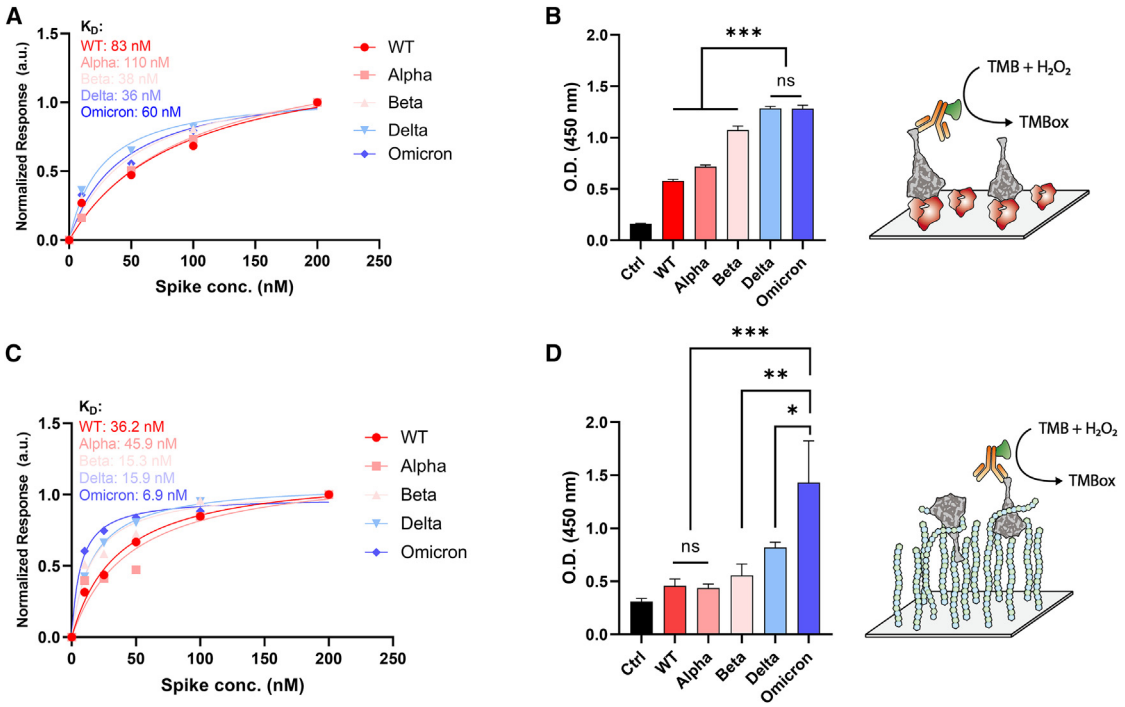

Figure 1. ACE2 and heparin binding affinity to VOC spike trimer

(A) Binding affinities of VOC spikes to dimeric ACE2 measured by BLI; K_D values were calculated with steady-state analysis.

(B) Degree of bound complex formation for VOC spikes to dimeric ACE2 as measured by ELISA. TMB (3,3′,5,5′-tetramethylbenzidine) was used as a chromogen for ELISA.

(C) Binding affinities of VOC spikes to HEP measured by BLI; K_D values calculated with steady-state analysis.

(D) Degree of bound complex formation for VOC spikes to HEP as measured by ELISA. Three independent tests were performed ($n \geq 3$), and standard deviation from mean value was represented as an error bar in the graph. p values < 0.05 (*), 0.01 (**), and 0.001 (***) were determined using a one-way ANOVA with Tukey's post hoc test.

Omicron spike over Delta and other VOC spikes (Figures 1C, 1D, and S3). To probe differences in spike affinity to HEP at the molecular scale, we conducted extensive ensemble-based docking studies with AutoDock Vina[73,74] to predict HEP binding modes to WT, Delta, and Omicron spikes in closed and open conformational states (supplemental experimental procedures). From ~28,800 binding modes, we identified a total of 19 HEP binding "hotspots," four of which were highly buried within the spike and 15 were located on the spike surface, thus accessible to long-chain HEP binding as would be seen within the glycocalyx (see Scheme S1, supplemental experimental procedures, and Figure S9 for complete descriptions of surface vs. buried sites). Relative affinities and populations of HEP binding modes at each of these sites were similar across the three spike variants (Figures S4–S11). In past work, we predicted three sites of high importance for interaction between the spike protein and HS: an RBD cleft site, an RBD patch site, and the furin cleavage site (FCS).[33] Current ensemble-based docking simulations have confirmed the presence of these sites on WT and variant spikes and indicate there are no significant differences in binding affinities or number of binding modes in these sites between spike variants (Figures S4–S11 and supplemental experimental procedures). To determine the degree to which induced-fit effects within the RBD cleft, RBD patch, FCS, and potential binding at the RBM could impact affinity, we then conducted targeted flexible protein-flexible ligand docking studies with HEP and HS tetramers at each of these sites across WT, Delta, and Omicron variants with Schrödinger's Induced Fit Docking protocol (Scheme S2 and supplemental experimental procedures).[75–79] Again, there were no significant differences between average

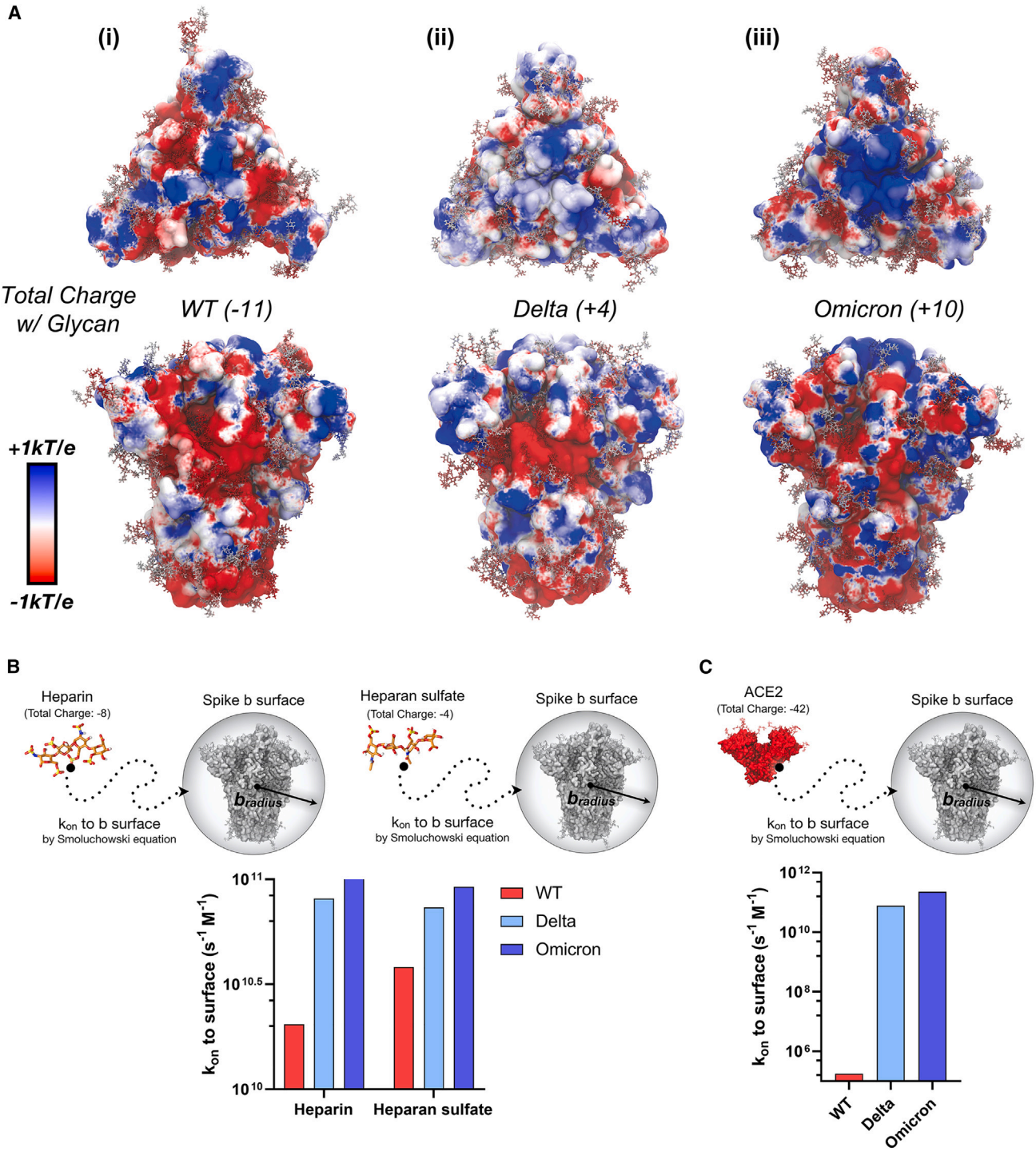

Figure 2. Dynamic electrostatic potential maps of spike trimer and Brownian dynamics simulation of HEP, HS, and ACE2 to spike trimer

(A) Dynamically averaged electrostatic potential maps collected from 50 ns of MD simulations for (i) WT, (ii) Delta, and (iii) Omicron spike proteins. The protein surfaces are colored according to average electrostatic potential at each site, ranging from −1 k_BT/e (red) to +1 k_BT/e (blue). Total charge of each spike protein head domain (residues 13 to 1,140, residues titrated to pH 7.4 with PROPKA[28]) given in parentheses next to the strain indicator; considering including a glycoprofile consistent with Casalino et al.[50] and Watanabe et al.,[81] WT, Delta, and Omicron spike proteins have total charges of −11, +4, and +10, respectively (14 sialic acids).

(B) Rate constant (k_{on}) to b-surface calculated between heparin and heparan sulfate tetramer to WT, Delta, and Omicron spike proteins (each titrated to pH 7.4) with a corresponding scheme demonstrating system diffusion to the b-surface.

Figure 2. *Continued*

(C) Rate constant (k_{on}) to b-surface calculated between and the ACE2 ectodomain (residues 18 to 734, pH 7.4) with a corresponding scheme demonstrating system diffusion to the b-surface. For (B) and (C), when calculating rate constants (k_{on}) to the b-surface, receptor molecules are modeled as spheres defined by a b-radius, and total charge. The k_{on} is calculated analytically according to the Smoluchowski equation (details in supplemental experimental procedures). Bars are colored according to a red to blue color scale normalized to VOC spike total charge with 14 sialylated glycans: WT (−11) in red, Delta (+4) in light blue, and Omicron (+10) in blue.[58,82] It should be noted that error bars are not necessary for data presented in Figures 2B and 2C, as these values represent exact analytical solutions to the Smoluchowski equation.

predicted binding energies for HEP or HS tetramers at each of these sites, across the three spike variants, even with global (MD enabled ensemble docking) and local (Schrödinger IFD) protein flexibility incorporated (Figure S12). This likely indicates that once an HS/HEP fragment finds a site on the spike surface, it is flexible enough to accommodate sequence mutations and maintain affinity at the surface. These docking results suggest that the increased binding affinity between HEP and SARS-CoV-2 Delta and Omicron spikes relative to WT, as observed with BLI and ELISA, most likely do not originate from site-specific changes.

Increased positive charge on Spike protein enhances rate of binding to ACE2 and Heparin

As previously noted by us[43,80] and others,[41,42,67] the spike protein is becoming more positively charged with each emerging VOC spike sequence (Scheme 1C). The total formal charge of the trimeric WT spike head domain (residues 13 to 1,140) at pH 7.4 is +3, Alpha is +6, Beta +15, Delta +18, and Omicron BA.1 +24. Several glycans on the spike ectodomain are also shown to be sialylated. Although a complete differentiation of glycan sialylation rate per spike sequence is far beyond the scope of this work, it is important to estimate the relative contribution of sialic acids to total spike head domain charge. Assuming a glycoprofile consistent with models from Casalino et al.[50] (14 sialic acid residues on 57 head domain glycans) and described by Watanabe et al.,[81] the total formal charge of the trimeric WT spike head domain with glycans is −11, Alpha is −8, Beta +1, Delta +4, and Omicron BA.1 +10 (Scheme 1C, Table S1). From this accounting of charge, it is evident that the spike protein head domains are increasing in total charge. In addition, to identify where positive and negative charges are most concentrated on the spike surface, we calculated dynamically averaged electrostatic potential maps of the WT, Delta, and Omicron (Figures 2A, S13, and supplemental experimental procedures). Interestingly, while the total spike charge is increasing, we also observed a clear redistribution of positive and negative charge across the spike surface between VOCs. Particularly, the Omicron spike surface exhibits a distinct redistribution of charges with a dramatic positively charged "bullseye" at its apex (Figure 2A(iii)). While the bullseye pattern is only clear in the closed state, the remapping of charge across the variant timeline is also demonstrated for 1up spike conformations (Figure S13). Increasing total charge of the spike protein, along with redistribution of charges on the spike surface have the potential to impact HS/HEP binding to spike within the glycocalyx.

To investigate the effects of spike total charge on HEP binding, we used Brownian dynamics (BD)[83,82] simulations with Browndye[83,82] to calculate rate constants (k_{on}) to a "b-surface," wherein the center of mass of a receptor molecule of interest defines the center of a sphere with a "b-radius" (Figure 2B). The receptor and ligand molecules, each containing partial atomic charges, approach one another from infinite space. In such a model, a k_{on} between two molecules attaining an intermolecular distance less than the b-radius is largely driven by charge-charge interactions and can thus be solved numerically using the Smoluchowski equation.[84] These results provide insight into long-range electrostatic interactions between molecules. We observe a dramatic increase in k_{on} to the b-surface between an HEP tetramer (charge

−8) and WT, Delta, and Omicron spike proteins, 2×10^{10} $M^{-1}s^{-1}$, 8×10^{10} $M^{-1}s^{-1}$, 1×10^{11} $M^{-1}s^{-1}$, respectively, (Figure 2B and supplemental experimental procedures). A similar trend is observed for the k_{on} to the b-surface between a model HS tetramer (charge −4) and WT, Delta, and Omicron spikes (Figure 2B). In addition, seeing as the k_{on} to the b-surface calculated for HS to WT was higher than that for HEP to WT, we predict that HS, owing to its decreased sulfation and charge, is likely to find and bind more quickly to WT spike surface than fully sulfated HEP domains. These results indicate that optimized long-range electrostatic interactions via spike mutations could dramatically impact the rate of SARS-CoV-2 viral approach to the glycocalyx (Step 1 in Scheme 1). Together with our docking results, which predicted very little difference between VOC spikes in HEP binding affinities at HEP binding hotspots, the BD results illustrate that increased affinities between HEP and Delta/Omicron spikes relative to WT, as seen by BLI and ELISA, may be due to kinetic selection allowing for increased encounters rather than site-specific differences in binding affinity. Furthermore, due to drastic difference in k_{on} to b-surface for WT spike between HEP and HS tetrameric models (Figure 2B)—a trend that is nonexistent, if not reversed, for Delta and Omicron spike proteins—we predict that WT spike proteins have the potential to demonstrate increased selectivity for the less densely sulfated/charged heparin-like domains, while Delta and Omicron spike proteins would demonstrate little to no selectivity, or moderately increased selectivity for more densely sulfated/charged heparin-like domains.

Considering that ACE2's dimeric ectodomain has a total charge at pH 7.4 of −42 (total formal charge with glycans at pH 7.4, −54)[47] rates to ACE2, driven by long-range electrostatic interactions, may also be affected by increasing spike protein charge. Therefore, we also calculated rate constants (k_{on}s) to b-surfaces between the ACE2 ectodomain and WT, Delta, and Omicron spike proteins (supplemental experimental procedures). Interestingly, we see six orders of magnitude increase in k_{on} between WT and Delta spikes to ACE2, followed by a one order of magnitude increase in k_{on} between Delta and Omicron spikes to ACE2 (Figure 2C). As with the HS/HEP results, the increasing total charge of spike proteins may strengthen long-range electrostatic interactions to negatively charged ACE2. In addition, recall that binding affinities between SARS-CoV-2 VOC spikes and ACE2 are increasing (decreasing K_D), but only moderately (Figures 1A and 1B). In sum, these BD results for HEP, HS, and ACE2 all point to kinetic fitness for interactions between the spike protein and negatively charged HEP/HS/ACE2 within the glycocalyx as a potential underlying evolutionary pressure driving SARS-CoV-2 spike sequence adaptation. Furthermore, the interactions of spike with other charged glycoprotein species and glycans within the glycocalyx such as neurophilin, CD147, GRP78, and sialic acids, could potentially be altered with the change in the charge on spike.

Remapping of positive charge distribution on Omicron surface maximizes heparin/ACE2 synergy

As can be seen from the dynamically averaged electrostatic potential maps in Figures 2A(i–iii) and S13, spike sequence mutations increase the total spike charge as well as redistribute surface patches of positive and negative charge. As a result, the site of first contact between HS/HEP and spike surface, i.e., a nucleation site for HS/HEP long-chain binding to the spike surface, could be altered on a per-VOC basis. To probe these changes, we again used BD simulations to investigate the rate of HS and HEP tetramer association, this time specifically to the RBM, RBD cleft, RBD patch, and the FCS sites (supplemental experimental procedures). We find that HEP tetramers associate differentially to spike surface sites due to mutations at each site (Figures 3A and 3B). Upon approaching a WT spike protein,

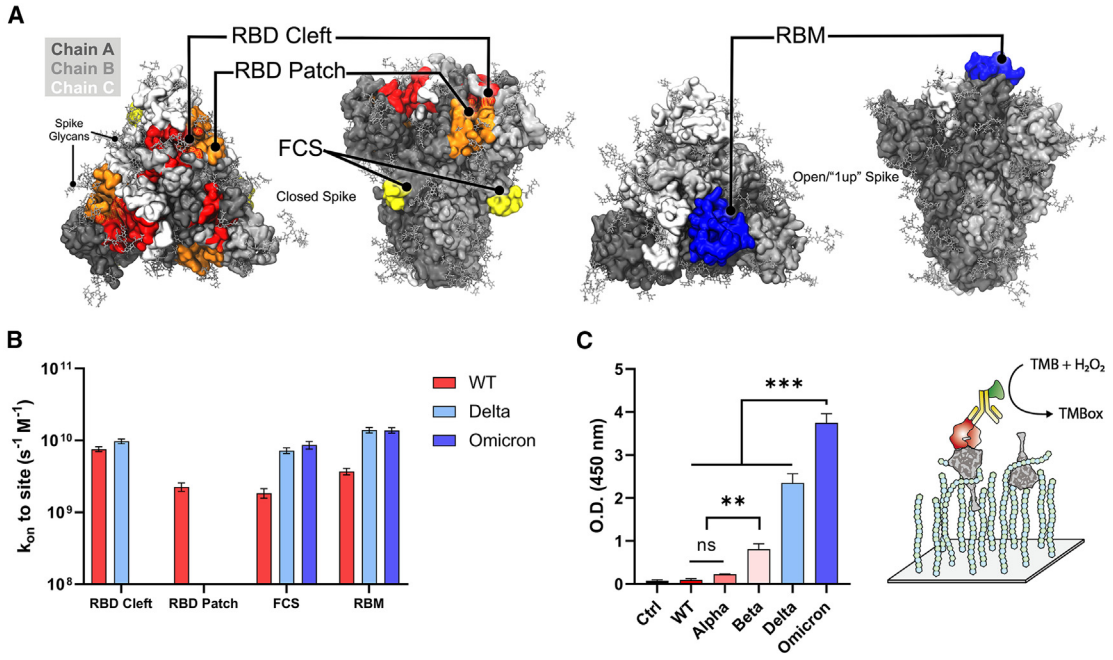

Figure 3. Site-specific Brownian dynamics simulation and comparison of ternary complex formation between VOCs spike trimer

(A and B) Spike structures illustrating receptor binding domain (RBD) cleft, RBD patch, furin cleavage site (FCS), and the receptor binding motif (RBM) as designated sites targeted with BD simulations and (B) corresponding BD results shown as second-order rate constants between HEP and identified RBD cleft, RBD patch, FCS, and RBM sites.

(C) Degree of bound ternary complex formation for VOC spikes to HEP and ACE2 as measured by ELISA. Three independent tests were performed ($n \geq 3$), and standard deviation from mean value is represented as an error bar in the graph. p values < 0.05 (*), 0.01 (**) and 0.001 (***) were determined using a one-way ANOVA with Tukey's post hoc test.

our kinetic experiments indicate that HEP tetramers are most likely to associate with the RBD cleft site first, followed by the RBM, the RBD patch, and finally the FCS. However, upon approaching a Delta spike protein, HEP tetramers are most likely to find the RBM first, followed closely by the RBD cleft, and finally the FCS, with no observed transitions into the RBD patch. Similarly, when encountering Omicron spike proteins, HEP tetramers are most likely to first find and bind the RBM, followed by the FCS, with no observed transitions to the RBD cleft or patch sites. ESP maps of the Omicron RBM reveal that it is strongly positively charged, which likely supports the kinetic advantage for binding HEP at this site (Figure S13C(i)). These results indicate that redistribution of positive charges, especially for Omicron spikes, might cause a competition between HEP and ACE2 binding on the RBM site of the spike protein. However, at the cell surface, ternary complex formation among HS, spike, and ACE2 is potentially required for stabilization of the spike-ACE2 interface.[21] Thus, we conducted ternary complex ELISA to identify whether HEP and ACE2 compete with one another for spike binding on a per-VOC basis (Figure 3C). While this ternary complex ELISA relies on both spike-HEP and spike-ACE2 binding, it could be hindered by decreased affinity at either interface. Strikingly, we observed a significant increase in the affinity of the Omicron spike-HEP-ACE2 ternary complex over all other variants, including Delta. It should be noted that when comparing Figure 3C with Figures 1B and 1D, the trend in ternary complex formation affinities compares more similarly to that seen in spike-HEP binary complex formation (Figure 1D) than spike-ACE2 complex formation (Figure 1B). Furthermore, the relatively similar affinities for Delta and Omicron spike proteins to ACE2 binding does not translate to a similar affinity in ternary complex formation for these two spike variants. These

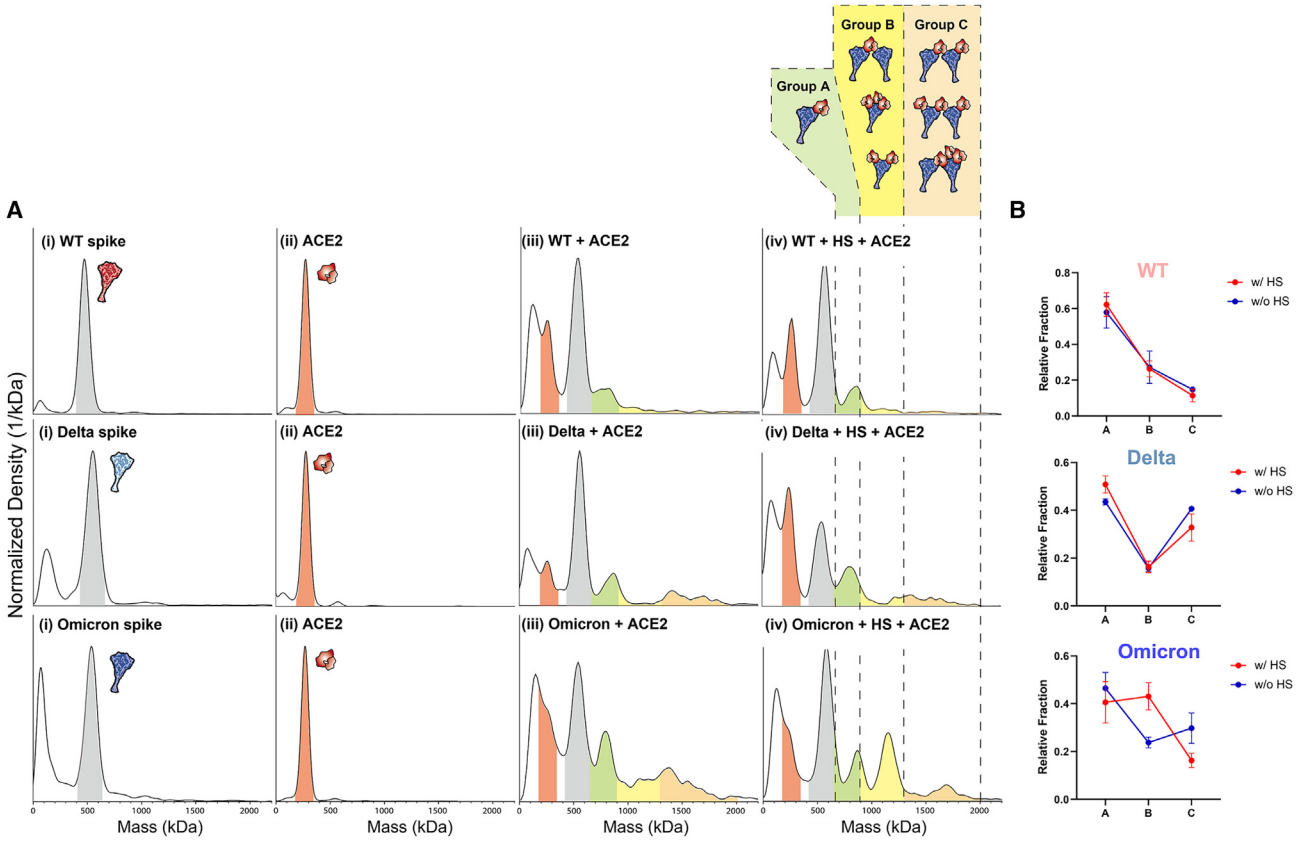

Figure 4. Synergistic formation of ternary spike/HS/ACE2 complexes visualized with mass photometry

(A) Mass photometry results comparing the WT, Delta, Omicron spikes binding to ACE2 and heparan sulfate (HS). (i) Mass distribution of WT, Delta, and Omicron spikes (mass range highlighted in gray), (ii) mass distribution of the dimeric ACE2 (mass range highlighted in red), (iii) mass distribution of spike protein + ACE2, and (iv) mass distribution of spike + HS + ACE2. To mimic the viral entry mechanism, HS was incubated with spike proteins first then followed by addition of ACE2. Possible ternary complexes are grouped in A (green), B (yellow), C (orange) based on their expected mass ranges. The molar ratio used in this study was spike:HS:ACE2 = 1:1:0.5.

(B) Fraction of ternary complex with or without HS for WT, Delta, and Omicron obtained by mass photometry. To calculate the fraction of these complexes, count numbers from each group (A, B, C) in Figure 4A were obtained. At least three independent experiments were performed, and error bars were calculated by the standard deviation of all experiments. Significance was calculated via multiple t test (unpaired) with Holm-Sidak method (α: 0.05) was performed.

results indicate that remapping of positive charges, especially for Omicron, did not hinder the binding of HEP and ACE2 on spike protein. Instead, HEP and ACE2 can co-bind to the spike protein (Figure S13D shows the how 1up SARS-CoV-2 spike can accommodate ACE2 and HEP).

As HS has been reported to induce the open conformation of spike protein and enhance ACE2 binding, we further investigated the synergistic formation of ternary spike/HS/ACE2 complexes with mass photometry (MP). We then compared the effect of HS on formation of ternary complexes for WT, Delta, and Omicron spike proteins in the presence of dimeric ACE2, by measuring the mass distributions (Figures 4 and S14–S16 for repetition of MP results, supplemental experimental procedures).

The mass of each trimeric spike protein was measured to be around 560 kDa, and the mass of dimeric ACE2 was 240 kDa. Given that spike likely first encounters the extended tendrils of HS on approach to the human host-cell, we sequentially added first HS and then ACE2 to spike protein samples to mimic conditions at the cell

surface. Co-incubation of spike with just ACE2 generated mass peaks for WT, Delta, and Omicron spike around 800 kDa, followed by signal density in higher mass ranges indicating that spike and ACE2 are interacting to form complexes at varying stoichiometric ratios (Figure 4A(iii)). Interestingly, while incubating spike and ACE2 with HS yielded very little differences in MP spectra for WT and Delta spikes compared with no-HS conditions, Omicron showed a significant increased population around 1,200 kDa under these testing conditions (Figure 4A (iv)), suggesting it plays a role in stabilizing a ternary spike-HS-ACE2. To assign possible stoichiometries to the emerging 1,200-kDa complex, we must understand the structural requirements for such assembly. Spike protein binding to ACE2 requires at least one spike RBD to be in the up conformation and a successful binding event between the two proteins is canonically considered as occurring between one ACE2 and one 1up spike. However, a spike protein with three RBDs in the up-state could accommodate binding of up to three ACE2 dimers and one ACE2 dimer could itself accommodate binding of up to two spike proteins.[47,85] In addition, while dimeric ACE2 was used in this work, without the presence of B^0AT-1—B^0AT-1 is a sodium-dependent neutral amino acid transporter commonly found co-expressed and complexed with ACE2 in the gastrointestinal tract, B^0AT-1 is often used to stabilize ACE2 during structural elucidation[45] and its corresponding stabilization of the ACE2 interfacial neck domain—ACE2 in solution could exhibit more flexibility and adopt dual RBD binding modes as described by Xiao et al.[86] While all such complexes are likely biologically relevant, the degree to which, and by what mechanism(s), spike and ACE2 form such complexes of "intermediate" stoichiometry is an open question. Thus, to parse our current mass photometry results, we have enumerated several configurations of spike-ACE2 complexes (illustration within Figure 4A) and divided such complexes into three groups based on their expected mass range: A (650–900 kDa), B (900–1,300 kDa), C (1,300–2,000 kDa). To compare the change in ternary complex distribution with or without HS, the fraction of each group (denoted as A, B, C) was calculated for each spike protein (Table S4–S6 for tables denoting fractions per group for Omicron, Delta, and WT spike proteins). As shown in Figure 4B, although the addition of HS slightly increased the population of group A type complexes for WT and Delta spikes. There was no significant change in degree of complex formation for type A along with type B and C for WT and Delta spikes. However, Omicron spikes showed significantly increased proportions of type B complexes in the presence of HS (Figure 4B). Considering that HS may stabilize spike RBDs in their up conformation, as reported by Clausen et al.,[21] binding of multiple HS fragments to the Omicron spike could serve to recruit additional nearby ACE2s for binding, thereby increasing the population of group B type complexes (spike:ACE2 = 1:2, 1:3). In addition, an increased proportion of group B could also stem from one dimeric ACE2 binding two trimeric spike proteins, an interaction that could easily be facilitated by long chains of HS either binding one or both spike proteins. ACE2 bridging multiple spike proteins is likely an important factor governing complex formation at the cell surface, and HS has the potential to "hold" or cluster multiple spikes near ACE2 in preparation for multiplex binding.

To summarize all results presented thus-far: (1) binding affinity between SARS-CoV-2 VOC spikes to ACE2 are moderately increasing over the variant timeline, (2) site-specific affinities between SARS-CoV-2 VOC spikes to HEP dimers and tetramers have not changed significantly over the variant timeline, but (3) binding affinity between spike VOCs and long-chain HEP has increased over the variant timeline, (4) increasing total spike charge over the variant timeline may be increasing rates of HEP/HS/ACE2 to spike surfaces, (5) charge redistribution on the spike surface over the variant timeline may be altering HEP/HS nucleation sites in the context of

long-chain binding interactions, and finally (6) Omicron has a particular ability to unlock a key HS/ACE2 synergy by increasing proportions of 1:2 and 1:3 spike:ACE2 complexes. At the cell surface, an individual spike glycoprotein will likely encounter both HS and ACE2. In what order, and by what mechanism(s) does the spike glycoprotein interact with and exploit the native functions of HS and ACE2 to enter the human host-cell, and how do mutations to the spike sequence affect this mechanism remain outstanding questions. As illustrated in Scheme 1, for a spike-ACE2 binding event to occur, the spike's RBM needs to be sufficiently exposed, which only occurs when at least one of the spike protein's RBDs moves from a "down"/"shielded" state to the "up"/"exposed" state. Clausen et al. report that short-chain HEP can increase proportions of ACE2s bound to the spike protein, suggesting HEP can facilitate RBD opening and ACE2 binding. Based on our results, we hypothesize that as the total formal charge of the spike protein increases so does the spike's fitness for moving through and interacting with the negatively charged glycocalyx and ACE2 as shown in BLI, ELISA, and BD results. Moreover, as the spike approaches the glycocalyx, certain sites (i.e., the RBM and FCS) on VOC spikes may find and bind to HS more quickly than to others due to redistribution of charges on the spike surface. For example, in the case of the Omicron spike protein, given the rate constant for HEP binding is fastest to exposed RBMs, HS/HEP could increase the local concentration of 1up, 2up, and 3up Omicron spike proteins directly at the cell surface. While bound to the Omicron spike protein, HS would thereby stabilize spike in an attack-ready conformation while ACE2 arrives on the cell surface below. ACE2 could eventually displace HS from the RBM, which could in turn shift to one of the many other GAG-hotspots on the spike surface, including the FCS. In this fashion, the Omicron spike protein's RBM could be capitalizing on HS/HEP's capacity for kinetic selection, thereby increasing the localized concentration of ACE2-ready binding partners at the cell surface. Taken together, we suggest a mechanism by which SARS-CoV-2 variants evolve to better bind the co-receptor glycocalyx HS, which indirectly enhances its chances to bind and the stability of its interactions with the primary receptor, ACE2.

GlycoGrip test strips mimic host-cell surface to effectively detect evolved variants

As discussed in the introduction, maintaining robust testing via rapid antigen and PCR detection platforms becomes a challenge during an actively progressing public health crisis such as the COVID-19 pandemic. Recently, we showed that the interaction between the host-cell surface glycopolymers and the spike glycoprotein can be exploited to detect SARS-CoV-2 in a rapid sandwich-style lateral-flow strip assay (LFSA).[33] Our sensor termed *GlycoGrip*, was inspired by the interactions between SARS-CoV-2 virions and the glycocalyx. *GlycoGrip* uses long-chain heparin (HEP) to capture, and Au-nanoparticle conjugated anti-spike antibodies to signal for the presence of SARS-CoV-2 spike proteins. In our first generation of *GlycoGrip*, also known as *GlycoGrip1.0*, we used an N-terminal domain (NTD)-based anti-spike antibody to signal for the presence of WT, Alpha, Beta, and Delta spike proteins. In the current work, we leveraged our findings of a favorable tertiary complex formation between the Omicron spike protein, HS, and ACE2 to explore the potential of combining HEP as the capture agent, with ACE2 as the signaling probe: after all, if the virus utilizes these receptors to infect, *GlycoGrip2.0* will leverage them to detect, (Figure 5A (i,ii)).

For both generations of *GlycoGrip*, when a sample contains spike protein, a double-banded signal will appear on the lateral-flow strip: one band at the test line indicating ternary complex formation between HEP, spike, and the signaling probe,

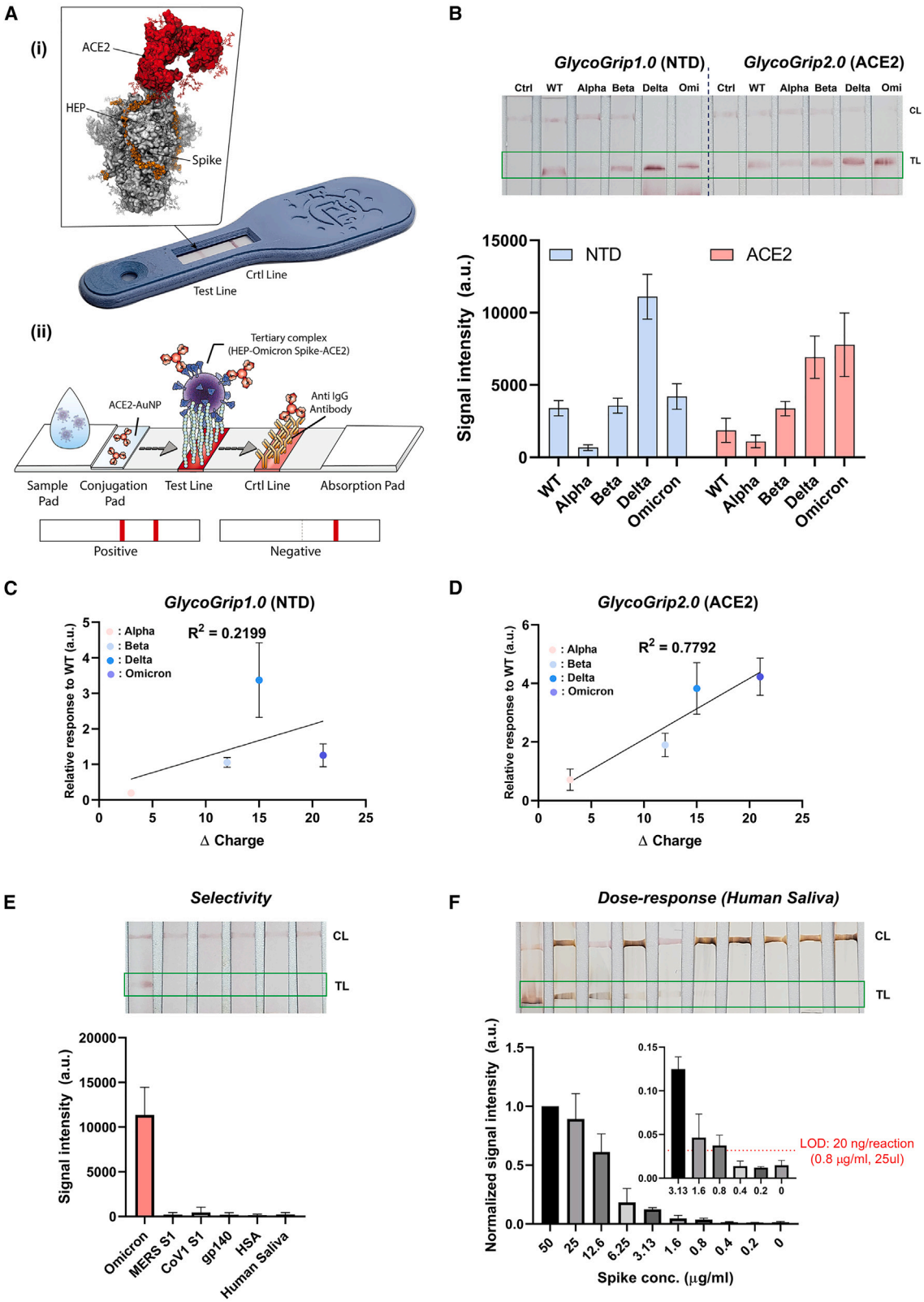
A
(i)
ACE2
HEP
Spike
Crtl Line
Test Line
(ii)
Tertiary complex
(HEP-Omicron Spike-ACE2)
ACE2-AuNP
Anti IgG
Antibody
Sample Pad
Conjugation Pad
Test Line
Crtl Line
Absorption Pad
Positive
Negative
B
GlycoGrip1.0 (NTD)
GlycoGrip2.0 (ACE2)
Ctrl WT Alpha Beta Delta Omi
CL
TL
Signal intensity (a.u.)
NTD
ACE2
WT Alpha Beta Delta Omicron
C
GlycoGrip1.0 (NTD)
R2 = 0.2199
: Alpha
: Beta
: Delta
: Omicron
Relative response to WT (a.u.)
Δ Charge
D
GlycoGrip2.0 (ACE2)
R2 = 0.7792
E
Selectivity
Omicron
MERS S1
CoV1 S1
gp140
HSA
Human Saliva
F
Dose-response (Human Saliva)
Normalized signal intensity (a.u.)
LOD: 20 ng/reaction
(0.8 μg/ml, 25ul)
Spike conc. (μg/ml)

Figure 5. Analytical performance of *GlycoGrip2.0*

(A (i)) Image of a *GlycoGrip* prototype with callout image depicting a spike protein bound to both HEP (the *GlycoGrip* capture agent) and ACE2 (the signaling probe). (A (ii)) Schematic illustrating *GlycoGrip*'s capture and signaling of SARS-CoV-2 virions.

(B and C) Comparison of the *GlycoGrip1.0 and GlycoGrip2.0* to VOCs with two different signaling probes (NTD Ab and ACE2; NTD Ab was previously used in *GlycoGrip1.0*), and (C) correlation between relative *GlycoGrip1.0* signal intensity vs. change in spike charge; charge change calculated as VOC spike charge – WT spike charge, relative signal intensities plotted as ratio with respect to WT (same data as shown in B [NTD]).

(D) Correlation between relative *GlycoGrip2.0* signal intensity vs. change in spike charge; charge change calculated as VOC spike charge—WT spike charge, relative signal intensities plotted as ratio with respect to WT (same data as shown in B [ACE2]).

(E) Selectivity of the *GlycoGrip2.0* to relevant proteins including MERS, CoV1 spike, HIV envelope protein (gp140), human serum albumin (HSA), and human saliva.

(F) Dose-dependency results of Omicron detection using *GlycoGrip2.0* with signal enhancement in human saliva condition. The limit of the detection was calculated by the blank + 3x (standard deviation of blank). At least three independent tests were performed ($n \geq 3$) for *GlycoGrip*, and standard deviation from mean value was represented as an error bar in the graph.

and one band at the control line indicating binary complex formation between the signaling probe and an anti-signaling probe antibody. We compared *GlycoGrip1.0* and *GlycoGrip2.0* against all VOC spike proteins (Figure 5B). We observed that, while *GlycoGrip1.0* still signaled well for Omicron spike, signal intensity dropped significantly relative to Delta. However, the trend observed for WT, Alpha, Beta, and Delta spikes on *GlycoGrip1.0* was similar to that reported previously.[33] Notably, *GlycoGrip2.0* elicited the strongest signal for Omicron spikes compared with *GlycoGrip1.0*. Moreover, we observed a clear trend: signal intensity on our *GlycoGrip2.0* increases along with the variant timeline (Figure 5B) in a manner strikingly similar to the increase in total spike charge. Plotting this change in spike charge (i.e., total charge changes relative to WT spike) against relative signal intensity on our reconfigured *GlycoGrip2.0*, we see these two quantities correlate with one another: $R^2 = 0.7792$ (Figure 5E) while there was no clear trend for *GlycoGrip1.0* (Figure 5C): $R^2 = 0.2199$. This correlation is striking given that, with HEP as the capture agent and ACE2 as the signaling probe, *GlycoGrip*2.0 can be seen as a simplified model for the cell-surface environment. These results indicate that, in contrast to antibody-based detection, our cell-surface mimetic sensor easily and effectively adapts to viral mutations, suggesting a novel paradigm shift in designing LFSA platforms to sensing viral antigens with high mutation rates.

Finally, we investigated the selectivity and sensitivity of our *GlycoGrip2.0* specifically for detection of Omicron spike proteins. To determine the selectivity, we interrogated our sensor with related coronavirus (MERS, CoV1) and HIV (gp140) envelope proteins along with relevant complex proteins such as human serum albumin (HSA). To illustrate *GlycoGrip*'s feasibility when used against complex biologically relevant media, we also tested our sensor against a non-infected human saliva sample to check the false-positive signal from the complex biological samples. As shown in Figure 5E, *GlycoGrip2.0* selectively captures and signals for Omicron spike proteins while not binding to related viral proteins, HSA, or other saliva matrix elements. Finally, Omicron was detectable as low as 40 ng/reaction (1.6 μg/mL, 25 μL, Figure S17) with ACE2, and 78 ng/reaction with NTD Abs. We then adopted a silver staining method to further enhance detection 4-fold for Omicron spikes: down to 10 ng/reaction (0.4 μg/mL, Figure S18). Last, we validated our sensor performance in human saliva samples. Human saliva contains various glycoproteins, including neutrophil elastase and histone H2A, which could interfere with the binding of either ACE2 or HEP to the spike protein.[87] The limit of detection in saliva was estimated to be 20 ng/reaction (Figure 5F), which was comparable to detection in buffer conditions, demonstrating the power of our sensor to detect the virus in complex fluids (see Table S7 for comparison of *GlycoGrip2.0* analytical performance with reported LFSA sensors). These results indicate *GlycoGrip* is selective for SARS-CoV-2 spike proteins, signals strongly in the presence of Omicron spikes, and is rapidly

adaptable and deployable within the context of the ever-evolving COVID-19 public health crisis. Furthermore, as SARS-CoV-2 continues to adapt to niche evolutionary pressures within glycocalyx, *GlycoGrip's* detection capacities will likely maintain and even strengthen without the need to change any of the sensor components.

As the COVID-19 pandemic now progresses into its third year, public health experts continue to scan the epidemic-horizon for new variants. Delineating the environmental and immunological pressures driving SARS-CoV-2 genomic adaptation can help predict the likely range of future mutations, and the potential impacts of those mutations on infection, re-infection, hospitalization, and mortality rates. In this work, we revealed that increased total charge on the spike proteins of SARS-CoV-2 variants, due to the progressive addition of positively charged mutations, strengthens long-range electrostatic interactions with the negatively charged host-cell surface. Furthermore, we showed that the redistribution of positive and negative charges on evolving spike protein variants, particularly for Omicron, which adopts a striking "bullseye"-like patch of positive charge near the RBM, selectively enhances the rate and strength of HS binding to exposed RBMs. We thus hypothesize that Omicron SARS-CoV-2 kinetically increases the local concentration of ACE2-binding-ready spikes at the cell surface and unlocks a key synergy between HS and ACE2. We believe this remapping of positive charge on the SARS-CoV-2 spike protein is an evolutionary driver for the optimization of electrostatic interactions of spike proteins with both HS and ACE2, thereby increasing the rate of viral entry. With these conclusions in hand, one could predict that emerging variants will exhibit additional charge redistribution to further fine-tune these interactions and in turn increase SARS-CoV-2 infectivity.

Finally, we leveraged our findings of a favorable tertiary complex formation among the Omicron spike protein, HS, and ACE2 to develop the *GlycoGrip2.0* sensor. We demonstrated *GlycoGrip*'s ability to "co-evolve" alongside the SARS-CoV-2 genome and we improved its detection of all VOCs (Video S1). By harnessing the primary (ACE2) and secondary (HS) cellular receptors in one sensor, *GlycoGrip2.0* essentially serves as a minimal model of the glycocalyx environment, which may be a useful platform for viral surveillance. This highlights the advantage of glycocalyx-inspired sensing in a rapidly adapting public health crisis, as it is quickly reconfigurable and employable against evolving variants. As the COVID-19 pandemic is still ongoing, due to continuous evolution of the virus, glycocalyx-inspired LFSAs are likely to be a great benefit for global health monitoring power, not only for SARS-CoV-2 but for other rapidly mutating viral antigens.

EXPERIMENTAL PROCEDURES

Resource availability

Lead contact

Further information and requests for resources and reagents should be directed to and will be fulfilled by the lead contact, Ronit Freeman (ronifree@e-mail.unc.edu).

Materials availability

This study did not generate new unique materials.

Data and code availability

The authors declare that all data supporting the findings of this study are available within this article and its supplemental information files. Any additional information reported in this paper is available from the lead contact on request. All structures

relating to simulations described herein will also be made freely available to download on the AmaroLab Web site. The following files are available at https://amarolab.ucsd.edu/covid19.php: structures (psf/pdb formats) of all docking results described herein; APBS input files for all computational calculations done herein including docking and electrostatic potential and binding energy calculations; BD input files for all Brownian dynamics simulations conducted herein. Any questions or additional information needed to access these files will be handled by the lead contact on request.

Experimental methods

All methods including MD and BD simulations, docking studies, ESP calculations, BLI, and ELISA details can be found in the Supplemental Experimental Information.

SUPPLEMENTAL INFORMATION

Supplemental information can be found online at https://doi.org/10.1016/j.xcrp.2023.101346.

ACKNOWLEDGMENTS

The authors acknowledge the Texas Advanced Computing Center (TACC) at The University of Texas at Austin for providing HPC resources that have contributed to the research results reported within this paper (http://www.tacc.utexas.edu). R.E.A. and R.F. acknowledge a Research Corporation for Science Advancement (COVID Initiative grant no. 27350) award. R.F. also acknowledges support from the North Carolina Policy Collaboratory at the University of North Carolina at Chapel Hill with funding from the North Carolina Coronavirus Relief Fund established and appropriated by the North Carolina General Assembly, NSF RAPID (DMS-2028758), and the UNC Institute for Convergent Science Director's Machete Award. R.E.A. acknowledges support from NIH GM132826, NSF RAPID MCB-2032054, a UC San Diego Moores Cancer Center 2020 SARS-COV-2 seed grant, and U19-AI171954 from NIAID. M.A.R. is supported by NIH T32 EB009380.

F.L.K., M.A.R., L.V., L.C., and R.E.A. acknowledge TACC Frontera and SDSC TSCC for their continued, unwavering support of our work over the past several years.

AUTHOR CONTRIBUTIONS

S.H.K., F.L.K., and M.A.R. contributed equally. S.H.K. and R.F. designed all experiments and conducted all assays. F.L.K., M.A.R., L.V., L.C., and R.E.A. designed all computational simulations and analyses. F.L.K., M.A.R., and L.V. conducted all computational simulations and analyses. L.C. contributed to the construction of the spike computational models. F.L.K. and M.A.R. constructed and designed all computational model images. S.H.K., F.L.K., M.A.R., R.E.A., and R.F. wrote the manuscript with input from all the authors. M.J.P. provided lung biology insights and edited the paper. R.E.A. and R.F. provided foundational guidance on experimental design and analyses.

DECLARATION OF INTERESTS

The authors declare the following patent: Glycosaminoglycan articles and methods relating thereof. Inventors: S.H.K, R.F. Application number PCT/US22/79641 was submitted on this work.

INCLUSION AND DIVERSITY

We support inclusive, diverse, and equitable conduct of research.

Received: November 8, 2022
Revised: February 7, 2023
Accepted: March 7, 2023
Published: April 7, 2023

REFERENCES

1. World Health Organization (2020). WHO Coronavirus (COVID-19) Dashboard.
2. World Health Organization (2021). Tracking SARS-CoV-2 Variants of Concern (WHO activity).
3. Center for Disease Control and Prevention (2022). SARS-CoV-2 Variant Classifications and Definitions (CDC Variants and Surveillance).
4. Bashor, L., Gagne, R.B., Bosco-Lauth, A.M., Bowen, R.A., Stenglein, M., and VandeWoude, S. (2021). SARS-CoV-2 evolution in animals suggests mechanisms for rapid variant selection. Proc. Natl. Acad. Sci. USA *118*, e2105253118. https://doi.org/10.1073/pnas.2105253118.
5. (2022). Evolutionary insight into the emergence of SARS-CoV-2 variants of concern. Nat. Med. *28*, 1357–1358. https://doi.org/10.1038/s41591-022-01892-2.
6. Otto, S.P., Day, T., Arino, J., Colijn, C., Dushoff, J., Li, M., Mechai, S., Van Domselaar, G., Wu, J., Earn, D.J.D., and Ogden, N.H. (2021). The origins and potential future of SARS-CoV-2 variants of concern in the evolving COVID-19 pandemic. Curr. Biol. *31*, R918–R929. https://doi.org/10.1016/j.cub.2021.06.049.
7. Maher, M.C., Bartha, I., Weaver, S., di Iulio, J., Ferri, E., Soriaga, L., Lempp, F.A., Hie, B.L., Bryson, B., Berger, B., et al. (2022). Predicting the mutational drivers of future SARS-CoV-2 variants of concern. Sci. Transl. Med. *14*, eabk3445. https://doi.org/10.1126/scitranslmed.abk3445.
8. Harvey, W.T., Carabelli, A.M., Jackson, B., Gupta, R.K., Thomson, E.C., Harrison, E.M., Ludden, C., Reeve, R., Rambaut, A., et al.; COVID-19 Genomics UK COG-UK Consortium (2021). SARS-CoV-2 variants, spike mutations and immune escape. Nat. Rev. Microbiol. *19*, 409–424. https://doi.org/10.1038/s41579-021-00573-0.
9. McCallum, M., Walls, A.C., Sprouse, K.R., Bowen, J.E., Rosen, L.E., Dang, H.V., De Marco, A., Franko, N., Tilles, S.W., Logue, J., et al. (2021). Molecular basis of immune evasion by the Delta and Kappa SARS-CoV-2 variants. Science *374*, 1621–1626. https://doi.org/10.1126/science.abl8506.
10. Public Health England (2020). Public Health England Investigation of Novel SARS-COV-2 Variant 202012/01 (Technical Briefing).
11. Zhou, D., Dejnirattisai, W., Supasa, P., Liu, C., Mentzer, A.J., Ginn, H.M., Zhao, Y., Duyvesteyn, H.M.E., Tuekprakhon, A., Nutalai, R., et al. (2021). Evidence of escape of SARS-CoV-2 variant B.1.351 from natural and vaccine-induced sera. Cell *184*, 2348–2361.e6. https://doi.org/10.1016/j.cell.2021.02.037.
12. Quandt, J., Muik, A., Salisch, N., Lui, B.G., Lutz, S., Krüger, K., Wallisch, A.-K., Adams-Quack, P., Bacher, M., Finlayson, A., et al. (2022). 1 breakthrough infection drives cross-variant neutralization and memory B cell formation against conserved epitopes. Sci. Immunol. *7*, eabq2427. https://doi.org/10.1126/sciimmunol.abq2427.
13. Shrestha, L.B., Foster, C., Rawlinson, W., Tedla, N., and Bull, R.A. (2022). Evolution of the SARS-CoV-2 omicron variants BA.1 to BA.5: implications for immune escape and transmission. Rev. Med. Virol. *32*, e2381. https://doi.org/10.1002/rmv.2381.
14. Mohapatra, R.K., Kandi, V., Verma, S., and Dhama, K. (2022). Challenges of the omicron (B.1.1.529) variant and its lineages: a global perspective. Chembiochem *23*, e202200059. https://doi.org/10.1002/cbic.202200059.
15. Shao, W., Zhang, W., Fang, X., Yu, D., and Wang, X. (2022). Challenges of SARS-CoV-2 omicron variant and appropriate countermeasures. J. Microbiol. Immunol. Infect. *55*, 387–394. https://doi.org/10.1016/j.jmii.2022.03.007.
16. Leuzinger, K., Roloff, T., Egli, A., and Hirsch, H.H. (2022). Impact of SARS-CoV-2 omicron on rapid antigen testing developed for early-pandemic SARS-CoV-2 variants. Microbiol. Spectr. *10*, e0200622–e0202022. https://doi.org/10.1128/spectrum.02006-22.
17. United States Food and Drug Administration (2022). At-Home COVID-19 Antigen Tests-Take Steps to Reduce Your Risk of False Negative (FDA Safety Communication).
18. VanBlargan, L.A., Errico, J.M., Halfmann, P.J., Zost, S.J., Crowe, J.E., Purcell, L.A., Kawaoka, Y., Corti, D., Fremont, D.H., and Diamond, M.S. (2022). An infectious SARS-CoV-2 B.1.1.529 Omicron virus escapes neutralization by therapeutic monoclonal antibodies. Nat. Med. *28*, 490–495. https://doi.org/10.1038/s41591-021-01678-y.
19. Tuekprakhon, A., Nutalai, R., Dijokaite-Guraliuc, A., Zhou, D., Ginn, H.M., Selvaraj, M., Liu, C., Mentzer, A.J., Supasa, P., Duyvesteyn, H.M.E., et al. (2022). Antibody escape of SARS-CoV-2 Omicron BA.4 and BA.5 from vaccine and BA.1 serum. Cell *185*, 2422–2433.e13. https://doi.org/10.1016/j.cell.2022.06.005.
20. Planas, D., Saunders, N., Maes, P., Guivel-Benhassine, F., Planchais, C., Buchrieser, J., Bolland, W.-H., Porrot, F., Staropoli, I., Lemoine, F., et al. (2022). Considerable escape of SARS-CoV-2 Omicron to antibody neutralization. Nature *602*, 671–675. https://doi.org/10.1038/s41586-021-04389-z.
21. Clausen, T.M., Sandoval, D.R., Spliid, C.B., Pihl, J., Perrett, H.R., Painter, C.D., Narayanan, A., Majowicz, S.A., Kwong, E.M., McVicar, R.N., et al. (2020). SARS-CoV-2 infection depends on cellular heparan sulfate and ACE2. Cell *183*, 1043–1057.e15. https://doi.org/10.1016/j.cell.2020.09.033.
22. Yue, J., Jin, W., Yang, H., Faulkner, J., Song, X., Qiu, H., Teng, M., Azadi, P., Zhang, F., Linhardt, R.J., and Wang, L. (2021). Heparan sulfate facilitates spike protein-mediated SARS-CoV-2 host cell invasion and contributes to increased infection of SARS-CoV-2 G614 mutant and in lung cancer. Front. Mol. Biosci. *8*, 649575. https://doi.org/10.3389/fmolb.2021.649575.
23. Cagno, V., Tseligka, E.D., Jones, S.T., and Tapparel, C. (2019). Heparan sulfate proteoglycans and viral attachment: true receptors or adaptation bias? Viruses *11*, 596. https://doi.org/10.3390/v11070596.
24. Stencel-Baerenwald, J.E., Reiss, K., Reiter, D.M., Stehle, T., and Dermody, T.S. (2014). The sweet spot: defining virus–sialic acid interactions. Nat. Rev. Microbiol. *12*, 739–749. https://doi.org/10.1038/nrmicro3346.
25. Connell, B.J., and Lortat-Jacob, H. (2013). Human immunodeficiency virus and heparan sulfate: from attachment to entry inhibition. Front. Immunol. *4*, 385.
26. Xu, D., and Esko, J.D. (2014). Demystifying heparan sulfate–protein interactions. Annu. Rev. Biochem. *83*, 129–157. https://doi.org/10.1146/annurev-biochem-060713-035314.
27. Casalino, L., Dommer, A.C., Gaieb, Z., Barros, E.P., Sztain, T., Ahn, S.-H., Trifan, A., Brace, A., Bogetti, A.T., Clyde, A., et al. (2021). AI-driven multiscale simulations illuminate mechanisms of SARS-CoV-2 spike dynamics. The International Journal of High Performance Computing Applications *10943420211006452*. https://doi.org/10.1177/10943420211006452.
28. Olsson, M.H.M., Søndergaard, C.R., Rostkowski, M., and Jensen, J.H. (2011). PROPKA3: Consistent Treatment of Internal and Surface Residues in Empirical pKa Predictions. Journal of Chemical Theory and Computation *7*, 525–537. https://doi.org/10.1021/ct100578z.
29. Mycroft-West, C.J., Su, D., Pagani, I., Rudd, T.R., Elli, S., Gandhi, N.S., Guimond, S.E., Miller, G.J., Meneghetti, M.C.Z., Nader, H.B., et al. (2020). Heparin inhibits cellular invasion by SARS-CoV-2: structural dependence of the interaction of the spike S1 receptor-binding domain with heparin. Thromb. Haemost. *120*,

1700–1715. https://doi.org/10.1055/s-0040-1721319.

30. Liu, L., Chopra, P., Li, X., Bouwman, K.M., Tompkins, S.M., Wolfert, M.A., de Vries, R.P., and Boons, G.-J. (2021). Heparan sulfate proteoglycans as attachment factor for SARS-CoV-2. ACS Cent. Sci. *7*, 1009–1018. https://doi.org/10.1021/acscentsci.1c00010.

31. Kim, S.Y., Jin, W., Sood, A., Montgomery, D.W., Grant, O.C., Fuster, M.M., Fu, L., Dordick, J.S., Woods, R.J., Zhang, F., and Linhardt, R.J. (2020). Characterization of heparin and severe acute respiratory syndrome-related coronavirus 2 (SARS-CoV-2) spike glycoprotein binding interactions. Antiviral Res. *181*, 104873. https://doi.org/10.1016/j.antiviral.2020.104873.

32. Kalra, R.S., and Kandimalla, R. (2021). Engaging the spikes: heparan sulfate facilitates SARS-CoV-2 spike protein binding to ACE2 and potentiates viral infection. Signal Transduct. Target. Ther. *6*, 39. https://doi.org/10.1038/s41392-021-00470-1.

33. Kim, S.H., Kearns, F.L., Rosenfeld, M.A., Casalino, L., Papanikolas, M.J., Simmerling, C., Amaro, R.E., and Freeman, R. (2022). GlycoGrip: cell surface-inspired universal sensor for betacoronaviruses. ACS Cent. Sci. *8*, 22–42. https://doi.org/10.1021/acscentsci.1c01080.

34. Schuurs, Z.P., Hammond, E., Elli, S., Rudd, T.R., Mycroft-West, C.J., Lima, M.A., Skidmore, M.A., Karlsson, R., Chen, Y.-H., Bagdonaite, I., et al. (2021). Evidence of a putative glycosaminoglycan binding site on the glycosylated SARS-CoV-2 spike protein N-terminal domain. Comput. Struct. Biotechnol. J. *19*, 2806–2818. https://doi.org/10.1016/j.csbj.2021.05.002.

35. Tandon, R., Sharp, J.S., Zhang, F., Pomin, V.H., Ashpole, N.M., Mitra, D., McCandless, M.G., Jin, W., Liu, H., Sharma, P., and Linhardt, R.J. (2021). Effective inhibition of SARS-CoV-2 entry by heparin and enoxaparin derivatives. J. Virol. *95*, e01987-20–e01920. https://doi.org/10.1128/JVI.01987-20.

36. Zhang, Q., Chen, C.Z., Swaroop, M., Xu, M., Wang, L., Lee, J., Wang, A.Q., Pradhan, M., Hagen, N., Chen, L., et al. (2020). Heparan sulfate assists SARS-CoV-2 in cell entry and can be targeted by approved drugs in vitro. Cell Discov. *6*, 80. https://doi.org/10.1038/s41421-020-00222-5.

37. Paiardi, G., Richter, S., Oreste, P., Urbinati, C., Rusnati, M., and Wade, R.C. (2022). The binding of heparin to spike glycoprotein inhibits SARS-CoV-2 infection by three mechanisms. J. Biol. Chem. *298*, 101507. https://doi.org/10.1016/j.jbc.2021.101507.

38. Milewska, A., Nowak, P., Owczarek, K., Szczepanski, A., Zarebski, M., Hoang, A., Berniak, K., Wojarski, J., Zeglen, S., Baster, Z., et al. (2018). Entry of human coronavirus NL63 into the cell. J. Virol. *92*, e01933-17–e01917. https://doi.org/10.1128/JVI.01933-17.

39. Lang, J., Yang, N., Deng, J., Liu, K., Yang, P., Zhang, G., and Jiang, C. (2011). Inhibition of SARS pseudovirus cell entry by lactoferrin binding to heparan sulfate proteoglycans. PLoS One *6*, e23710. https://doi.org/10.1371/journal.pone.0023710.

40. Pascarella, S., Ciccozzi, M., Bianchi, M., Benvenuto, D., Cauda, R., and Cassone, A. (2022). The electrostatic potential of the Omicron variant spike is higher than in Delta and Delta-plus variants: a hint to higher transmissibility? J. Med. Virol. *94*, 1277–1280. https://doi.org/10.1002/jmv.27528.

41. Gan, H.H., Zinno, J., Piano, F., and Gunsalus, K.C. (2022). Omicron spike protein has a positive electrostatic surface that promotes ACE2 recognition and antibody escape. Front. Virol. *2*.

42. Nie, C., Sahoo, A.K., Netz, R.R., Herrmann, A., Ballauff, M., and Haag, R. (2022). Charge matters: mutations in omicron variant favor binding to cells. Chembiochem *23*, e202100681. https://doi.org/10.1002/cbic.202100681.

43. Kearns, F.L., Sandoval, D.R., Casalino, L., Clausen, T.M., Rosenfeld, M.A., Spliid, C.B., Amaro, R.E., and Esko, J.D. (2022). Spike-heparan sulfate interactions in SARS-CoV-2 infection. Curr. Opin. Struct. Biol. *76*, 102439. https://doi.org/10.1016/j.sbi.2022.102439.

44. Lan, J., Ge, J., Yu, J., Shan, S., Zhou, H., Fan, S., Zhang, Q., Shi, X., Wang, Q., Zhang, L., and Wang, X. (2020). Structure of the SARS-CoV-2 spike receptor-binding domain bound to the ACE2 receptor. Nature *581*, 215–220. https://doi.org/10.1038/s41586-020-2180-5.

45. Yan, R., Zhang, Y., Li, Y., Xia, L., Guo, Y., and Zhou, Q. (2020). Structural basis for the recognition of SARS-CoV-2 by full-length human ACE2. Science *367*, 1444–1448. https://doi.org/10.1126/science.abb2762.

46. Zhao, P., Praissman, J.L., Grant, O.C., Cai, Y., Xiao, T., Rosenbalm, K.E., Aoki, K., Kellman, B.P., Bridger, R., Barouch, D.H., et al. (2020). Virus-receptor interactions of glycosylated SARS-CoV-2 spike and human ACE2 receptor. Cell Host Microbe *28*, 586–601.e6. https://doi.org/10.1016/j.chom.2020.08.004.

47. Barros, E.P., Casalino, L., Gaieb, Z., Dommer, A.C., Wang, Y., Fallon, L., Raguette, L., Belfon, K., Simmerling, C., and Amaro, R.E. (2021). The flexibility of ACE2 in the context of SARS-CoV-2 infection. Biophys. J. *120*, 1072–1084. https://doi.org/10.1016/j.bpj.2020.10.036.

48. Ozono, S., Zhang, Y., Ode, H., Sano, K., Tan, T.S., Imai, K., Miyoshi, K., Kishigami, S., Ueno, T., Iwatani, Y., et al. (2021). SARS-CoV-2 D614G spike mutation increases entry efficiency with enhanced ACE2-binding affinity. Nat. Commun. *12*, 848. https://doi.org/10.1038/s41467-021-21118-2.

49. Verdecchia, P., Cavallini, C., Spanevello, A., and Angeli, F. (2020). The pivotal link between ACE2 deficiency and SARS-CoV-2 infection. Eur. J. Intern. Med. *76*, 14–20. https://doi.org/10.1016/j.ejim.2020.04.037.

50. Casalino, L., Gaieb, Z., Goldsmith, J.A., Hjorth, C.K., Dommer, A.C., Harbison, A.M., Fogarty, C.A., Barros, E.P., Taylor, B.C., McLellan, J.S., et al. (2020). Beyond shielding: the roles of glycans in the SARS-CoV-2 spike protein. ACS Cent. Sci. *6*, 1722–1734. https://doi.org/10.1021/acscentsci.0c01056.

51. Sztain, T., Ahn, S.-H., Bogetti, A.T., Casalino, L., Goldsmith, J.A., Seitz, E., McCool, R.S., Kearns, F.L., Acosta-Reyes, F., Maji, S., et al. (2021). A glycan gate controls opening of the SARS-CoV-2 spike protein. Nat. Chem. *13*, 963–968. https://doi.org/10.1038/s41557-021-00758-3.

52. Walls, A.C., Park, Y.-J., Tortorici, M.A., Wall, A., McGuire, A.T., and Veesler, D. (2020). Structure, function, and antigenicity of the SARS-CoV-2 spike glycoprotein. Cell *181*, 281–292.e6. https://doi.org/10.1016/j.cell.2020.02.058.

53. Wrapp, D., Wang, N., Corbett, K.S., Goldsmith, J.A., Hsieh, C.-L., Abiona, O., Graham, B.S., and McLellan, J.S. (2020). Cryo-EM structure of the 2019-nCoV spike in the prefusion conformation. Science *367*, 1260–1263. https://doi.org/10.1126/science.abb2507.

54. Rahbar Saadat, Y., Hosseiniyan Khatibi, S.M., Zununi Vahed, S., and Ardalan, M. (2021). Host serine proteases: a potential targeted therapy for COVID-19 and influenza. Front. Mol. Biosci. *8*, 725528.

55. Sasaki, M., Uemura, K., Sato, A., Toba, S., Sanaki, T., Maenaka, K., Hall, W.W., Orba, Y., and Sawa, H. (2021). SARS-CoV-2 variants with mutations at the S1/S2 cleavage site are generated in vitro during propagation in TMPRSS2-deficient cells. PLoS Pathog. *17*, e1009233. https://doi.org/10.1371/journal.ppat.1009233.

56. Papa, G., Mallery, D.L., Albecka, A., Welch, L.G., Cattin-Ortolá, J., Luptak, J., Paul, D., McMahon, H.T., Goodfellow, I.G., Carter, A., et al. (2021). Furin cleavage of SARS-CoV-2 Spike promotes but is not essential for infection and cell-cell fusion. PLoS Pathog. *17*, e1009246. https://doi.org/10.1371/journal.ppat.1009246.

57. Essalmani, R., Jain, J., Susan-Resiga, D., Andréo, U., Evagelidis, A., Derbali, R.M., Huynh, D.N., Dallaire, F., Laporte, M., Delpal, A., et al. (2022). Distinctive roles of furin and TMPRSS2 in SARS-CoV-2 infectivity. J. Virol. *96*, 00128222–e100122. https://doi.org/10.1128/jvi.00128-22.

58. Bestle, D., Heindl, M.R., Limburg, H., Van Lam van, T., Pilgram, O., Moulton, H., Stein, D.A., Hardes, K., Eickmann, M., Dolnik, O., et al. (2020). TMPRSS2 and furin are both essential for proteolytic activation of SARS-CoV-2 in human airway cells. Life Sci. Alliance *3*, e202000786. https://doi.org/10.26508/lsa.202000786.

59. Koppisetti, R.K., Fulcher, Y.G., and Van Doren, S.R. (2021). Fusion peptide of SARS-CoV-2 spike rearranges into a wedge inserted in bilayered micelles. J. Am. Chem. Soc. *143*, 13205–13211. https://doi.org/10.1021/jacs.1c05435.

60. Jackson, C.B., Farzan, M., Chen, B., and Choe, H. (2022). Mechanisms of SARS-CoV-2 entry into cells. Nat. Rev. Mol. Cell Biol. *23*, 3–20. https://doi.org/10.1038/s41580-021-00418-x.

61. Shang, J., Wan, Y., Luo, C., Ye, G., Geng, Q., Auerbach, A., and Li, F. (2020). Cell entry mechanisms of SARS-CoV-2. Proc. Natl. Acad. Sci. USA *117*, 11727–11734. https://doi.org/10.1073/pnas.2003138117.

62. Meng, B., Abdullahi, A., Ferreira, I.A.T.M., Goonawardane, N., Saito, A., Kimura, I., Yamasoba, D., Gerber, P.P., Fatihi, S., Rathore, S., et al. (2022). Altered TMPRSS2 usage by

SARS-CoV-2 Omicron impacts infectivity and fusogenicity. Nature *603*, 706–714. https://doi.org/10.1038/s41586-022-04474-x.

63. Willett, B.J., Grove, J., MacLean, O.A., Wilkie, C., De Lorenzo, G., Furnon, W., Cantoni, D., Scott, S., Logan, N., Ashraf, S., et al. (2022). SARS-CoV-2 Omicron is an immune escape variant with an altered cell entry pathway. Nat. Microbiol. *7*, 1161–1179. https://doi.org/10.1038/s41564-022-01143-7.

64. Peacock, T.P., Brown, J.C., Zhou, J., Thakur, N., Sukhova, K., Newman, J., Kugathasan, R., Yan, A.W.C., Furnon, W., De Lorenzo, G., et al. (2022). The altered entry pathway and antigenic distance of the SARS-CoV-2 Omicron variant map to separate domains of spike protein. Preprint at bioRxiv. https://doi.org/10.1101/2021.12.31.474653.

65. Hoffmann, M., Zhang, L., and Pöhlmann, S. (2022). Omicron: master of immune evasion maintains robust ACE2 binding. Signal Transduct. Target. Ther. *7*, 118. https://doi.org/10.1038/s41392-022-00965-5.

66. Socher, E., Heger, L., Paulsen, F., Zunke, F., and Arnold, P. (2022). Molecular dynamics simulations of the delta and omicron SARS-CoV-2 spike – ACE2 complexes reveal distinct changes between both variants. Comput. Struct. Biotechnol. J. *20*, 1168–1176. https://doi.org/10.1016/j.csbj.2022.02.015.

67. Cotten, M., and Phan, M.V.T. (2022). Evolution to increased positive charge on the viral spike protein may be part of the adaptation of SARS-CoV-2 to human transmission. Preprint at bioRxiv. https://doi.org/10.1101/2022.07.30.502143.

68. Mehta, P., Ravi, V., Devi, P., Maurya, R., Parveen, S., Mishra, P., Yadav, A., Swaminathan, A., Saifi, S., Khare, K., et al. (2022). Mutational dynamics across VOCs in International travellers and Community transmission underscores importance of Spike-ACE2 interaction. Microbiol. Res. *262*, 127099. https://doi.org/10.1016/j.micres.2022.127099.

69. da Costa, C.H.S., de Freitas, C.A.B., Alves, C.N., and Lameira, J. (2022). Assessment of mutations on RBD in the spike protein of SARS-CoV-2 Alpha, delta and omicron variants. Sci. Rep. *12*, 8540. https://doi.org/10.1038/s41598-022-12479-9.

70. Kim, S., Liu, Y., Ziarnik, M., Seo, S., Cao, Y., Zhang, X.F., and Im, W. (2023). Binding of human ACE2 and RBD of Omicron enhanced by unique interaction patterns among SARS-CoV-2 variants of concern. J. Comput. Chem. *44*, 594–601. https://doi.org/10.1002/jcc.27025.

71. Wang, X., Bie, L., and Gao, J. (2022). Structural insights into the cofactor role of heparin/heparan sulfate in binding between the SARS-CoV-2 spike protein and host angiotensin-converting enzyme II. J. Chem. Inf. Model. *62*, 656–667. https://doi.org/10.1021/acs.jcim.1c01484.

72. Han, P., Li, L., Liu, S., Wang, Q., Zhang, D., Xu, Z., Han, P., Li, X., Peng, Q., Su, C., et al. (2022). Receptor binding and complex structures of human ACE2 to spike RBD from omicron and delta SARS-CoV-2. Cell *185*, 630–640.e10. https://doi.org/10.1016/j.cell.2022.01.001.

73. Trott, O., and Olson, A.J. (2010). AutoDock Vina: improving the speed and accuracy of docking with a new scoring function, efficient optimization, and multithreading. J. Comput. Chem. *31*, 455–461. https://doi.org/10.1002/jcc.21334.

74. Morris, G.M., Huey, R., Lindstrom, W., Sanner, M.F., Belew, R.K., Goodsell, D.S., and Olson, A.J. (2009). AutoDock4 and AutoDockTools4: automated docking with selective receptor flexibility. J. Comput. Chem. *30*, 2785–2791. https://doi.org/10.1002/jcc.21256.

75. Schrodinger Release 2022-3 (2022). Induced Fit Docking Protocol (Schrödinger, LLC).

76. Sherman, W., Beard, H.S., and Farid, R. (2006). Use of an induced fit receptor structure in virtual screening. Chem. Biol. Drug Des. *67*, 83–84. https://doi.org/10.1111/j.1747-0285.2005.00327.x.

77. Sherman, W., Day, T., Jacobson, M.P., Friesner, R.A., and Farid, R. (2006). Novel procedure for modeling ligand/receptor induced fit effects. J. Med. Chem. *49*, 534–553. https://doi.org/10.1021/jm050540c.

78. Farid, R., Day, T., Friesner, R.A., and Pearlstein, R.A. (2006). New insights about HERG blockade obtained from protein modeling, potential energy mapping, and docking studies. Bioorg. Med. Chem. *14*, 3160–3173. https://doi.org/10.1016/j.bmc.2005.12.032.

79. Schrödinger Release 2021-3. Glide (2021) (Schrödinger, LLC).

80. Carl Zimmer, J.C. (2021). The New York times. The Coronavirus in a Tiny Drop.

81. Watanabe, Y., Allen, J.D., Wrapp, D., McLellan, J.S., and Crispin, M. (2020). Site-specific glycan analysis of the SARS-CoV-2 spike. Science *369*, 330–333. https://doi.org/10.1126/science.abb9983.

82. Huber, G.A., and McCammon, J.A. (2010). Browndye: a software package for Brownian dynamics. Comput. Phys. Commun. *181*, 1896–1905. https://doi.org/10.1016/j.cpc.2010.07.022.

83. Huber, G.A., and McCammon, J.A. (2019). Brownian dynamics simulations of biological molecules. Trends Chem. *1*, 727–738. https://doi.org/10.1016/j.trechm.2019.07.008.

84. Chavanis, P.-H. (2019). The generalized stochastic Smoluchowski equation. Entropy *21*, 1006. https://doi.org/10.3390/e21101006.

85. Mannar, D., Saville, J.W., Zhu, X., Srivastava, S.S., Berezuk, A.M., Tuttle, K.S., Marquez, A.C., Sekirov, I., and Subramaniam, S. (2022). SARS-CoV-2 Omicron variant: antibody evasion and cryo-EM structure of spike protein–ACE2 complex. Science *375*, 760–764. https://doi.org/10.1126/science.abn7760.

86. Xiao, T., Lu, J., Zhang, J., Johnson, R.I., McKay, L.G.A., Storm, N., Lavine, C.L., Peng, H., Cai, Y., Rits-Volloch, S., et al. (2021). A trimeric human angiotensin-converting enzyme 2 as an anti-SARS-CoV-2 agent. Nat. Struct. Mol. Biol. *28*, 202–209. https://doi.org/10.1038/s41594-020-00549-3.

87. Yoshizato, K., Taira, T., Sato-Matsubara, M., Sekiguchi, S., Yabunaka, Y., Kira, Y., Ohashi, T., Daikoku, A., Ofusa, K., Kadono, C., et al. (2022). Cloaking the ACE2 receptor with salivary cationic proteins inhibits SARS-CoV-2 entry. J. Biochem. *172*, 205–216. https://doi.org/10.1093/jb/mvac054.

Cell Reports Physical Science, Volume *4*

Supplemental information

SARS-CoV-2 evolved variants optimize binding to cellular glycocalyx

Sang Hoon Kim, Fiona L. Kearns, Mia A. Rosenfeld, Lane Votapka, Lorenzo Casalino, Micah Papanikolas, Rommie E. Amaro, and Ronit Freeman

Table of Contents:

- **Table S6**: Fraction of each group measured by mass photometer for WT ternary complex with or without heparan sulfate.
- **Table S7:** Comparison of the limit of detection for spike protein detection in lateral flow assay

5. Figures:

- **Figure S1**: BLI sensogram of the ACE2 binding to variant of SARS-CoV-2 spike proteins.
- **Figure S2:** Figure describing MD simulation results of RBD+ACE2 systems.
- **Figure S3**: BLI sensogram of the heparin binding to variant of SARS-CoV-2 spike proteins.
- **Figure S4:** AutoDock Vina docking results illustrating heparin dimeric and tetrameric models bound to WT (A) closed and (B) 1-up structures.
- **Figure S5:** AutoDock Vina docking results illustrating heparin dimeric and tetrameric models bound to Delta (A) closed and (B) 1-up structures.
- **Figure S6:** AutoDock Vina docking results illustrating heparin dimeric and tetrameric models bound to Omicron (A) closed and (B) 1-up structures.
- **Figure S7:** K-means clustering results determining the optimal number of clusters from 28,800 AutoDock vina binding modes.
- **Figure S8:** All 19 heparin hotspots found via ensemble-based docking with AutoDock and kmeans clustering.
- **Figure S9:** Accessible Surface Area plotted for each site calculated with a probe radius of 7.2Å, calculated according to the Shrake-Rupley algorithm.
- **Figure S10**: Violin plots demonstrating distribution of AutoDock Vina binding scores for heparin dimer (hep2) and tetramer (hep4) models each binding hotspot across all variants.
- **Figure S11:** Violin plots demonstrating distribution of AutoDock Vina binding scores for heparin dimer (hep2) and tetramer (hep4) models each binding hotspot across 1up and closed spike structures.
- **Figure S12**: Violin plots illustrating the distribution of binding scores predicted by Schrodinger's Induced Fit Docking protocol in each of the probed sites, for each of the Variants, at pH's 7.4.
- **Figure S13:** Dynamically-averaged electrostatic potential maps collected from 50 ns of MD simulations for (A) WT, (B) Delta, (C) Omicron spike proteins in the 1up RBD conformation, and (D) Images demonstrating co-bind of ACE2 and HEP to 1up SARS-CoV-2 Spike
- **Figure S14**: Repetition results of Omicron variant mass photometer. Row (A) Omicron spike + HS + ACE2, and row (B) Omicron spike + ACE2.
- **Figure S15:** Repetition results of Delta variant mass photometer. Row (A) Delta spike + HS + ACE2, and row (B) Delta spike + ACE2.
- **Figure S16**: Repetition results of Wild type mass photometer. Row (A) WT spike + HS + ACE2, and row (B) WT spike + ACE2.
- **Figure S17**: Dose-dependency results of Omicron detection using *GlycoGrip2.0* without signal enhancement. The limit of the detection was calculated by the blank + 3x (Standard deviation of blank).

- **Figure S18**: Dose-dependency results of Omicron detection using *GlycoGrip2.0* with signal enhancement. The limit of the detection was calculated by the blank + 3x (Standard deviation of blank). At least three independent tests were performed (n ≥ 3).
- **Figure S19:** ChemDraws of all molecules modeled and docked in this work. Hep2mer, hep4mer, h6s2mer, h6s4mer.
- **Figure S20:** Comparison of the heparin and heparan sulfate for mass photometer.

1. List of Abbreviations:

- VOC: Variant of Concern
- RBD: Receptor Binding Domain
- RBM: Receptor Binding Motif
- FCS: Furin Cleavage Site
- 1up: shorthand describing when one spike RBD is in the "up"/"open" state
- ACE2: Angiotensin Converting Enzyme 2
- TMPRSS2: Transmembrane Serine Protease 2
- GAGs: GlycosAminoGlycans
- HEP: Heparin
- HS: Heparan Sulfate
- ESP: electrostatic potential
- BD: Brownian Dynamics
- MD: Molecular Dynamics
- IFD: Induced Fit Docking, particularly the flexible ligand-flexible receptor protocol provided by Schrodinger Suite of programs using Glide and Prime to model ligand and protein flexibility

2. Supplemental Experimental Procedures

2.1 Computational Methods:

2.1.1. WT, Delta, Omicron Spike System Construction, MD Simulation, and Clustering:

Fully glycosylated, all-atom models of WT, Delta, and Omicron SARS-CoV-2 spike glycoprotein head domains (residues 13 to 1140) were constructed according to the following protocols.

WT: For construction of our WT "closed"/all RBD down system, a cryo-EM structure with 2.8 Å resolution was used (PDB ID 6VXX).[1] To improve the accuracy of our model, we incorporated fully resolved NTD, RBD, and pre-fusion loops from another closed spike structure (PDB ID 7JJI).[2] For construction of our WT "open"/1 RBD up system, a cryo-EM structure with 3.46 Å resolution was used (PDB ID 6VSB).[3] To improve the accuracy of our open model, we incorporated fully resolved RBD in an up-state bound to ACE2 (PDB ID 6M17)[4] and fully resolved NTD and pre-fusion loops (PDB ID 7JJI).[2]

Delta: We used the WT open and closed structures as described above as the basis for construction of our Delta variant closed and open spike glycoprotein systems. To account for the mutation profile in the Delta

variant, we induced single point mutations using the "mutate" command in psfgen. Experimental data showed significant rearrangement/structural remodeling of the NTD on Delta, so we incorporated a cryo-EM structure of the remodeled Delta variant NTD (PDB ID 7SO9).[4]

Omicron: For construction of our Omicron variant closed system, a cryo-EM structure with 3.36 Å resolution was used (PDB ID 7TF8)[5] as the base structure. Missing loops from the furin cleavage site in the Omicron PDB were grafted in from PDB ID 6VSB.[3] For construction of our Omicron variant open system, a cryo-EM structure with 3.40 A resolution was used (PDB ID 7TEI)[5] as the base structure. Missing loops in the furin cleavage site, fusion peptide, and RBD were grafted in from PDB ID 6VSB.[3] For both open and closed omicron spike glycoprotein systems, we incorporated a cryo-EM structure of a fully resolved Omicron NTD (PDB ID 7K4N).[6]

Glycosylation/ Protonation/ Solvation/ Neutralization: All spike models were then glycosylated following the same glycoprofile as used by Casalino et al.,[7] consistent with Watanabe et al.[8] Protonation states were assigned by performing stand-alone PROPKA3[9] so that the glycan atoms were considered in the calculation, however protonation states (HSE vs HSD) for histidines were assigned by use of PROPKA through Schrödinger's Protein Preparation Wizard tool.[10] AutoIMD, a VMD tool,[11] was used to resolve any glycan/protein clashes or ring penetrations in our glycoprotein systems. Glycoprotein models were then each solvated in explicit water boxes of 215 x 215 x 215 $Å^3$ and neutralized with 0.15 M NaCl.

Molecular Dynamics Simulations: All structures (6 models in total) were then subjected to the following Molecular Dynamics (MD) simulation protocol (1 replica each) with NAMD2.14,[12,13] all atoms described according to CHARMM36m all-atom force field:[14-16] 20,000 steps of Steepest Descent minimization for TIP3 water molecules and NaCl ions. Protein and glycan atoms were held fixed with a Lagrangian constraint. Heating of the solvated system from 10K to 310K by increments of 25K with protein and glycan atoms held in light restraint according to a force constant of 1 kcal/mol/Å. With each increase in temperature, 10080 steps (1fs/step) of MD simulation were performed within the NpT ensemble. Once the temperature reached 310K, 0.5 ns of NVT equilibration was performed with restraints maintained. NpT equilibration (310K, 1.01325 bar) for 0.5 ns (2fs/step) with restraint (force constant = 1 kcal/mol/Å) applied to all protein backbone atoms. Pressure was maintained a Langevin barostat. Box cell dimensions were set to flexible during pressure equilibration. NVT free (no restraints) production (310K, 1.01325 bar) simulations for 50 ns (2fs/step). 50ns NVT production runs were performed on TACC Frontera. As system pressure was equilibrated in the prior step, box cell flexibility was turned off in this step (useFlexibleCell = no).

Clustering: In preparation for ensemble-based spike/GAG docking studies with AutoDock Vina,[17,18] we selected the final frame of each 50ns MD simulation to serve as a rigid-docking receptor. We also clustered the 50ns trajectories to generate 5 other receptor structures per spike glycoprotein model. The 50ns trajectories were clustered in Python (with MDAnalysis[19,20] and Scikit-learn[21]) according to the following protocol: To remove global rotational and translational degrees of freedom before clustering, VMD[11] was used to align trajectories according to minimum Root Mean Square Deviation (RMSD) distance of all C_a atoms from their first frame positions. Water and ion atoms were stripped from resultant aligned trajectories. Aligned trajectories were then opened as universes in MDAnalysis[19,20] wherein the RMSDs of C_α atoms and glycan carbon atoms were calculated for each frame. Python Scikit-learn's[21] Kmeans clustering package was then used to cluster all frames according to C_α atom and glycan carbon atom RMSDs, and the knee locator algorithm was used to select the optimal number of clusters per simulation.

Representative structures -- i.e., those simulation frames closest in RMSD space from the true cluster center – for the 5 most populated clusters were then selected for ensemble-based docking with AutoDock Vina.[18,19] PSF/PDB pairs were generated for each structure selected herein (i.e., for the final frame and for all clustered frames) and have been made available with our shared data sets on the AmaroLab website (https://amarolab.ucsd.edu/covid19.php).

2.1.2 Ensemble-based Docking with AutoDock Vina:

As described above, we selected 6 total structures per spike conformation (the final frame from 50ns and 5 representative structures from most populated clusters) to serve as receptors in ensemble based rigid docking studies with AutoDock Vina.[17,18] The following docking methods are detailed graphically in **Scheme S1** below. Each chosen spike receptor structure (3 variants x 2 conformational states x 6 selected frames = 36 total receptor structures) was subjected to the following protocol. To ensure receptor grids generated with AutoDockTools[18] would be similarly applied to each receptor structure, first all receptor PDB structures were aligned to one another according to the S2 domain C_α atoms (protein residues 686 to 1140). After alignment, all receptor structures were converted to `pdbqt` filetype with AutoDockTools.[18] Heparin (HEP) dimer and tetramer `.pdbqt` structures were used in previous work[18] and thus the same files were used in this work (see **Figure S19** for images denoting exact molecular structures modeled in this work). Per protein structure, the center of the AutoDock[13,14] receptor grid was defined as the geometric center of the central helix atoms (protein residues 985 to 1000); this was a choice made to ensure relative consistency of the box center for all structures, regardless of closed/1up conformation. Grid box size was set to 150 x 150 x 150 $Å^3$ for all spike structures, this was chosen to ensure RBDs in the 1up state would still be encompassed within the resultant grid. All docking input files can be found in the datasets shared on the AmaroLab website (https://amarolab.ucsd.edu/covid19.php). AutoDock Vina[17,18] settings were applied as follows: energy_range = 30, exhaustiveness = 80, num_modes = 100, a combination which gave 20 binding modes per docking study. To thoroughly sample binding sites and modes on the spike surface, we conducted 20 runs of each docking procedure. A "docking procedure" being defined as one GAG model (HEP dimer or tetramer) docked into one spike receptor structure (e.g., a "docking procedure" could be described as dimeric HEP docked to WT spike in 1up state, clustered frame #1). Thus, with 20 replicas per docking procedure and 20 resultant binding modes per procedure, we obtained 400 binding modes per docking procedure. With 72 total docking procedures (2 GAG models, 3 spike variants, 2 spike conformational states, 6 receptor structures per spike variant/conformational state), we obtained 28,800 total binding modes from ensemble-based docking in this work.

We then used Scikit-learn's KMeans[21] clustering algorithm to cluster the geometric centers of all 28,800 resultant binding modes, and kneed, an inflection point calculation algorithm, to find the optimal number of clusters. From this clustering, we identified 19 distinctive GAG hotspots **(Figure S8).** To determine which of these 19 sites were accessible to long-chain HEP or HS, as would be encountered on the cell surface, we scanned all selected receptor structures (3 spike variants x 2 spike conformational states x 6 selected frames per variant/conformational state) to identify all residues within 10 Å of each hotspot centroid (for a full list of residues per site **Table S3**). As done in previous work,[22] we then used the Shrake-Rupley algorithm[23] to calculate the Accessible Surface Area (ASA) of each of these sites from the ~2 μs of freely available MD trajectories provided by Casalino et al.[7] We used these simulations to estimate ASA of defined sites, as opposed to our own 50ns trajectories, because Casalino et al.'s are much longer, and

therefore likely to be more representative of conformational variability, especially with respect to glycan degrees of freedom. We calculated ASA for all sites at probe radii ranging from r=1.4 Å (reflective of water molecule probe), 7.2 Å (reflective of small molecule binding or an antibody hypervariable loop), and 18.6 Å (reflective of a small protein binding partner or antibody's variable fragment domain). We compared ASA results calculated at r=7.2 Å between all sites and saw that in the closed state **(Figure S9)**, sites K, M, N, and R, were highly buried and likely not accessible to ligand binding. However, from the 1up state, site M becomes moderately exposed. Upon visualizing these sites on the spike structure with VMD we determined sites K, M, N, and R were indeed buried sites, however further investigation will be necessary to determine if site M does indeed become sufficiently exposed after spikes move into the 1up conformation. We then conducted further statistical analyses of these sites with MDAnalysis[19,20] as are described in the Supporting Information Results and Discussion below.

2.1.3 Schrödinger IFD:

In past work,[22] through ensemble-based docking, we identified 3 sites on the spike surface with high affinity to GAGs which could be important for anchoring the spike to long-chain GAG binding modes within the glycocalyx: the RBD cleft, the RBD patch, and the FCS. Ensemble-based docking studies in this current work (described above) reconfirmed the presence of these sites. Additionally, Brownian Dynamics simulations show the importance of the RBM as a potentially adapting kinetic discriminator for HS within the glycocalyx. While we have already incorporated a degree of protein and glycan motion with our ensemble-based docking studies -- by selecting clustered spike structures from 50ns of MD simulation -- local binding site conformations can adapt to ligand binding. To assess the degree to which local rearrangements at key binding sites could contribute to GAG binding and to see how these rearrangements do or don't change with the introduction of spike mutations, we conducted site specific flexible ligand-flexible receptor docking simulations with Schrödinger IFD **(Scheme S2)**.[24] For docking into the RBD Cleft, RBD Patch, and FCS sites, the final frame from 50ns simulations of each variant closed spike structure was taken. Since the spike is a trimeric protein, there exist three RBD Cleft, RBD Patch, and FCS sites on the spike structure. To avoid complications and confounding variability due to glycan positioning during flexible docking simulations, we specifically then selected the specific RBD Cleft, RBD Patch, and FCS sites for docking based on which sites were not occupied by glycans in the final frame. This selection was particularly important as Schrödinger IFD does not handle or treat glycan atoms and therefore would not have been able to appropriately include glycan atoms during these studies. For docking into the RBM, we selected the final frame of 50 ns simulations of each variant 1up spike structure. No special care was needed for selecting frames without glycans in the case of the RBM as the RBM, when in the up/open state, is practically unreachable by spike glycans.

To prepare all spike structures for docking with Schrödinger IFD,[24] all protein structures were first titrated to pH 7.4 with PROPKA3.[9] Then all glycan atoms were removed from protein structures as Schrödinger does not properly treat glycans. HSD, HSE, and HSP residue names were converted to the Schrödinger compatible names HID, HIE, and HIP. Structures were then converted to `.mae` format and prepared according to OPLS4[25] force field using Schrödinger Protein Preparation Wizard[10] according to the following settings: missing hydrogen atoms were added (necessary after glycan deletion), bond orders were assigned, disulfide bonds were added (necessary as Schrödinger cannot also take topology files), hydrogen bonds were optimized with PROPKA3[9] at pH 7.4, and a restrained minimization of hydrogen atoms was

performed according to energies and forces described by the OPLS4[25] force field (again necessary after glycan deletion and addition of missing hydrogen atoms). All prepared protein structures will be shared with this work. Heparin and heparan sulfate tetrameric structures (specific chemical structures of which are shown in **Figure S19** below) were prepared for flexible docking with Schrödinger's LigPrep.[26]

Binding sites for flexible docking were then defined as the center of mass of the following residues, again with care taken to ensure no site was occupied by a glycan in the selected frame from MD simulations:

- ***WT:***
  - **RBD Cleft:** (chain B and resid 346 348 349 351 352 354 355 356 357 450 454 466 467 469 489 472 490) or (chain C and resid 113 114 115 132 165 167)
  - **RBD Patch:** (chain B and resid 337 356 357 359 360 393 394 516 520 521 523 561 562 577 579 580 582) or (chain C and resid 41 170 172 173 226 227 228)
  - **FCS:** (chain B 675 676 677 678 679 680 681 682 683 684 685)
  - **RBM:** (chain A and resid 438 to 508)
- ***Delta:***
  - **RBD Cleft:** (chain A and resid 346 348 349 351 352 354 355 356 357 450 454 466 467 469 489 472 490) or (chain B and resid 113 114 115 132 165 167)
  - **RBD Patch:** (chain B and resid 337 356 357 359 360 393 394 516 520 521 523 561 562 577 579 580 582) or (chain C and resid 41 170 172 173 226 227 228)
  - **FCS:** (chain B 675 676 677 678 679 680 681 682 683 684 685)
  - **RBM:** (chain A and resid 438 to 508)
- ***Omicron:***
  - **RBD Cleft:** (chain A and resid 346 348 349 351 352 354 355 356 357 450 454 466 467 469 489 472 490) or (chain B and resid 113 114 115 132 165 167)
  - **RBD Patch:** (chain B and resid 337 356 357 359 360 393 394 516 520 521 523 561 562 577 579 580 582) or (chain C and resid 41 170 172 173 226 227 228)
  - **FCS:** (chain B 675 676 677 678 679 680 681 682 683 684 685)
  - **RBM:** (chain A and resid 438 to 508)

From each docking procedure, Glide scores were collected and analyzed holistically as well as individual binding modes were inspected to determine interactions of interest within each binding site.

2.1.4 Brownian Dynamics Simulations:

Following the preparation and docking of glycoproteins and ligands, all structures were submitted to the PDB2PQR program[27,28] to assign atomic partial charges and radii according to the CHARMM36m forcefield.[14-16] Protonation states for all systems were assigned using PROPKA3[9] at pH of 7.4. Then the "make_apbs_input" and "run_apbs_input" programs in the Browndye2 package[29,30] were used to prepare input files and run APBS 1.5[31-36] to solve the linear Poisson-Boltzmann equation for the creation of electrostatic potential grids for each molecule. Electrostatics calculations, as well as BD simulations, were performed at a temperature of 298.15K, with a NaCl electrolyte concentration of 10mM, a solvent dielectric of 78, and a solute interior dielectric of 4, and with a grid spacing of 0.5Å.

BD simulations to study the association kinetics of bimolecular reactions require definitions of reaction criteria. Following the docking procedure, key interacting residues for each of the sites on the glycoproteins were identified. For each site on each monomer of each glycoprotein, the center of mass of these residues was computed. Separately, the center of mass for each ligand was also computed. The distance between the glycoprotein site center of mass and the ligand center of mass was used as the reaction coordinate, and if this distance ever fell below a defined threshold of 14Å, a "reaction" was assumed to have occurred.

The Browndye2 package[29,30] as used to prepare and run all BD simulations. Hydrodynamics were enabled. Upon independent investigation, we observed anomalous behavior for these systems when desolvation forces were enabled, most likely due to the high magnitude of molecular charges involved. For this reason, we chose not to enable desolvation forces for these simulations. A total of 24 separate systems were simulated on the TACC Frontera supercomputer. For each system, the BD simulations were spread onto a 56-core node and ran for 24 hours. The total number of BD simulations varied between systems, and anywhere from a few hundred to a hundred thousand separate trajectories were completed per system. Following the simulations, the obtained reaction statistics may be used to estimate k_{on}s for each system. BD simulations were performed on TACC Frontera.

To compute the association rate constants to the b-surface, we use the following equation, which is derived from the Smoluchowski equation:[37,38]

$$k(r) = -\frac{DQ_cQ_s}{\left[1 - exp\left\{\frac{Q_cQ_s}{4\pi\varepsilon_0\varepsilon_r k_B T r}\right\}\right]\varepsilon_0\varepsilon_r k_B T}$$

Where *k(r)* is the association rate constant to the spherical b-surface of radius *r*, Q_s is the charge of the substrate, Q_c is the charge of the receptor, *D* is the radial relative diffusion coefficient of the two molecules, ε_0 is the vacuum permittivity, ε_r is the dielectric constant of the solvent, k_B is the Boltzmann constant, and *T* is the system temperature.

2.1.5 Spike RBD+ACE2 MD Simulations:

To investigate the stability of the ACE2/RBD interface over the course of the variant timeline, RBD+ACE2 systems were constructed for WT, Delta, and Omicron variants. RBDs were extracted from our full spike WT, Delta, and Omicron models and then aligned to a 2.90 Å cryo-EM structure of the WT ACE2/RBD complex (PDB ID 6M17).[39] ACE2 and aligned RBD complex were extracted for each variant and full glycosylation profile of ACE2 and RBD were replicated from Barros et al.[40] PROPKA3[9] was used to ensure all protonation states for ACE2 and the RBDs were still appropriate, and they were. Special attention was paid to ensure the Zn^{2+} atoms from ACE2 were retained in RBD/ACE2 system model building. Additionally, special care was taken to make sure there were no residue clashes along the RBD/ACE2 interface as the Delta and Omicron interfaces were constructed from alignment to the WT RBD structure and not resolved experimentally. All systems were solvated in water boxes of ~130 x 140 x 180 $Å^3$ and ionized with 0.15M NaCl. For each RBD/ACE2 system, we then performed 3 replicas of the following MD simulation protocol with NAMD2.14[12,13] and CHARMM36m all atom force field:[14-16] 10,000 steps of Steepest Descent minimization for all atoms (no restraints nor constraints). Heating of the solvated system from 10K to

310K by increments of 25K with protein and glycan atoms held in light restraint according to a force constant of 1 kcal/mol/Å. With each increase in temperature, 10080 steps (1fs/step) of MD simulation were performed within the NVT ensemble. Once the temperature reached 310K, 0.5 ns of NVT equilibration was performed with restraints maintained. NpT equilibration (310K, 1.01325 bar) for 0.5 ns (1fs/step) with restraint (force constant = 1 kcal/mol/Å) applied to all protein backbone atoms. Pressure was maintained a Langevin barostat. Box cell dimensions were set to flexible during pressure equilibration. GPU accelerated NVT free (no restraints) production (310K, 1.01325 bar) simulations for 25 ns (1fs/step) conducted with NAMD3.0.[13] As system pressure was equilibrated in the prior step, box cell flexibility was turned off in this step (useFlexibleCell = no). GPU accelerated NVT production runs were performed on the Hopper GPU cluster at SDSC TSCC. To prepare for analysis, VMD[11] was used to align trajectories according to protein C_α atomic positions in the first frame, and water and ion atoms were stripped from trajectories. Trajectories were then ported into MDAnalysis[19,20] as universes where native contacts analysis was performed.

2.1.6 Dynamical Electrostatic Potential Map Calculations:

To confirm the presence of large, positively charged regions on the spike surface we used a time-averaged implementation of Adaptive Poisson Boltzmann Solver (APBS)[31-36] to calculate the electrostatic potential at equally spaced grid points along the spike surface over our aligned 50ns classical MD simulation trajectories (described in **Section 2.1.1** above). We calculated electrostatic potential maps for the WT spike in closed and open states as well as for Delta and Omicron BA.1 variants full-length spike structures in the closed and open states. All resulting ESP volume (`.dx`) files for each frame of the 50ns trajectories (1260 frames per simulation) were averaged using the APBS's `dxmath` functionality. For each structure and each frame, we calculated electrostatic potential maps using the following options, and example input scripts can be found in the downloadable tar.gz file associated with this supporting information:

```
elec name frame
    mg-auto
    dime 321 321 321
    cglen 400 400 400
    fglen 200 200 200
    cgcent mol 1
    fgcent mol 1
    lpbe
    bcfl sdh
    ion charge 1 conc 0.150 radius 1.36375
    ion charge -1 conc 0.150 radius 2.27
    pdie 4.0
    sdie 78.00
```

```
    chgm spl2
    srfm smol
    srad 1.4
    swin 0.3
    sdens 10.0
    temp 298.15
    gamma 0.105
    calcenergy total
    write pot dx frame
end
```

2.2 Experimental Methods:

2.2.1 Materials

Heparin (HEP001) was purchased from Galen laboratory supplies. Heparan sulfate from bovine kidney (H7640), Human serum albumin (A3782), and sucrose (S0389), Silver lactate (359750), Hydroquinone (H9003) were purchased from Sigma-Aldrich. Biotin-PEG3-amine (BG-17) was purchased from G-Biosciences. Tween 20 (J20605-AP) was purchased from Thermo Fisher Scientific. Sodium phosphate monobasic (389872500) and Sodium phosphate dibasic (204851000) were purchased from ACROS Organics. Bovine serum albumin (105033) was purchased from MP biomedicals. Gold nanoparticles 10nm (15703-20) were purchased from Ted Pella Inc. Human ACE2, Fc Tag (AC2-H5257) was purchased from Acro Biosystems. Rabbit anti-human IgG (31143) and Horseradish peroxidase conjugated goat anti-human IgG with Horseradish peroxidase (A18811) was purchased from Invitrogen. Horseradish peroxidase conjugated anti-His Tag antibody (652504) was purchased from Biolegend. Nitrocellulose membrane (FF120HP), sample pad (Whatman CF4 dipstick pad), and absorbent pad (Whatman standard 17) were purchased from Cytiva. SARS-CoV-2 Wild type Spike (40589-V08H4), Delta (40589-V08H10) Spike, and Omicron (40589-V08H26) Spike, and HIV gp140 envelope protein (11677-V08H) were purchased from Sino biological. SARS-CoV-2 Alpha (B.1.1.7) Spike (10796-CV-100) and Beta (B.1.351) spike (10786-CV-100) were purchased from R&D systems. Streptavidin modified BLI biosensor tips (18-5019) and anti-human IgG Fc Capture (AHC) BLI biosensor tips (18-5060) were purchased from Sartorius. N-Terminal domain binding antibody (LT-2000) was purchased from Leinco Technologies. Human saliva pooled from human donors (991-05-P) was purchased from LEE Biosolutions.

2.2.2 Biotin conjugation to heparin

For BLI, ELISA, and LFSA preparation, biotin modified heparin was prepared. Specifically, 2 mg of biotin-PEG3-amine and 2 mg of heparin was dissolved in the 10 mM sodium phosphate buffer pH 7.4. Followed by the addition of the sodium cyanoborohydride (5 mg), and the solution was incubated 24 hr at 60°C. After the incubation, same amount of sodium cyanoborohydride was added and incubated for another 24

hr. Resulting solution was purified by centrifugation with 3k filter to remove the unreacted biotins. Finally, the solution was lyophilized and stored in -20°C until further use.

2.2.3 Immobilization and binding of heparin, ACE2 to variant spike proteins

To compare the binding of heparin or ACE2 to variant spike proteins, enzyme-linked immunoassay (ELISA) was utilized. Firstly, streptavidin (200 nM; 50 µL) was added to the Nunc maxisorp flat bottom 96 well plate and incubated overnight at 4°C. The plates were washed with 200 µl of 1xPBST (0.05% tween-20) three times to remove unbound streptavidin. Then the plate was blocked with 100 µl of 2% BSA for 1 hr at room temperature and washed with 1xPBST. Biotinylated heparin (800 nM; 50 µL) was incubated for 1hr and washed thoroughly to remove unbound heparin. SARS-CoV-2 Spike proteins (WT, Alpha, Beta, Delta, and Omicron; 100 nM; 50 µL) in LFSA buffer were incubated for 1 hr, and LFSA buffer without any spike protein was also incubated for 1 hr as a control. After 1 hr incubation, wells were washed with 200 µl of 1xPBST three times. For the signal generation, anti-his tag-HRP (1 µg/ml; 50 µl) was incubated for 30 min. To remove the unbound HRP, plates were thoroughly washed 5 times with 1xPBST. Finally, 50 µl of TMB substrate (Thermo Fisher Scientific, 34028) was added to each well to develop color. The reaction was stopped by adding 50 µl of stop solution (Thermo Fisher Scientific, N600), and absorbance was measured at 450 nm. In case of ACE2 binding, same procedure was used as heparin binding except that ACE2 functionalized plates were prepared by directly absorbing ACE2 (10 µg/mL; 50 µL) to Nunc maxisorp flat bottom 96 well plates at 4 °C overnight instead of streptavidin functionalization.

2.2.4 Biolayer interferometry (BLI)

For measuring the binding affinities of heparin or ACE2 to variants of SARS-CoV-2 Spike, biolayer interferometry (BLI) was used. For heparin binding affinity measurement, streptavidin coated BLI tips were functionalized with biotin-heparin (100 µg/mL, 40 µL) for 180 s. Unbound or loosely bound biotin-heparin was washed for 500 s. Heparin functionalized tips were treated with various concentrations of spike protein (10, 25, 50, 100, 200 nM) including control without spike protein for 400 sec and dissociation was measured for 500 s. Binding affinity, Dissociation Constant (K_D), was calculated with steady-state analysis using the HT 11.1 software. ACE2 binding affinity was measured with the same procedure except that anti-human IgG Fc capture (AHC) BLI tips were utilized when ACE2 (1 µg/mL; 40 µL) was loaded. For all measurements, LFSA buffer (10 mM Sodium phosphate, 0.05% tween-20, pH 7.4) was used.

2.2.5 Checking ternary complex formation (Spike-HS-ACE2) using ELISA

To check the synergy of heparin and ACE2 binding in spike protein binding, ELISA was utilized. Firstly, streptavidin (200 nM; 50 µL) was added to the Nunc maxisorp flat bottom 96 well plate and incubated overnight at 4°C. The plates were washed with 1xPBST (0.05% tween-20) three times to remove unbound streptavidin. Then the plate was blocked with 2% BSA (100 µl) for 1hr at room temperature and washed with 1xPBST. Biotinylated heparin (800 nM; 50 µL) was incubated for 1hr and washed thoroughly to remove unbound heparin. SARS-CoV-2 Spike proteins (100 nM; 50 µL) in LFSA buffer were incubated for 1 hr including the control without spike proteins. After incubation wells were washed three times with

1xPBST to remove unbound spike proteins. ACE2 (1 ug/mL; 50 µL) in LFSA buffer was added and incubated for 1 hr. After incubation, each well was washed three times with 1xPBST. Finally, anti-IgG-HRP (1 µg/mL; 50 µL) was incubated for 30 min, and plates were thoroughly washed 5 times with 1xPBST. Finally, 50 µL of TMB substrate (Thermo Fisher Scientific, 34028) was added to each well to develop color. The reaction was stopped by adding 50 µL of stop solution (Thermo Fisher Scientific, N600), and absorbance was measured at 450 nm.

2.2.6 Checking ternary complex formation (Spike-HS-ACE2) using Mass Photometer

To measure the synergy effect of heparan sulfate and ACE2 in spike protein binding, mass photometry (Refeyn One mass photometry) was utilized. Using heparin on mass photometer drastically reduced number of spike protein counts even though the same concentration of omicron spike trimer and glycans were used (**Figure S20**). This is likely due to the fact that the high number of negative charges on heparin might hinder the contacting of spike protein to the surface of the glass, resulting in a low number of count event. Therefore, heparan sulfate instead of heparin was utilized to check the ternary complex formation on mass photometer. Microscope coverslips (CG15KH1**,** 24 x 50 mm, Thickness 170 ± 5 µm**,** Thorlabs) were cleaned by sonication in 2-Propanol (A516-4, Fisher Scientific) followed by DW (10 min for each step). Silicone gasket (3 mm diameter x 1mm depth, Grace Bio-labs) was applied to the cleaned coverslip to form a chamber. After preparing the gasket, 10 µl of LFSA buffer (10 mM sodium phosphate, pH 7.4) without tween-20 was first injected to the chamber to find the focus using the autofocus function called droplet-dilution using Acquire MP Sofware provided by the instrument. Samples (Spike, Spike + ACE2, Spike + HS + ACE2) were prepared by incubating Spike (40 µg/ml; 5 µl), ACE2 (16 µg/ml; 2.5 µl), and HS (2 µg/ml; 2.5 µl) for 30 min at room temperature prior to mass photometer. For each acquisition, 10 µl of mixture of protein solution was introduced to the chamber (total volume: 20 µl) and movies of 60 s duration were recorded. Each sample was measured in new chambers (each chamber was used once). All mass photometer data were analyzed with DiscoverMP (2022 ver. R1). Firstly, using a mass calibration curve, ratiometric data was converted to the mass. Then, to check the fraction of the ternary complexes, count numbers for binding event were obtained for each mass range (denoted as group A, B, and C). Obtained count numbers were used to calculate the relative fraction of each and compare the fraction of the ternary complex with or without HS.

2.2.7 Preparation of signaling probes

To prepare the signaling probes, ACE2 and NTD Ab were conjugated to the gold nanoparticles (AuNP). Firstly, 10 nm AuNP (1 ml) was equilibrated with borate buffer (0.1 M pH 8.0; 100 µl), then ACE2 (0.6 mg/ml; 8.3 µl) or NTD Ab (1 mg/ml; 5 µl) was added to prepare the signaling probes for *GlycoGrip*2.0 and *GlycoGrip*1.0, respectively. After incubating the resulting solution for 1 hr at room temperature with continuous rotation, 100 µl of 1% BSA was added and incubated for an additional 30 min. To remove the unbound proteins, ACE2 or NTD Ab conjugated AuNPs were centrifugated at 22000g, 4°C for 45 min and the supernatant was removed. AuNP pellets were resuspended in the 1% BSA (1 ml) solution. This procedure was repeated 3 times. Finally, ACE2 or NTD Ab conjugated AuNPs were resuspended in the LFSA buffer and stored in 4°C until further use.

2.2.8 Preparation of *GlycoGrip* LFSA

For the immobilization of the heparin to the nitrocellulose membrane, heparin was conjugated to the streptavidin as previously reported. Briefly, biotin-heparin (2 mg/ml, 50 µl) was incubated with streptavidin (1 mg/ml, 100 µl) for 1 hr. The mixture solutions were purified by centrifugation with a 30k amicon filter to remove excess biotin-heparin. The concentration of heparin was measured using Azure A assay. Heparin conjugated with streptavidin (300 µM) and rabbit antihuman IgG (1 mg/mL) were dispensed on the nitrocellulose membrane (FF120HP). Dispensed nitrocellulose membrane was dried at 65 °C for 3 min. After drying, the nitrocellulose membrane was blocked with a blocking buffer (1% BSA, 0.05% Tween 20 in 10 mM PB, pH 7.4). Finally, the sample pad (Whatman CF4 dipstick pad) and the absorbent pad (Whatman standard 17) were assembled onto the nitrocellulose membrane. Assembled strips were stored at room temperature with desiccant before use.

2.2.9 Comparison of the variant detection in *GlycoGrip1.0* and *GlycoGrip2.0*

For the comparison of the SARS-CoV-2 variant detection in *GlycoGrip1.0* and *GlycoGrip2.0*, 25 µL of each of the Spike proteins (25 µg/ml) in LFSA buffer were incubated with 25 µl of signaling probes (i.e., 20 nM of NTD Ab-AuNP for *GlycoGrip1.0*, and 20 nM of ACE2-AuNP for *GlycoGrip2.0*) for 30 min at room temperature. Then, the dipstick method was used to compare the detection. Briefly, the resulting solutions were dispensed in the flat bottom 96 well plate and lateral flow strips were dipped for 10 min. After 10 min, the image was taken by smartphone camera and signals were quantitatively analyzed by ImageJ software.

2.2.10 Evaluation of Selectivity and sensitivity of *GlycoGrip2.0*

To evaluate the selectivity of the *GlycoGrip2.0*, 25 µL of each samples including SARS-CoV-2 Omicron spike (25 µg/mL), CoV1 S1 (25 µg/mL), MERS S1 (25 µg/mL), HIV gp140 (group M, CRF07_BC) envelope protein (25 µg/mL), Human serum albumin (50 mg/mL), and Human saliva (25x diluted from the stock solution) was incubated with 25 µL of signaling probe (ACE2-AuNP; 20 nM) for 30 min. Then, signals were generated with the dipstick method and analyzed with ImageJ.

For the sensitivity testing, different concentrations of SARS-CoV-2 Omicron spike (0, 0.4, 0.8, 1.6, 3.13, 6.25, 12.5, 25, 50 µg/ml; 25 µl) were incubated with ACE2-AuNP (20 nM; 25 µl) for 30 min. After 30 min, the same dipstick method was utilized. Signal intensity of the test line was analyzed with ImageJ software and the limit of the detection (LOD) was estimated by blank + 3 standard deviations. At least 3 independent tests were performed to calculate the LOD.

2.2.11 Evaluation of sensitivity of *GlycoGrip2.0* in human saliva

For human saliva testing, various concentrations of SARS-CoV-2 Omicron spike (0. 0.8, 1.6, 6.25, 25, 50, 100 ug/ml; 12.5 ul) were introduced into human saliva (25µL; 25x diluted from the stock solution). Prepared spike in human saliva solution were incubated with ACE2-AuNP (20 nM; 25 µL) for 30 min. After

30 min, dipstick method was utilized, and signal was enhanced with silver enhancement methods as described in 2.2.12.

2.2.12 Signal enhancement analysis

To enhance the sensitivity of the *GlycoGrip2.0*, silver enhancement methods[41] was adopted. Specifically, different concentrations of SARS-CoV-2 Omicron spike (0, 0.1, 0.2, 0.4, 0.8, 1.6, 3.13, 6.25, 12.5, 25, 50 ug/mL; 25 µL) were incubated with ACE2-AuNP (20 nM; 25 µL) for 30 min. After 30 min, each solution was dispensed to 96 well plates and LFSA strips were dipped for 10 min. After 10 min, Strips were sequentially washed with LFSA buffer (100 µL) and DW (100 µL) for 3 min. Finally, Strips were dipped into the mixture of 0.3% silver lactate and 3% hydroquinone (100 µL each) for 3 min and the enhancement reaction was stopped by washing with DW. Signal intensity of the test line was analyzed with ImageJ software and the limit of the detection (LOD) was estimated by blank + 3 standard deviations. At least 3 independent tests were performed to calculate the LOD.

2.3 Supplemental notes:

2.3.1 Summary of AutoDock Vina results:

28,800 GAG binding modes were collected from ensemble-based docking studies as laid out in Scheme S1 below. All binding modes for WT, Delta, and Omicron spike structures in closed and 1up conformations can be seen in **Figures S4, S5,** and **S6** respectively. The centers of mass of each of these resultant binding modes were collected passed through kmeans clustering to identify GAG binding "hotspots" on the spike surface. Figure S7 shows the sum of squared Euclidean distances (SSE) for the generated 1-100 clusters; kneed elbow locator algorithm was used to determine 19 to be the optimal number of clusters of all 28,800 binding modes. These 19 clusters were then given names A-S and their locations on the spike structure were identified, **Figure S8**. To determine which of these binding sites were "surface exposed", I.e. sites accessible to long chain GAGs within the glycocalyx, we calculated the Accessible Surface Area (ASA) for each of these sites using the Shrake-Rupley algorithm[19] through VMD tools,[11] **Figure S9**, with a probe radius of r=7.2 Å from WT trajectories shared for closed and 1up state spike proteins shared by Casalino et al.[8] Each site was defined as any residue (from all structures considered, i.e., all conformations of WT, Delta, and Omicron structures) within 10 Å of the centroid of said site as defined by kmeans clustering. A probe radius of 7.2 Å was chosen to be consistent with an approaching GAG fragment. All residue numbers per site can be found in **Table S3**. From ASA results we see that in the closed spike conformation, sites K, M, N, and R are largely inaccessible to GAG fragments within the glycocalyx. However, in the 1up spike conformation site M becomes marginally exposed due to the lifting up of the neighboring RBD.

To identify any sites of particular importance on a per spike variant basis we then analyzed the distributions of predicted binding energies within each site as given by AutoDock Vina,[17,18] **Figure S10**. As can be seen from these results, both heparin dimers and heparin tetramers bind with relatively similar predicted energies to all sites on a per variant basis, save for a few instances. We also compared the distribution of predicted binding energies at each site as a function of spike conformation, i.e., closed versus 1up states, **Figure S11**. Again, very little difference could be seen between closed and 1up spike

structures to suggest heparin dimers or tetramers favor binding to either state. Given the similarity in predicted energies, and the broad distribution of predicted energies at each site in all resultant binding modes, we cannot predict, at this time, any significant differences in binding affinity at each site resulting from changes in spike sequence. As such we predict binding affinity differences as observed with BLI between heparin and variant spike structures are likely due to effects only captured by use of long-chain heparins or due to kinetic effects such as rate of encounter complex formation.

2.3.2 Summary of Schrödinger IFD Results:

While we have already incorporated a degree of protein flexibility in our docking studies by conducting extensive ensemble-based sampling (i.e., 3 spike proteins (WT, Delta, Omicron) x 2 spike states (closed, 1up) x 6 conformations each = 36 total spike receptor structures) we were interested in identifying any potential induced fit effects and how such effects may adapt/change over the variant timeline. As such we conducted flexible ligand-flexible receptor docking studies with Schrödinger IFD on targeted sites within the spike protein using heparin and heparan sulfate tetrameric models. From these results, **Figure S12,** we again see predicted binding energies (Glide Scores) are broad at each site, and there is virtually no difference in these distributions across the variant timeline despite mutations within each site. We predict that this is due to the innate flexibility of GAG molecules like heparin and heparan sulfate. These ligands can adapt to mutations within these binding sites and thus still bind at each site. Thus, we predict differences in binding affinity between heparin/heparan sulfate and spike proteins as seen from BLI and ELISA results are likely due to effects that can only be seen at the long-chain binding mode scale or due to kinetic effects not captured in docking studies.

Schemes:

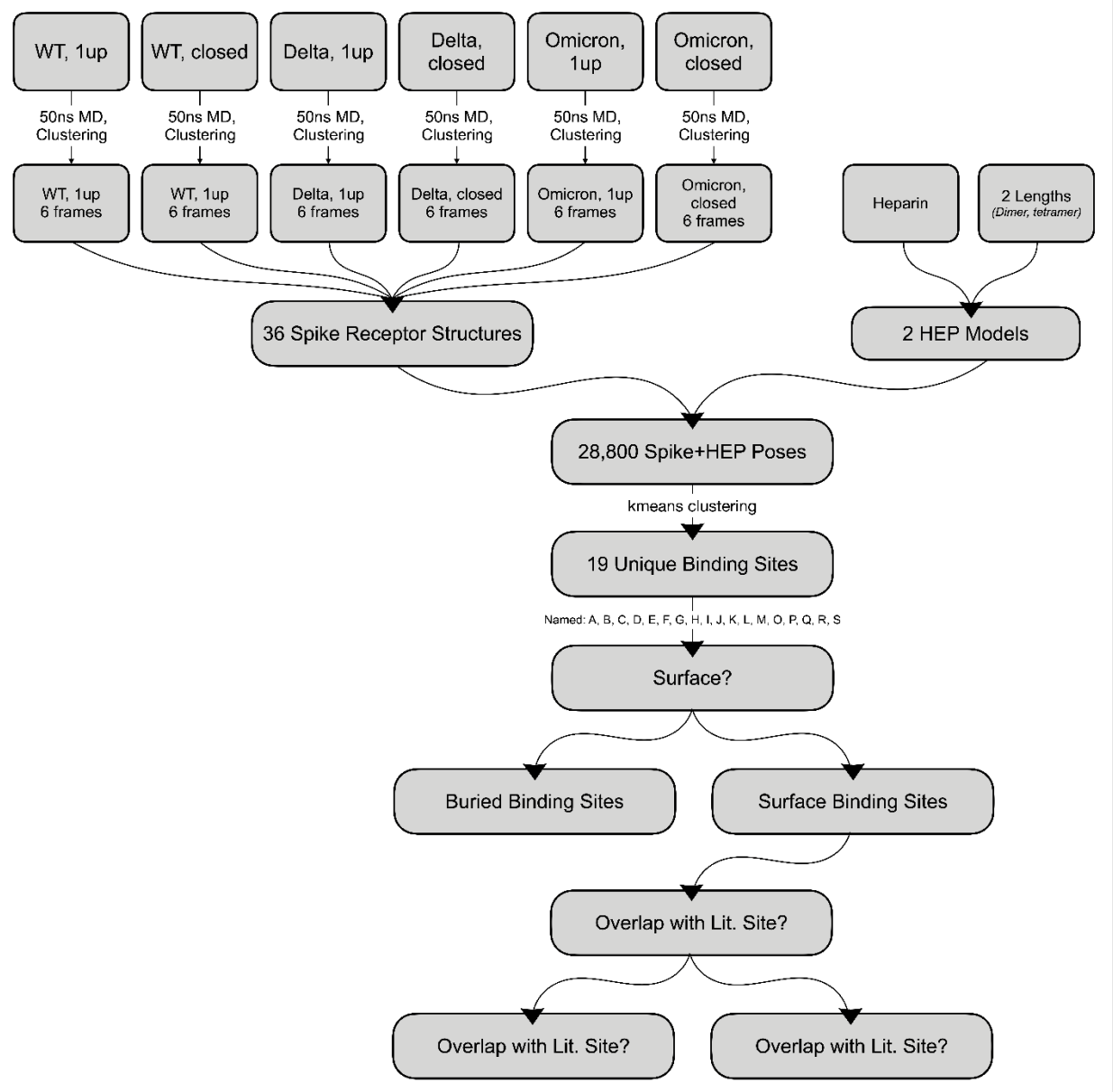

Scheme S1: Schematic outlining variant spike simulation, clustering, and AutoDock Vina procedures as discussed in Computational Methods Sections 2.1.1 to 2.1.2.

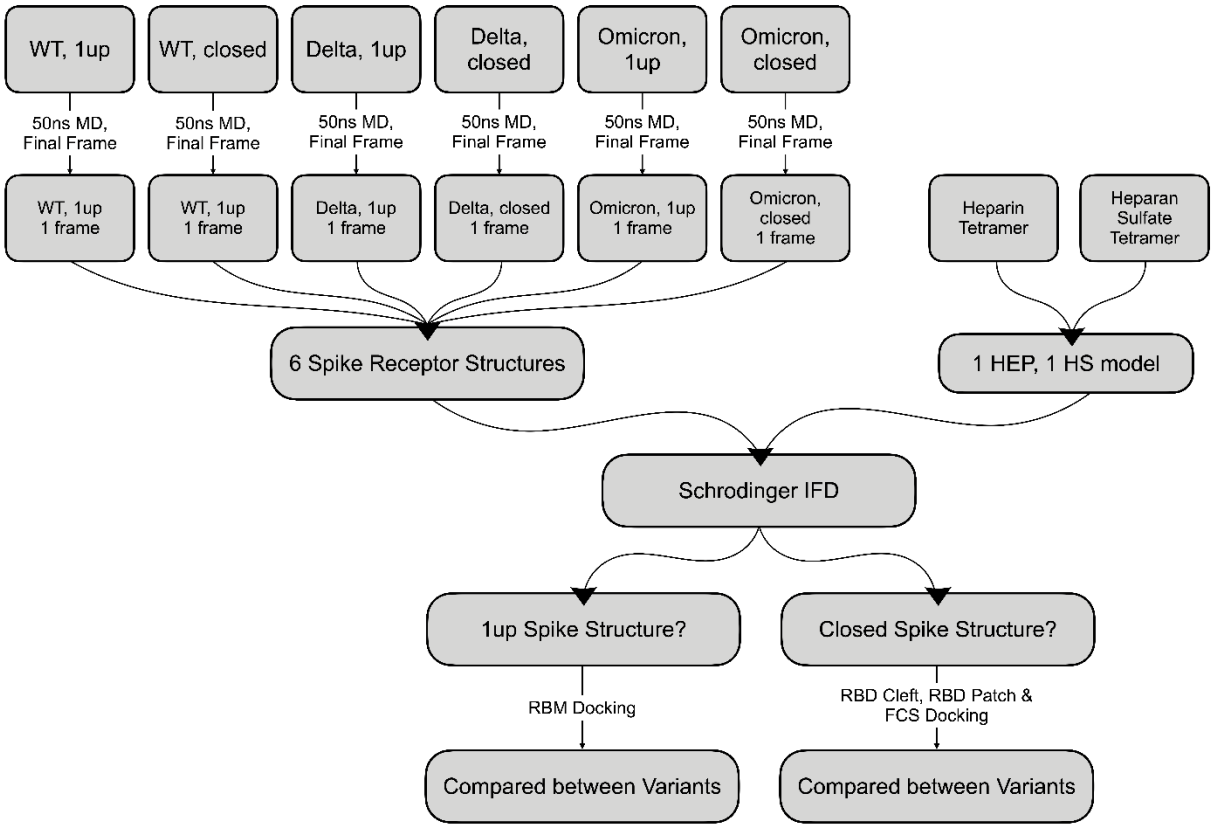

Scheme S2: Schrödinger IFD Methodology at pH 7.4 outlining variant spike simulation, clustering, and Schrödinger IFD procedures as discussed in Computational Methods 2.1.1 and 2.1.3.

Tables:

Table S1: Complete list of all mutations per variant considered for modeling and charge calculations in this work. Glycan contribution calculated according to Watanabe et al.[6] and with glycans chosen consistent to Casalino et al.[8] with 14 sialic acid residues included (total glycan charge of –14).

Variant	Mutations from WT/2019 (charge change relative to WT due to mutation)	ΔT_Q	T_Q
WT			-11
Alpha	ΔH69-V70 (0), ΔY144 (0), A570D (-1), D614G (+1), P681H (0), T716I (0), S982A (0), D1118H (+1)	(+1)*3 = +3	-8
Beta	D80A (+1), D215G (+1), ΔL241-L242-A243 (0), K417N (-1), E484K (+2), N501Y (0), D614G (+1), A701V (0)	(+4)*3 = +12	+1

Delta	T19R (+1), G142D (-1), ΔE156-F157 (+1), R158G (-1), L452R (+1), T478K (+1), D614G (+1), P681R (+1), D950N (+1), ΔN17-Glycan (0)	(+5)*3 = +15	+4
Omicron (BA.1)	A67V (0), ΔH69-V70 (0), T95I (0), G142D (-1), ΔV143-Y144-Y145 (0), ΔN211 (0), L212I, ins214EPE (-2), G338D (-1), S371L (0), S373P (0), S375F (0), K417N (-1), N440K (+1), G446S (0), S466N (0), T478K (+1), E484A (+1), Q493R (+1), G498R (+1), N501Y (0), Y505H (0), T547K (+1), D614G (+1), H655Y (0), N679K (+1), P681H (0), N764K (+1), D796Y (+1), N856K (+1), Q954H (0), N969K (+1), L981F (0)	(+7)*3 = +21	+10

Table S2: Complete list of all titratable residues and their selected protonation states each spike/ACE2 structure to pH = 7.4, as calculated by PROPKA. Full pK_a calculation data can be found in the shared files associated with this supporting information.

pH	Prot	Cnf	P.S.	Residue IDs
7.4	WT	Clo.	ASP	40 53 80 88 111 138 178 198 215 228 253 287 290 294 364 389 398 405 420 427 428 442 467 568 571 574 578 586 614 627 663 767 745 775 796 808 820 830 839 843 848 867 936 950 979 985 994 1041 1084 1118 1127 1139
			ASPP	none
			GLU	96 132 154 156 169 180 191 224 281 598 309 324 340 406 465 471 484 516 554 583 619 654 661 702 725 748 773 780 819 868 918 988 990 1017 1031 1072 1092 1111
			GLUP	none
			HSD	146 207 245 519 1058
			HSE	49 66 69 625 655 1048 1064 1083 1101
			HSP	none
7.4	WT	1up	ASP	40 53 80 88 111 138 178 198 215 228 253 287 290 294 364 389 398 405 420 427 428 442 467 568 571 574 578 586 614 627 663 767 745 775 796 808 820 830 839 843 848 867 936 950 979 985 994 1041 1084 1118 1127 1139
			ASPP	none
			GLU	96 132 154 156 169 180 191 224 281 598 309 324 340 406 465 471 484 516 554 583 619 654 661 702 725 748 773 780 819 868 918 988 990 1017 1031 1072 1092 1111

			GLUP	none
			HSD	146 207 245 519 1058
			HSE	49 66 69 625 655 1048 1064 1083 1101
			HSP	none
7.4	Del	Clo.	ASP	40 53 80 88 111 138 142 178 198 215 228 253 287 290 294 364 389 398 405 420 427 428 442 467 568 571 574 578 586 627 663 737 745 775 796 808 820 830 839 843 848 867 936 979 985 994 1041 1084 1118 1127 1139
			ASPP	none
			GLU	96 132 154 169 180 191 224 281 298 309 324 340 406 465 471 484 516 554 583 619 654 661 702 725 748 773 780 819 868 918 988 990 1017 1031 1072 1092 1111
			GLUP	none
			HSD	519 625 655 1058 1083 1088
			HSE	49 66 69 146 207 245 1048 1064 1101
			HSP	None
7.4	Del	1up	ASP	40 53 80 88 111 138 142 178 198 215 228 253 287 290 294 364 389 398 405 420 427 428 442 467 568 571 574 578 586 627 663 737 745 775 796 808 820 830 839 843 848 867 936 979 985 994 1041 1084 1118 1127 1139
			ASPP	none
			GLU	96 132 154 169 180 191 224 281 298 309 324 340 406 465 471 484 516 554 583 619 654 661 702 725 748 773 780 819 868 918 988 990 1017 1031 1072 1092 1111
			GLUP	none
			HSD	519 625 655 1058 1083 1088
			HSE	49 66 69 146 207 245 1048 1064 1101
			HSP	None
7.4	Omi	Clo.	ASP	40 53 80 88 111 138 142 178 198 215 228 253 287 290 294 339 364 389 398 405 420 427 428 442 467 568 571 574 578 586 627 663 737 745 775 808 820 830 839 843 848 867 936 950 979 985 994 1041 1084 1118 1127 1139

			ASPP	none
			GLU	96 132 154 156 169 180 191 2141 (inserted E) 2143 (inserted E) 224 281 298 309 324 340 406 465 471 516 554 583 619 654 661 702 725 748 773 780 819 868 918 988 990 1017 1031 1072 1092 1111
			GLUP	None
			HSD	146 207 245 519 681 1058 1088
			HSE	49 66 505 625 954 1048 1064 1083 1101
			HSP	none
7.4	Omi	1up	ASP	40 53 80 88 111 138 142 178 198 215 228 253 287 290 294 339 364 389 398 405 420 427 428 442 467 568 571 574 578 586 627 663 737 745 775 808 820 830 839 843 848 867 936 950 979 985 994 1041 1084 1118 1127 1139
			ASPP	none
			GLU	96 132 154 156 169 180 191 2141 (inserted E) 2143 (inserted E) 224 281 298 309 324 340 406 465 471 516 554 583 619 654 661 702 725 748 773 780 819 868 918 988 990 1017 1031 1072 1092 1111
			GLUP	None
			HSD	146 207 245 519 681 1058 1088
			HSE	49 66 505 625 954 1048 1064 1083 1101
			HSP	none
7.4	ACE2	--	ASP	30 38 67 111 136 157 198 201 206 213 216 225 269 292 295 299 303 335 350 355 367 368 382 427 431 471 494 499 509 543 597 609 615 630 637 669 693 713 719
			ASPP	none
			GLU	22 23 35 37 56 57 75 87 110 140 145 150 160 166 171 181 182 189 197 208 224 227 231 232 238 310 312 329 375 398 402 406 430 433 435 457 467 479 483 489 495 527 536 549 564 571 589 634 639 667 668 699 701 723
			GLUP	none
			HSD	34 195 239 373 374 378 417 493
			HSE	228 241 265 345 401 505 535 540
			HSP	none

Prot. = protein. Cnf = conformational state, relevant to spike protein structures only. P.S. = protonation state. Clo. = spike in closed conformational state. 1up = spike in 1up/open conformational state. WT = Wild Type. Del. = Delta. Omi. = Omicron. ACE2 = angiotensin converting enzyme 2. ASP = deprotonated/negatively charged aspartate. ASPP = protonated/neutral aspartate. GLU = deprotonated/negatively charged glutamate. GLUP = protonated/neutral glutamate. HSD = singly protonated/neutral histidine with protonation on the N_δ atom. HSE = singly protonated/neutral histidine with protonation on the N_ε atom. HSP = double protonated/positively charged histidine with protonation on N_δ and Nε atoms.

Table S3: Complete list of protein residues per GAG binding hotspot as predicted by ensemble-based docking with AutoDock and Kmeans clustering.

Site	Protein Residues: Residue Name, Residue Number, Chain ID Glycans: Glycan Protein Residue Name, Protein Residue Number, (Protein Chain ID)
A	Arg403A, Asp405A, Glu406A, Asn417A, Lys417A, Tyr421A, Ser443A, Lys444A, Val445A, Gly446A, Asn448A, Tyr449A, Tyr451A, Leu452A, Tyr453A, Leu455A, Phe456A, Lys458A, Ser459A, Asn460A, Lys462A, Ser477A, Phe490A, Leu492A, Gln493A, Arg493A, Ser494A, Tyr495A, Ser496A, Phe497A, Gly496A, Gln498A, Arg498A, Pro499A, Thr500A, Asn501A, Tyr501A, Gly502A, Val503A, Gly504A, Tyr505A, His505A, Gln506A, Pro507A, Phe342B, Asn343B, Tyr369B, Asn370B, Leu371B, Ser371B, Ala372B, Ser373B, Pro373B, Ser375B, Phe375B, Phe374B, Trp436B, Asn437B, Ser438B, Asn439B, Asn440B, Lys440B, Leu441B, Gly447B, Glycan N343(B)
B	Ser49B, Arg346B Phe347B, Ala348B, Val350B, Tyr351B, Ala352B, Trp353B, Leu371C, Ala372C, Phe374C, Phe400B, Val401B, Ile402B, Arg403B, Glu406B, Gly416B, Lys417B, Asn417B, Ile418B, Ala419B, Tyr421B, Asn422B, Tyr423B, Leu441B, Asp442B, Ser443B, Lys444B, Gly447B, Asn448B, Tyr449B, Asn450B, Tyr451B, Leu452B, Arg452B, Tyr453B, Arg454B, Leu455B, Phe456B, Arg457B, Leu461B, Thr470B, Glu471B, Tyr473B, Tyr489B, Phe490B, Pro491B, Leu492B, Gln493B, Arg493B, Ser494B, Tyr495B, Gly496B, Ser496B, Phe497B, Gln498B, Asn501B, Tyr501B, Tyr505B, His505B, Pro507B, Glycan N165(C), Glycan N343(C)
C	Asn370A, Ser371A, Ser373A, Phe377A, Lys378A, Cys379A, Tyr380A, Gly381A, Val382A, Ser383A, Pro384A, Thr385A, Lys386A, Ala411A, Pro412A, Gln414A, Asp427A, Asp428A, Phe429A, Thr430A, Gly431A, Leu517A, Tyr51C, Ser349C, Val350C, Ala352C, Ile402C, Arg403C, Glu406C, Gly416C, Asn417C, Lys417C, Ile418C, Ala419C, Asp420C, Tyr421C, Asn422C, Tyr423C, Tyr449C, Asn450C, Tyr451C, Leu452C, Arg452C, Tyr453C, Arg454C, Leu455C, Phe456C, Lys458C, Ser459C, Leu461C, Asp467C, Ile468C, Arg469C, Thr470C, Glu471C, Ile472C, Tyr473C, Gln474C, Ala475C, Glu484C, Cys488C, Tyr489C, Phe490C, Pro491C, Leu492C, Gln493C, Arg493C, Ser494C, Tyr495C, Gly496C, Ser496C, Phe497C, Tyr501C, Glycan N165(A), Glycan N343(A)
D	Ser13C, Cys15C, Val16C, Leu18C, Ala67C, Val67C, Ile68C, His69C, Ser71C, Phe79C, Arg78C, Asn81C, Glu96C, Lys97C, Ser98C, Asn99C, Ile100C, Ile101C, Arg102C, Gly103C, Leu118C, Val120C, Asn121C, Asn122C, Pro139C, Ala123C, Thr124C, Asn125C, Val127C, Asp138C, Pro139C, Phe140C, Leu141C, Asp142C, Gly142C, Val143C, Tyr144C, Tyr145C, His146C, Lys147C, Asn148C, Asn149C, Lys150C, Ser151C, Trp152C, Met153C, Glu154C, Gly156C,

	Ser155C, Glu156C, Phe157C, Arg158C, Val159C, Phe175C, Leu176C, Met177C, Asp178C, Leu179C, Glu180C, Gly181C, Lys182C, Gln183C, Arg190C, Thr240C, Leu241C, Leu242C, Ala243C, Leu244C, His245C, His245C, Arg246C, Ser247C, Tyr248C, Leu249C, Thr250C, Ser254C, Gly257C, Trp258C, Thr259C, Ala260C, Gly261C, Ala262C, Ala263C, Glycan N122(C), Glycan N149(C)
E	Asp420A, Tyr421A, Phe456A, Arg457A, Lys458A, Ser459A, Asn460A, Thr385B, Lys386B, Asn388B, Asp389B, Pro527B, Lys528B, Thr415A, Gly416A, Tyr473A, Asp364B, Ser366B, Gly526B, Lys529B, Tyr369B, Asn370B, Val367B, Leu455A, Leu461A, Leu387B, Tyr453A, Arg454A, Pro384B, Lys417A, Ile418A, Tyr489A, Asp985C, Tyr365B, Lys462A, Val327B, Lys424A, Pro463A, Leu371B, Glycan N234(B), Glycan N343(B), Glycan T323(B)
F	Pro330B, Ile332B, Arg357B, Ile358B, Ser359B, Asn360B, Cys361B, Phe392B, Thr393B, Asn394B, Val395B, Tyr396B, Glu516B, Leu518B, His519B, Ala520B, Pro521B, Ala522B, Thr523B, Val524B, Asn544B, Leu560B, Pro561B, Phe562B, Gln563B, Gln564B, Arg577B, Leu582B, Lys41C, Ile128C, Phe168C, Glu169C, Tyr170C, Val171C, Ser172C, Gln173C, Pro174C, Phe175C, Tyr200C, Lys202C, Pro225C, Leu226C, Val227C, Asp228C, Leu229C, Pro230C, Glycan N331(B), Glycan N122(C)
G	Ile119A, Thr124A, Asn125A, Val126A, Val127A, Ile128A, Phe168A, Glu169A, Tyr170A, Val171A, Ser172A, Gln173A, Pro174A, Phe175A, Leu179A, Ile203A, Leu226A, Val227A, Asp228A, Leu229A, Pro230A, Arg357C, Ser359C, Asn360C, Asn394C, Tyr396C, Thr523C, Glycan N122(A), Glycan N149(A), Glycan N331(C),
H	Arg357A, Ser359A, Asn360A, Thr393A, Asn394A, Ala520A, Pro521A, Ala522A, Thr523A, Pro561A, Phe562A, Lys41B, Leu117B, Ile119B, Val120B, Asn121B, Thr124B, Asn125B, Val126B, Val127B, Ile128B, Lys129B, Val130B, Phe168B, Glu169B, Tyr170B, Val171B, Ser172B, Gln173B, Pro174B, Phe175B, Leu176B, Met177B, Leu179B, Phe192B, Tyr200B, Phe201B, Lys202B, Ile203B, Tyr204B, Ser205B, Glu224B, Pro225B, Leu226B, Val227B, Asp228B, Leu229B, Pro230B, Ile231B, Gly232B, Glycan N331(A), Glycan N122(B), Glycan N282(B)
I	Ser325A, Val327A, Val382A, Ser383A, Thr385A, Lys386A, Leu387A, Asn388A, Asp389A, Leu390A, Leu518A, Lys528A, Asn540A, Phe541A, Asn542A, Gly545A, Leu546A, Thr547A, Gly548A, Glu748B, Asn978B, Ile980B, Leu981B, Ser982B, Arg983B, Leu984B, Asp985B, Lys986B, Ala989B, Thr747B, Asp979B, Ser746B, Phe329A, Leu977B, Phe543A, Asn544A, Thr549A, Val976B, Ile326A, Val987B, Glu988B, Ile993B, Pro322A, Glu324A, Asp745B, Lys417C, Gln321A, Thr323A, Val539A, Lys547A, Phe981B, Arg328A, Gly550A, Glucan T323(A), Glycan S325(A), Glycan N234(A)
J	Gln52B, Thr274B, Gln271B, Arg273B, Asp290B, Cys291B, Ala292B, Leu293B, Glu298B, Ser316B, Asn317B, Phe318B, Arg319B, Val320B, Gln321B, Pro322B, Thr323B, Glu324B, Lys537B, Cys538B, Asn540B, Thr549B, Val551B, Cys590B, Ser591B, Phe592B, Gly593B, Val595B, Tyr612B, Glu619B, Val620B, Pro621B Val622B, Ala623B, Ile624B, His625B, Ala626B, Asp627B, Gln628B, Leu629B, Thr630B, Pro631B, Thr632B, Trp633B, Arg634B, Val635B, Met740C, Asp745C, Thr747C, Glycan N234(B), Glycan T323(B)

K	Asp737A, Cys738A, Thr739A, Met740A, Ile742A, Cys743A, Gly744A, Asp745A, Ser746A, Thr747C, Glu748A, Cys749A, Ser750A, Asn751A, Leu752A, Leu753A, Leu754A, Gln755A, Tyr756A, Phe759A, Gly757A, Ser758A, Cys760A, Thr761A, Lys764A, Ile993A, Ile997A, Leu1001A, Ser50C, Gln52C, Asp53C, Pro272C, Thr274C, Glu298C, Lys304C, Ser316C, Asn317C, Phe318C, Arg319C, Thr302C, Phe592C, Thr630C, Glycan N234(C)
L	Leu24B, Pro25B, Pro26B, Ala27B, Tyr28B, Thr29B, Asn30B, Asn61B, Val62B, Thr63B, Trp64B, Phe65B, His66B, Ile68B, Val70B, Arg78B, Val213B, Arg214B, Asp215B, Tyr266B, Leu212B, ins-Glu2141B, ins-Pro2142B, ins-Glu2143B, Glycan N61(B), Glycan N74(B), Glycan N603(B)
M	Val47B, Leu48B, His49B, Ser50B, Thr51B, Gln52B, Thr274B, Leu276B, Val289B, Cys291B, Pro295B, Ser297B, Glu298B, Thr299B, Lys300B, Cys301B, Thr302B, Leu303B, Lys304B, Ser305B, Phe306B, Thr307B, Val308B, Tyr313B, Gln314B, Thr315B, Ser316B, Asn317B, Phe318B, Ile569A, Trp633B, Arg634B, Cys738C, Thr739C, Leu753C, Leu754C, Tyr756C, Gly757C, Ser758C, Phe759C, Cys760C, Thr761C, Gln762C, Leu763C, Lys764C, Asn764C, Arg765C, Gln957B, Asn960B, Thr961B, Lys964B, Gln965B, Ser968B, Ser967B,
N	Leu48A, His49A, Ser50A, Thr51A, Thr274A, Phe275A, Leu276A, Leu277A, Val289A, Cys291A, Ser297A, Glu298A, Thr299A, Lys300A, Cys301A, Thr302A, Leu303A, Lys304A, Ser305A, Phe306A, Thr315A, Thr961A, Lys964A, Leu754B, Gly757B, Ser758B, Cys760B, Thr761B, Asn764B, Gln52A, Leu296A, Ser316A, Arg765B, Asp290A, Ala292A, Phe759B, Gln762B, Thr739B, Leu753B, Val308A, Asp294A, Pro295A, Gln314A, Thr307A, Gln957A, Gln755B, Tyr756B, Tyr313A, Val597A, Gln965A, Cys738B, Lys764B, Asn317A, Phe318A, Ile569C Leu849A, Glycan N234(A), Glycan T323(A)
O	Ile834A, Ile312C, Val595C, Ser596C, Ile598C, Val608C, Ala609C, Val610C, Leu611C, Tyr612C, Gln613C, Gly614C, Val615C, Asn616C, Cys617C, Thr618C, Glu619C, Val620C, Pro621C, Val622C, Ala623C, Ile624C, Leu629C, Thr630C, Pro631C, Thr632C, Trp633C, Arg634C, Val635C, Tyr636C, Ser637C, Thr638C, Gly639C, Ser640C, Asn641C, Val642C, Phe643C, Gln644C, Thr645C, Arg646C, Ala647C, Gly648C, Cys649C, Leu650C, Ile651C, Gly652C, Ala653, Glu654C, His655C, Tyr655C, Val656C, Ile666C, Ile670C, Cys671C, Ala672C, Gln675C, Arg682C, Arg683C, Ser686C, Ala688C, Ser689C, Gln690C, Ser691C, Ile692C, Ile693C, Ala694C, Tyr695C, Glycan N616(C), Glycan N657(C)
P	Asn616B, Gln644B, Thr645B, Arg646B, Ala647B, Gly648B, Ala668B, Gly669B, Ile670B, Pro812C, Ser813C, Lys814C, Arg815C, Phe823C, Leu828C, Ala829C, Asp830C, Ala831C, Gly832C, Phe833C, Ile834C, Lys835C, Gln836C, Tyr837C, Pro862C, Pro863C, Leu865C, Thr866C, Asp867C, Glu868C, Met869C, His1058C, Glycan N616(B), Glycan N657(B), Glycan N282(C)
Q	Ala609A, Val610A, Leu611A, Tyr612A, Val615A, Asn616A, Cys617A, Thr618A, Glu619A, Val620A, Pro621A, Leu629A, Thr632A, Gly639A, Ser640A, Asn641A, Val642A, Phe643A, Gln644A, Thr645A, Gly648A, Cys649A, Leu650A, Ile651A, Gly652A, Ala653A, Glu654A, His655A, Val656A, Ile670A, Arg682A, Ala694A, Thr630A, Arg646A, Gln628A, Ile666A, His655A, Arg634A, Asn657A, Arg681A, Arg683A, Ile693A, Tyr695A, Thr638A, His625A, Thr696A, Ala623A, Ser686A, Ser691A, Ile692A, Tyr655A, Glycan N616(A), Glycan N657(A)

R	Leu1024A, Thr1027A, Lys1028A, Glu1031A, Ser1037A, Lys1038A, Arg1039A, Val1040A, Asp1041A, Phe1042A, Cys1043A, Glu780B, Val781B, Gln784B, Ala1020B, Ser1021B, Ala1022B, Asn1023B, Leu1024B, Ala1025B, Ala1026B, Thr1027B, Lys1028B, Met1029B, Ser1030B, Glu1031B, Cys1032B, Val1033B, Leu1034B, Ser1037B, Arg1039B, Phe1042B, Thr1027C, Glu1031C, Arg1039C, Cys1032A, Leu727B, Cys1043B, Gly1035B, Phe1062B, Trp886B, Asn1023C, Ser1030C, Gln1036B, Lys1038B, His1064B, Phe1042C, Gly1044A, Lys1045A, Glu725A
S	Val722C, Gly799C, Phe800C, Asn801C, Phe802C, Ser803C, Gln804C, Ile805C, Gln920C, Lys921C, Leu922C, Ile923C, Ala924C, Asn925C, Gln926C, Phe927C, Asn928C, Ser929C, Ala930C, Ile931C, Gly932C, Lys933C, Ile934C, Gln935C, Asp936C, Glycan N709 (B), Glycan N717(C), Glycan N801(C)

Table S4: Fraction of each group measured by mass photometer for Omicron ternary complex with or without heparan sulfate.

Group / Sample	A (fraction)	B (fraction)	C (fraction)
Omicron + ACE2	0.448	0.215	0.337
Omicron + ACE2	0.453	0.240	0.307
Omicron + ACE2	0.428	0.236	0.336
Average (Standard Deviation)	0.443 (0.014)	0.230 (0.013)	0.327 (0.017)
Group / Sample	A (fraction)	B (fraction)	C (fraction)
Omicron + HS + ACE2	0.468	0.395	0.137
Omicron + HS + ACE2	0.349	0.469	0.181
Omicron + HS + ACE2	0.316	0.488	0.195
Average (Standard Deviation)	0.378 (0.080)	0.451 (0.050)	0.171 (0.030)

Table S5: Fraction of each group measured by mass photometer for Delta ternary complex with or without heparan sulfate.

Group / Sample	A (fraction)	B (fraction)	C (fraction)
Delta + ACE2	0.447	0.147	0.406
Delta + ACE2	0.438	0.152	0.409
Delta + ACE2	0.421	0.174	0.405
Average (Standard Deviation)	0.435 (0.013)	0.158 (0.014)	0.407 (0.002)
Group / Sample	A (fraction)	B (fraction)	C (fraction)
Delta + HS + ACE2	0.507	0.145	0.348
Delta + HS + ACE2	0.473	0.155	0.372
Delta + HS + ACE2	0.545	0.191	0.264
Average (Standard Deviation)	0.508 (0.036)	0.163 (0.024)	0.328 (0.057)

Table S6: Fraction of each group measured by mass photometer for WT ternary complex with or without heparan sulfate.

Group / Sample	A (fraction)	B (fraction)	C (fraction)
WT + HS + ACE2	0.573	0.312	0.115
WT + HS + ACE2	0.697	0.224	0.079
WT + HS + ACE2	0.597	0.254	0.150
Average (Standard Deviation)	0.622 (0.066)	0.263 (0.045)	0.115 (0.035)
Group / Sample	A (fraction)	B (fraction)	C (fraction)
WT + HS + ACE2	0.517	0.336	0.147
WT + HS + ACE2	0.641	0.209	0.150
WT + HS + ACE2	0.553	0.276	0.171
Average (Standard Deviation)	0.570 (0.064)	0.274 (0.064)	0.156 (0.013)

Table S7: Comparison of the limit of detection for spike protein detection in lateral flow assay

Target	**Bioreceptor**	**Detection type**	**Limit of Detection (ng/reaction)**	**Ref.**
Spike	Primary: ACE2 Secondary: Antibody	sandwich-type	5 ng/reaction (buffer)	Lee2020[42]

Spike	Primary: NeuNAc[a] Secondary: NueNAc-PHEA$_{50}$[b]	sandwich-type	200 ng/reaction	Baker2020[43]
Spike	Primary: ACE2 Secondary: Antibody	sandwich-type	1 ng/reaction (buffer)	Lee2022[44]
Spike	Primary: Heparin Secondary: NTD Ab	sandwich-type	19.5 ng/reaction (buffer) 78 ng/reaction (saliva)	Kim2022[22]
Spike	Primary: Heparin Secondary: ACE2	Sandwich-type	10 ng/reaction (buffer) 20 ng/reaction (saliva)	In this study

Figures:

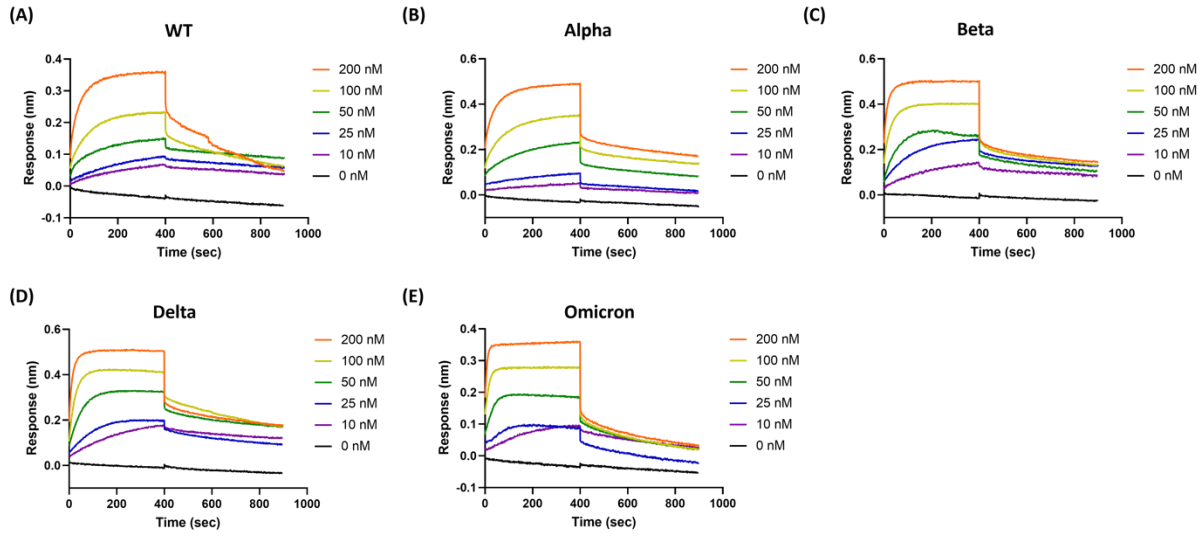

Figure S1: BLI sensogram of the ACE2 binding to variant of SARS-CoV-2 spike proteins (A) Wild type, (B) Alpha, (C) Beta, (D) Delta, and (E) Omicron. ACE2 binding to 0, 10, 25, 50, 100, 200 nM of spike proteins for each variant were measured. Control sample (0 nM) was subtracted to analyze the binding affinity using the steady-state analysis.

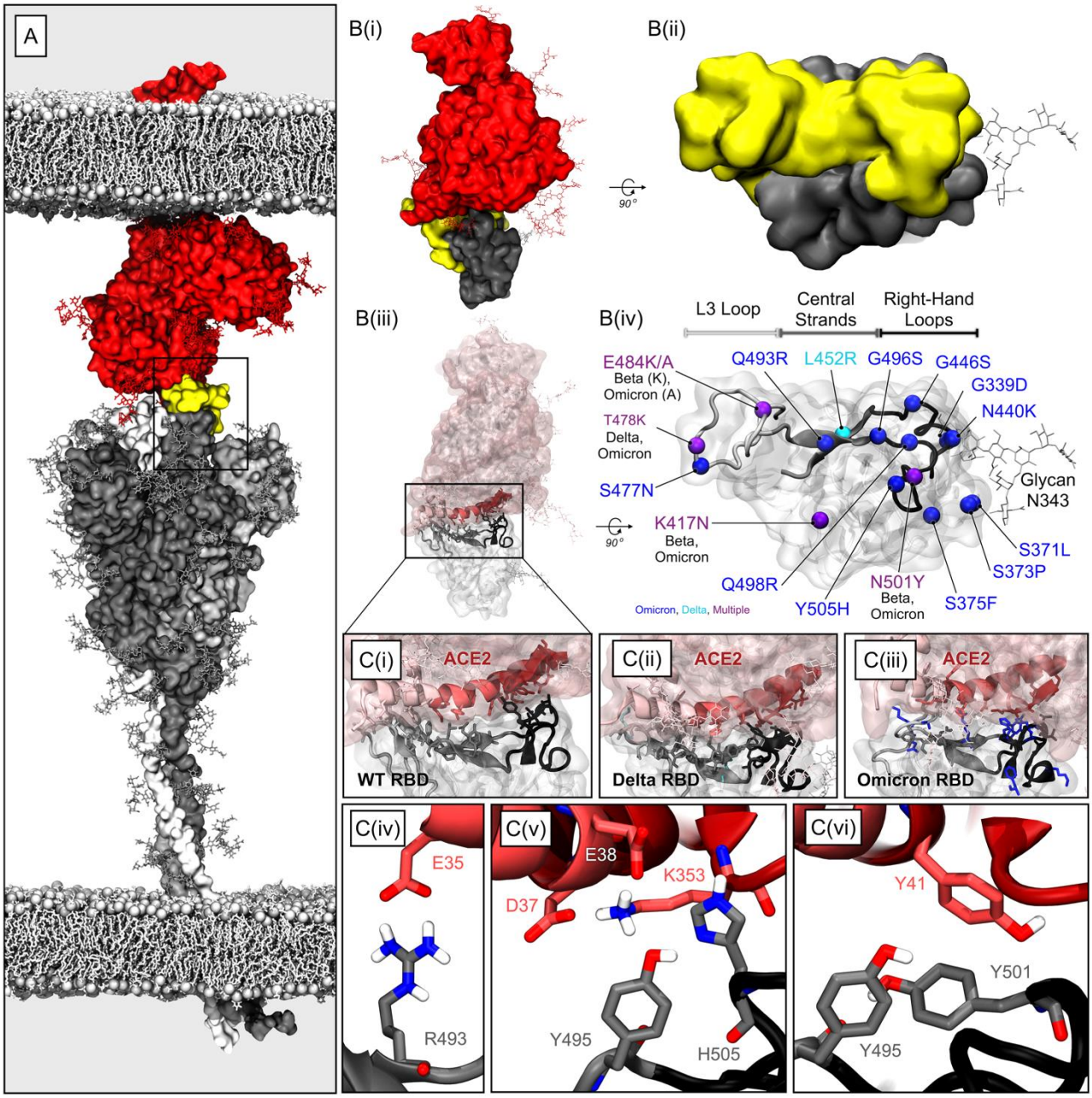

Figure S2: Image of (A) the spike/ACE2 double membrane complex.[44] ACE2 shown in dark red surface representation, ACE2 glycans shown in dark red licorice; SARS-CoV-2 spike protein in 1up conformation is shown in a grey surface representation (chain A as dark grey, chain B as light grey, chain C as white), the spike's exposed RBM is highlighted with a yellow surface, spike glycans shown in grey licorice; human and SARS-CoV-2 membranes are shown in grey licorice representation with phosphorous atoms represented in VDW. A rectangular box outlines the ACE2+RBM interface. (B(i)) Image showing the ACE2+RBD system constructed in this work for MD simulations. All molecules colored and represented as described in panel A. (B(ii)) Spike RBD with RBM highlighted. Spike RBD in grey surface representation, RBM highlighted in yellow. N-linked glycan at N343 shown in grey licorice representation. (B(iii)) Same system as shown in B(i) but with transparent surfaces to highlight the secondary

structure at the ACE2+RBD interface. ACE2 surface is shown in transparent red, with ACE2 glycans shown in pink licorice, spike RBD surface is shown in transparent grey with glycan N343 shown in grey licorice. The RBD side of the ACE2+RBD interface is represented in opaque ribbons and colored in shades of grey; the L3 Loop (residues 470-489), central beta strands (residues 450-456, 490-496), and right-handed loops (residues 438-450, 497-508) are colored as light grey, grey, and black ribbons, respectively. The ACE2 side of the ACE2+RBD interface is composed largely of one N-terminal alpha helix (residues 18-50), a neighboring helix (residues 82-83), and a neighboring beta-strand (residues 353-357). ACE2 residues within the ACE2+RBD interface that interact primarily with the RBD L3 loops, RBD central beta strands, and RBD right-handed loops are represented as pink, red, and dark red ribbons, respectively. A callout box highlights the ACE2+RBD interface. (B(iv)) Spike RBD shown in same orientation as shown in B(ii) but with transparent surface to reveal the positions of mutations in Beta, Delta, and Omicron BA.1 SARS-CoV-2 variant spike sequences. The L3 Loop, central beta strands, and right-handed loops are represented as in B(iii). Positions of mutations seen in the Delta and Omicron spike sequences are shown as cyan and blue beads, respectively, while positions of mutations seen in multiple spike sequences are shown as purple beads with denotation of sequence. Glycan N343 is represented in grey licorice. (C(i-iii)) Visualization of WT, Delta, and Omicron RBDs bound to ACE2. Secondary structural elements at the ACE2+RBD interface are represented in panels B(iii) and B(iv). Cyan and blue residues indicate positions of mutation within the Delta and Omicron spike sequences, respectively. (C(iv-vi)) Zoom-in images highlighting specific interactions of high interest observed in ACE2+Omicron spike RBD simulations as discussed in the main text. Red carbon atoms denote ACE2 residues, grey carbon atoms denote Omicron RBD residues.

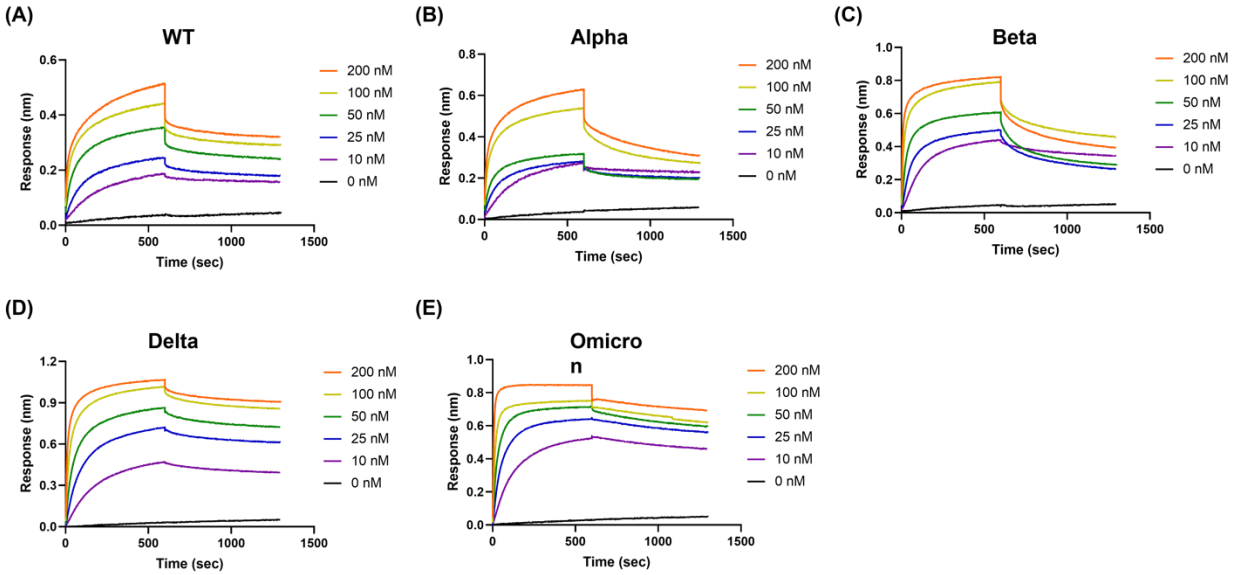

Figure S3: BLI sensogram of the heparin (HEP) binding to variant of SARS-CoV-2 spike proteins (A) Wild type, (B) Alpha, (C) Beta, (D) Delta, and (E) Omicron. HEP binding to 0, 10, 25, 50, 100, 200 nM of spike proteins for each variant were measured. Control sample (0 nM) was subtracted to analyze the binding affinity using the steady-state analysis.

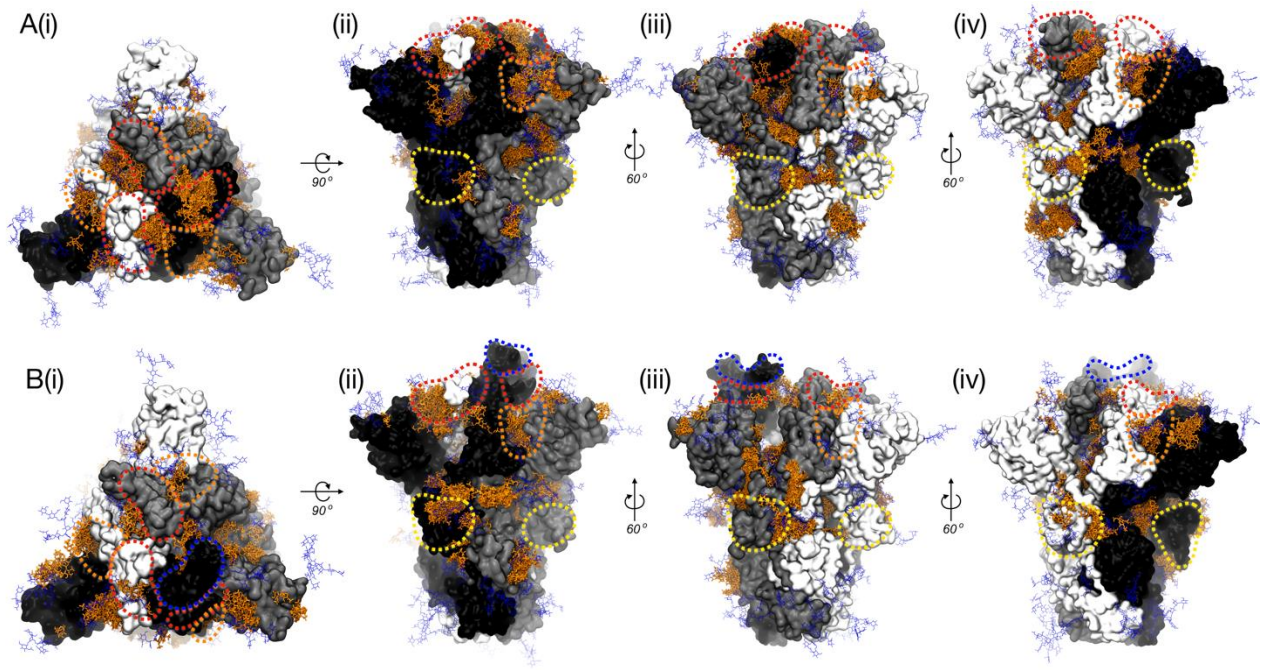

Figure S4: AutoDock Vina docking results illustrating heparin dimeric and tetrameric models bound to WT (A) closed and (B) 1-up structures. In all structures, spike chains A, B, and C are shown in black, grey, and white surface representations. Spike glycans are shown in thin blue licorice. Heparin dimeric and tetrameric binding modes are shown in orange licorice. Subpanels (i-iv) each represent the same structure in a different orientation. In all images, red, orange, yellow, and blue dotted lines highlight the RBD patch, RBD cleft, FCS, and RBM sites respectively.

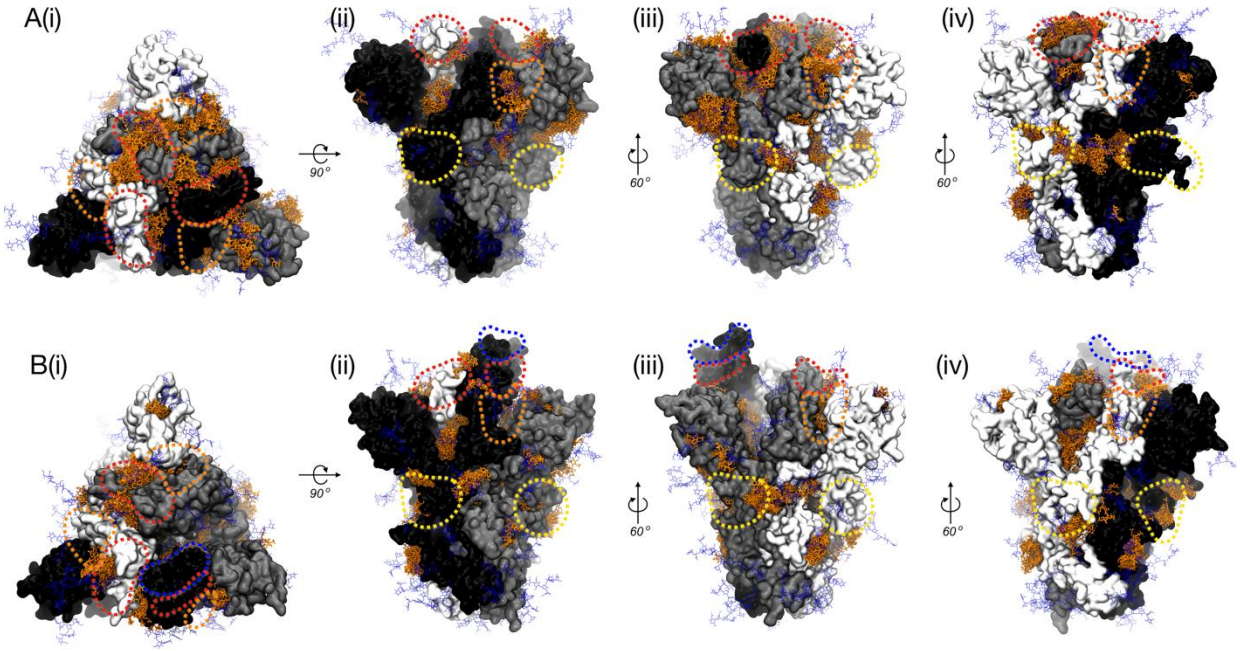

Figure S5: AutoDock Vina docking results illustrating heparin dimeric and tetrameric models bound to Delta (A) closed and (B) 1-up structures. In all structures, spike chains A, B, and C are shown in black, grey,

and white surface representations. Spike glycans are shown in thin blue licorice. Heparin dimeric and tetrameric binding modes are shown in orange licorice. In all images, red, orange, yellow, and blue dotted lines highlight the RBD patch, RBD cleft, FCS, and RBM sites respectively.

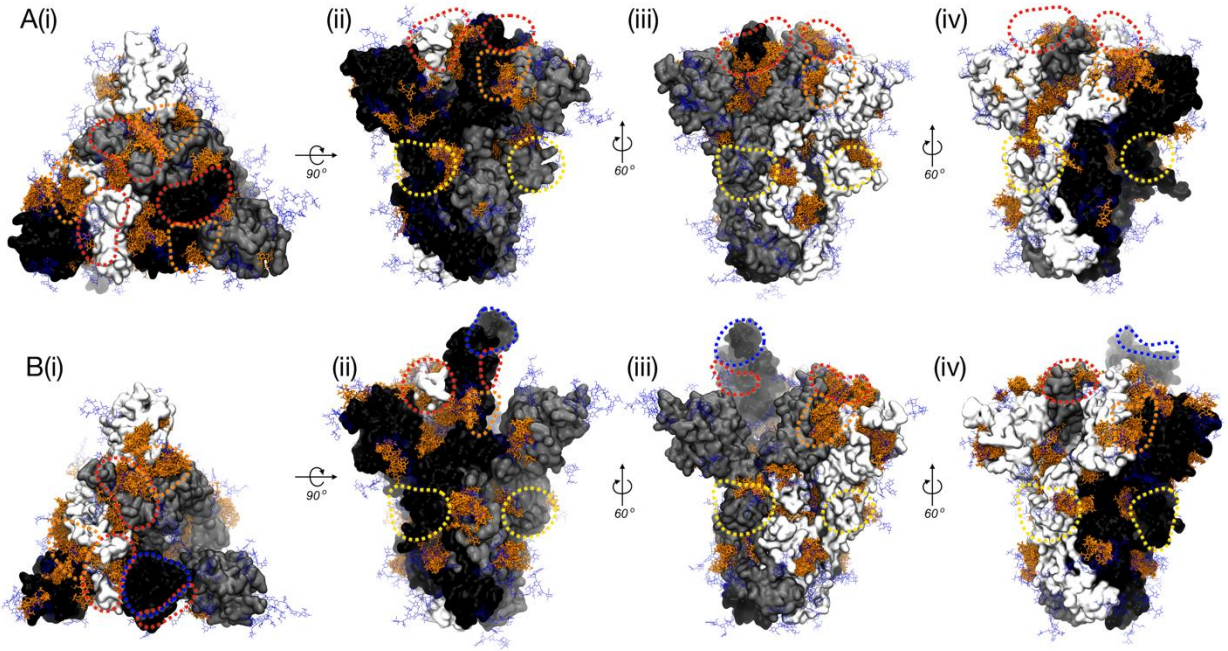

Figure S6: AutoDock Vina docking results illustrating heparin dimeric and tetrameric models bound to Omicron (A) closed and (B) 1-up structures. In all structures, spike chains A, B, and C are shown in black, grey, and white surface representations. Spike glycans are shown in thin blue licorice. Heparin dimeric and tetrameric binding modes are shown in orange licorice. In all images, red, orange, yellow, and blue dotted lines highlight the RBD patch, RBD cleft, FCS, and RBM sites respectively.

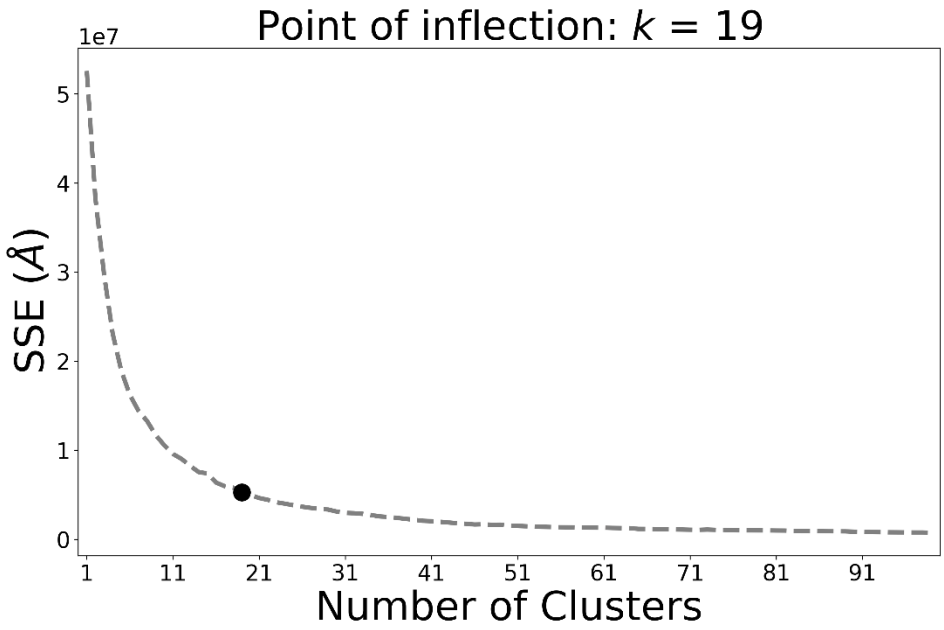

Figure S7: K-means clustering results determining the optimal number of clusters from 28,800 AutoDock vina binding modes.

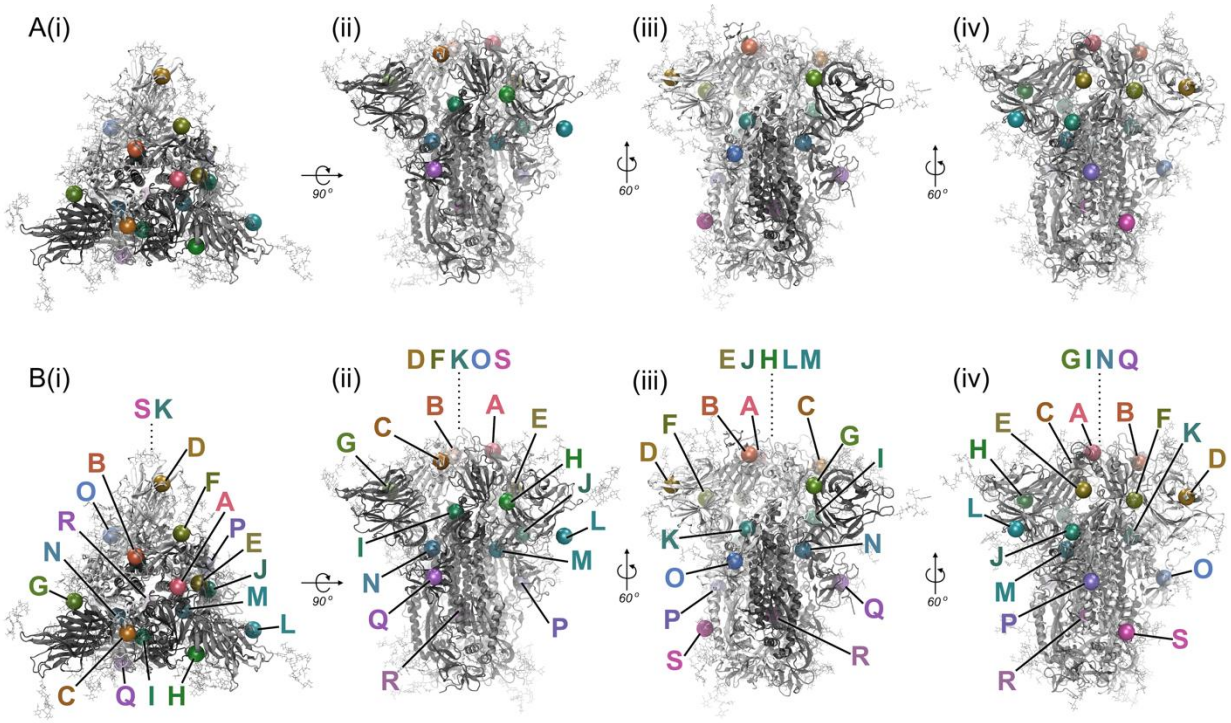

Figure S8: All 19 heparin hotspots found via ensemble-based docking with AutoDock and kmeans clustering. (A) Panels (i-iv) show the WT spike protein in closed conformation; chains A, B, and C are represented in grey, light grey, and white ribbons, respectively, and spike glycans are represented in light grey licorice. The centroid of each identified "hotspot" is represented with a 5Å sphere. The hotspots were ordered by height on the spike protein (i.e., according to z-coordinate) and colored according to a rainbow color palette. All images are based on an identical structure and VMD scene but rotated to give complete viewing of spike apex (i) and three sides (ii-iv). (B) Panels (i-iv) show the same WT spike protein in closed conformation with the same representation scheme as in (A), but with each identified binding hotspot labeled according to its name A-R. Hotspots were named as described in Supporting Information methods. Sites not visible in a given orientation, due to rotation or fog in the image, are denoted with a dashed line.

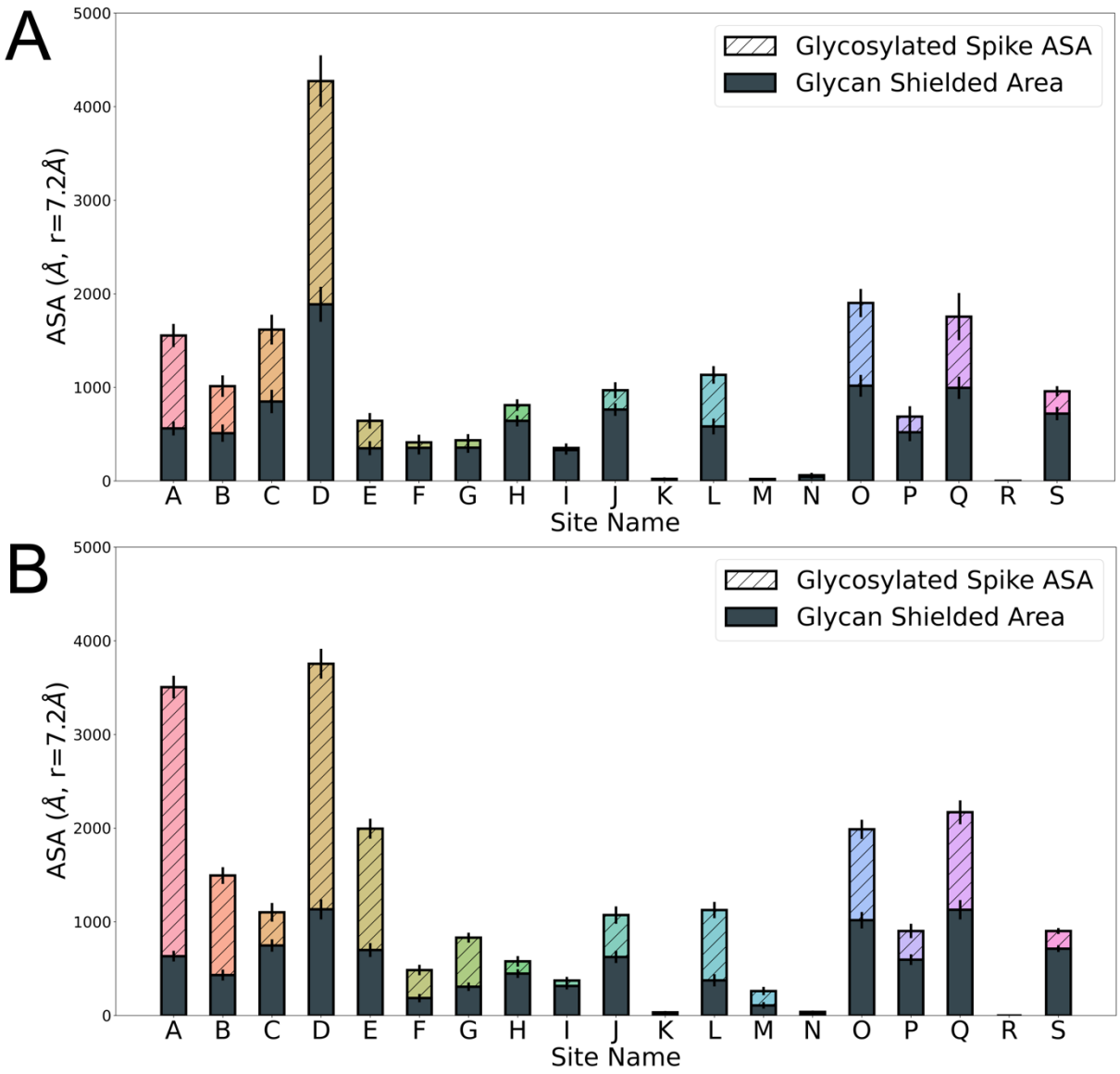

Figure S9: Accessible Surface Area plotted for each site calculated with a probe radius of 7.2 Å, calculated according to the Shrake-Rupley algorithm. (A) ASAs calculated for each binding site from wild type spike simulations in the all-RBDs-down/closed conformation. (B) ASAs calculated for each binding site from wild type spike simulations in the 1-up RBD conformation.

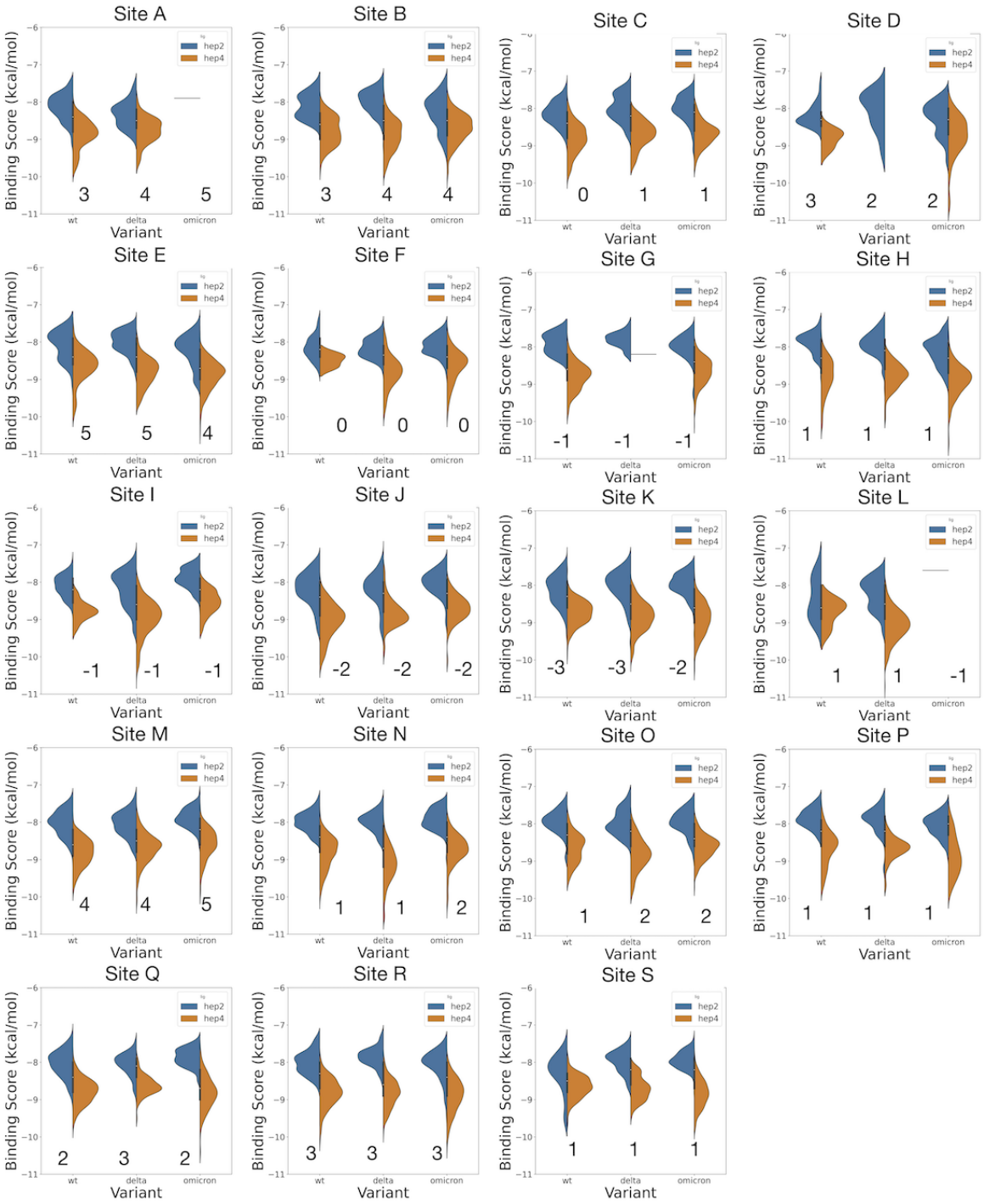

Figure S10: Violin plots demonstrating distribution of AutoDock Vina binding scores for heparin dimer (hep2) and tetramer (hep4) models each binding hotspot across all variants. Total charge per site per variant is denoted next to each violin within the plot. Site based distributions of AutoDock Vina binding scores were taken from both closed and 1up spike conformations per variant within each site.

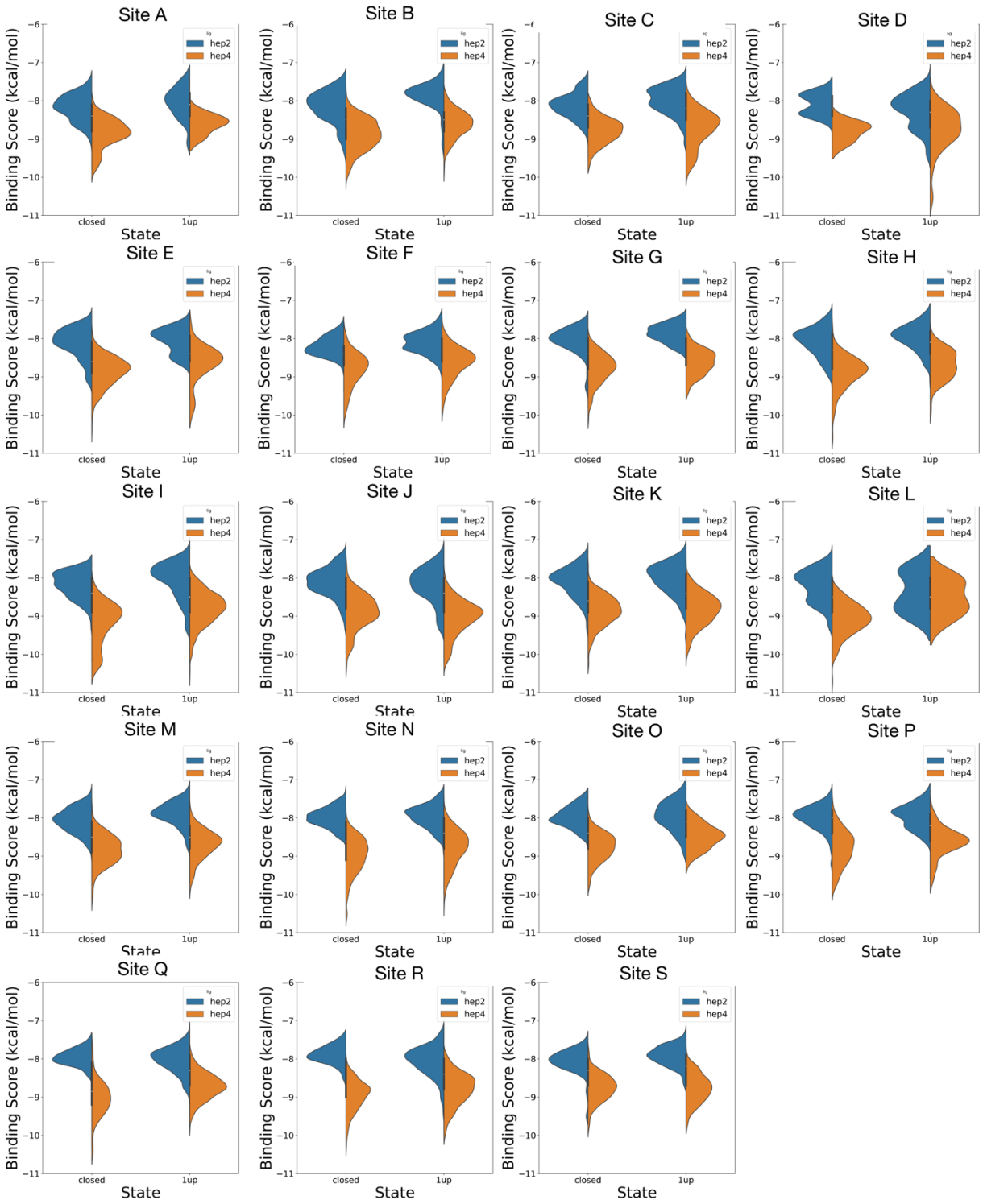

Figure S11: Violin plots demonstrating distribution of AutoDock Vina binding scores for heparin dimer (hep2) and tetramer (hep4) models each binding hotspot across 1up and closed spike structures. Site based distributions of AutoDock Vina binding scores were taken from all three spike variants (WT, Delta, and Omicron) per spike conformation.

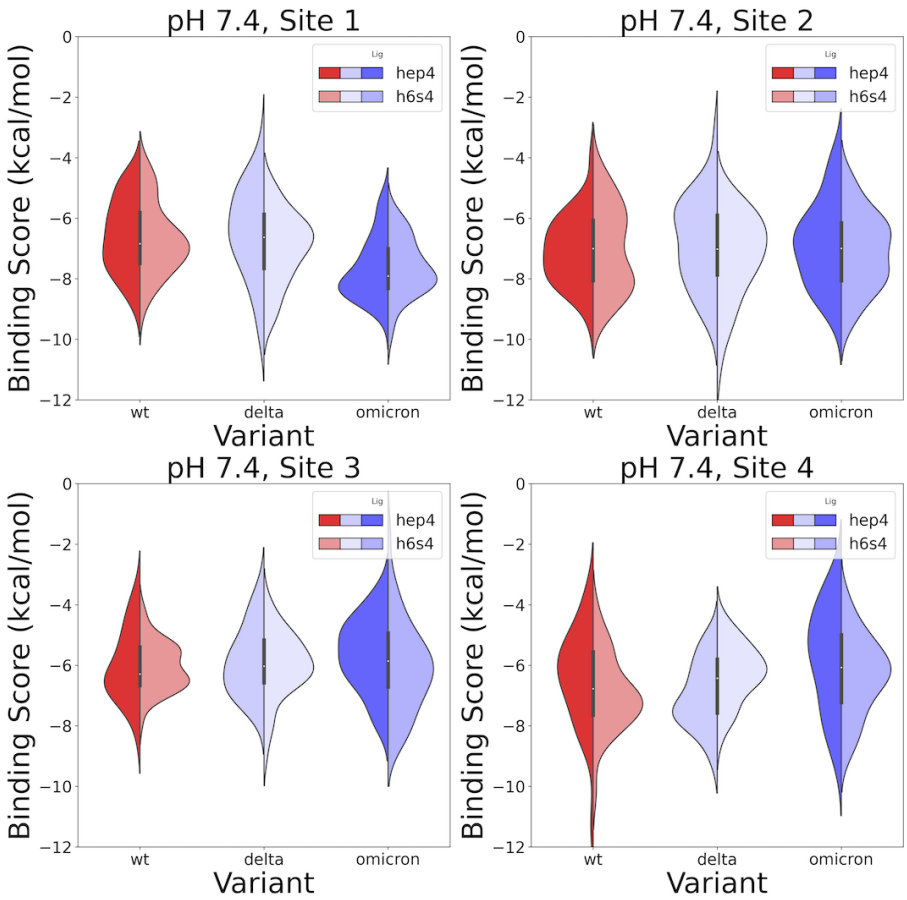

Figure S12: Violin plots illustrating the distribution of binding scores predicted by Schrodinger's Induced Fit Docking protocol in each of the probed sites, for each of the Variants, at pH's 7.4. Site 1 is the RBD Cleft Site, Site 2 is the RBD Patch Site, Site 3 is the Furin Cleavage Site, and Site 4 is the Receptor Binding Motif.

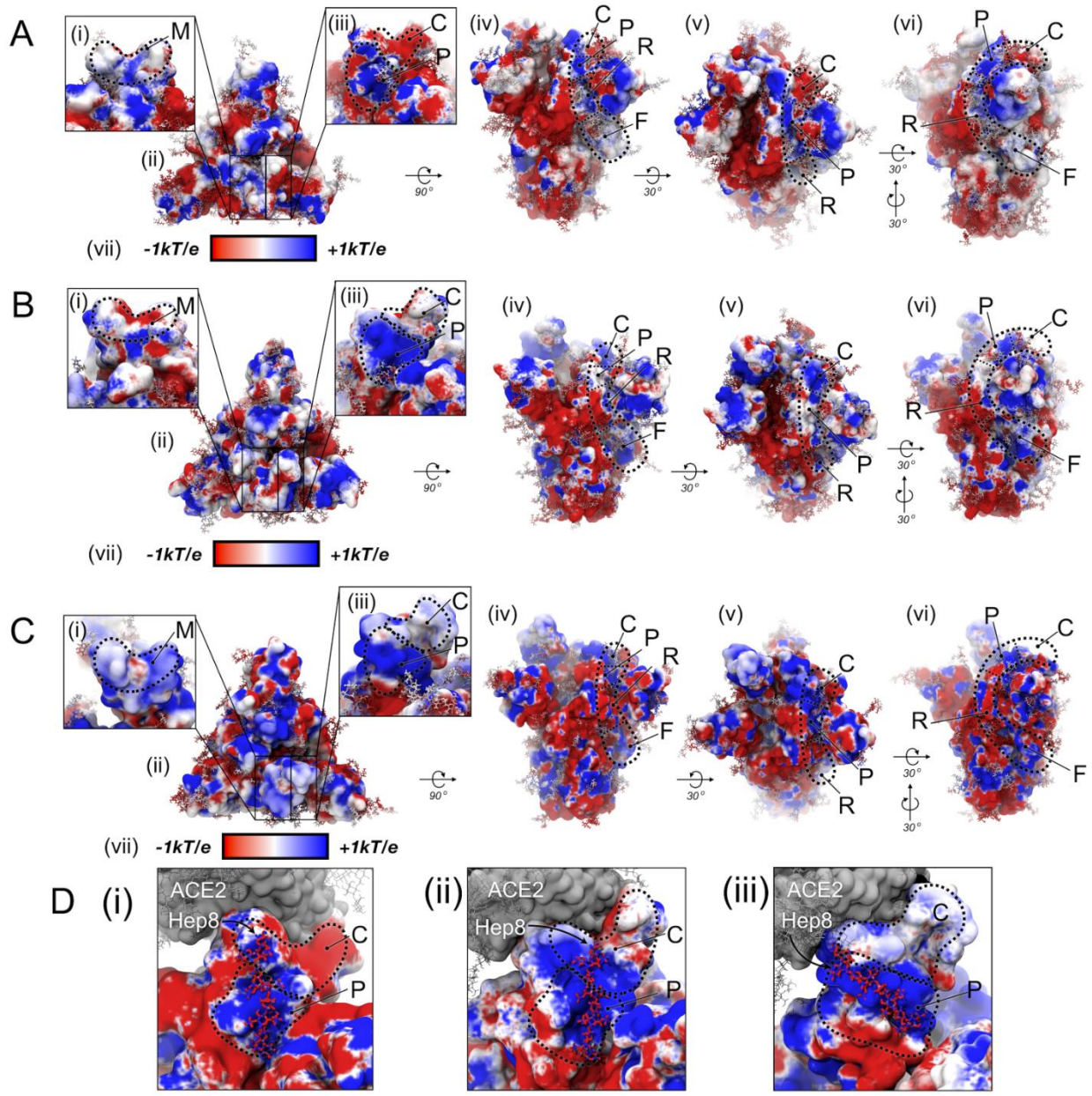

Figure S13: Dynamically-averaged electrostatic potential maps collected from 50 ns of MD simulations for (A) WT, (B) Delta, and (C) Omicron spike proteins in the 1up RBD conformation. For images A-C, labels (i-vii) indicate the following images: a close-up view of the RB**M** site (denoted as M), a top-down view of the spike protein, a close-up view of the RBD **C**left and RBD **P**atch sites (denoted as C and P, respectively), a side view of the spike protein with RBD **C**left, RBD **P**atch, Connecting **R**idge, and **F**CS sites (denoted as C, P, R, and F, respectively) highlighted, a tilted-top-down view of the spike protein with RBD **C**left, RBD **P**atch, and Connecting **R**idge sites (denoted as C, P, and R, respectively) highlighted, a rotated-side view of the spike protein with RBD **C**left, RBD **P**atch, Connecting **R**idge, and **F**CS sites (denoted as C, P, R, and F, respectively) highlighted, and a color bar demonstrating the color ranges for each image and the corresponding calculated electrostatic potential. In all panels, protein surfaces are colored according to average electrostatic potential at each site, ranging from –1 k_BT/e (red) to +1 k_BT/e (blue). (D) Images demonstrating how the SARS-CoV-2 spike can, in the 1up state, accommodate binding of ACE2 (grey surface) at the RBM and a heparin octamer (Hep8) bound to the positively charged RBD Patch site for (i) WT, (ii) Delta, and (iii) Omicron spike proteins. These images were generated by alignment with VMDtools.

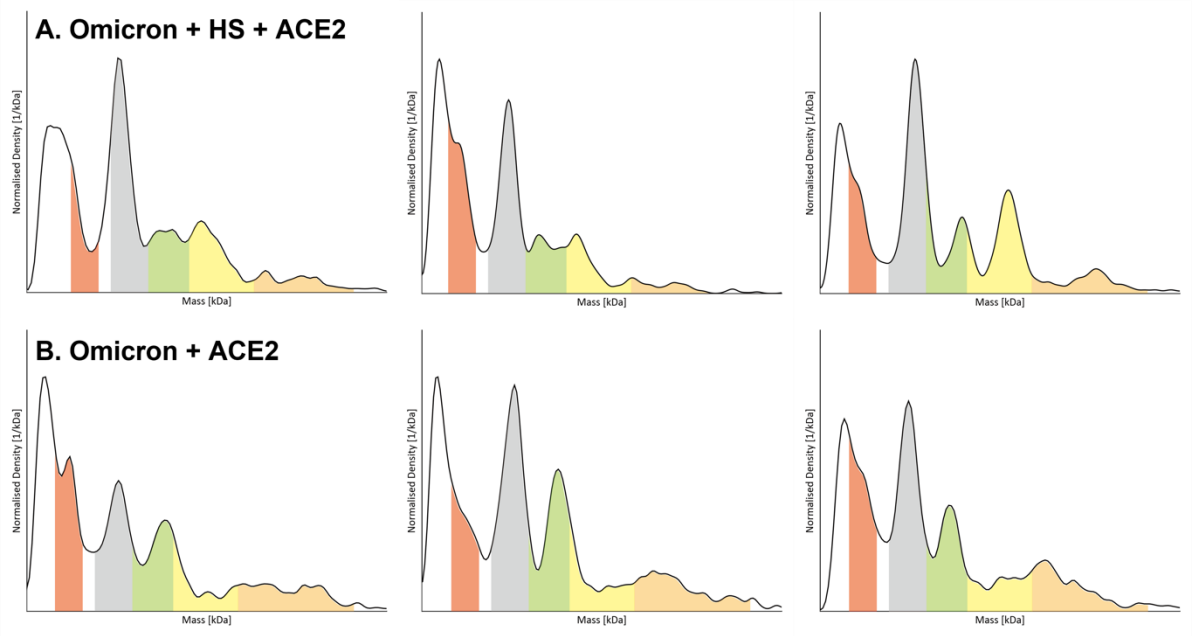

Figure S14: Repetition results of Omicron variant mass photometer. Row (A) Omicron spike + HS + ACE2, and row (B) Omicron spike + ACE2. Mass distribution of Omicron spike (mass range highlighted in grey), dACE2 (mass range highlighted in red), and Possible ternary complexes are grouped in A (green), B (yellow), C (orange) based on their expected mass ranges.

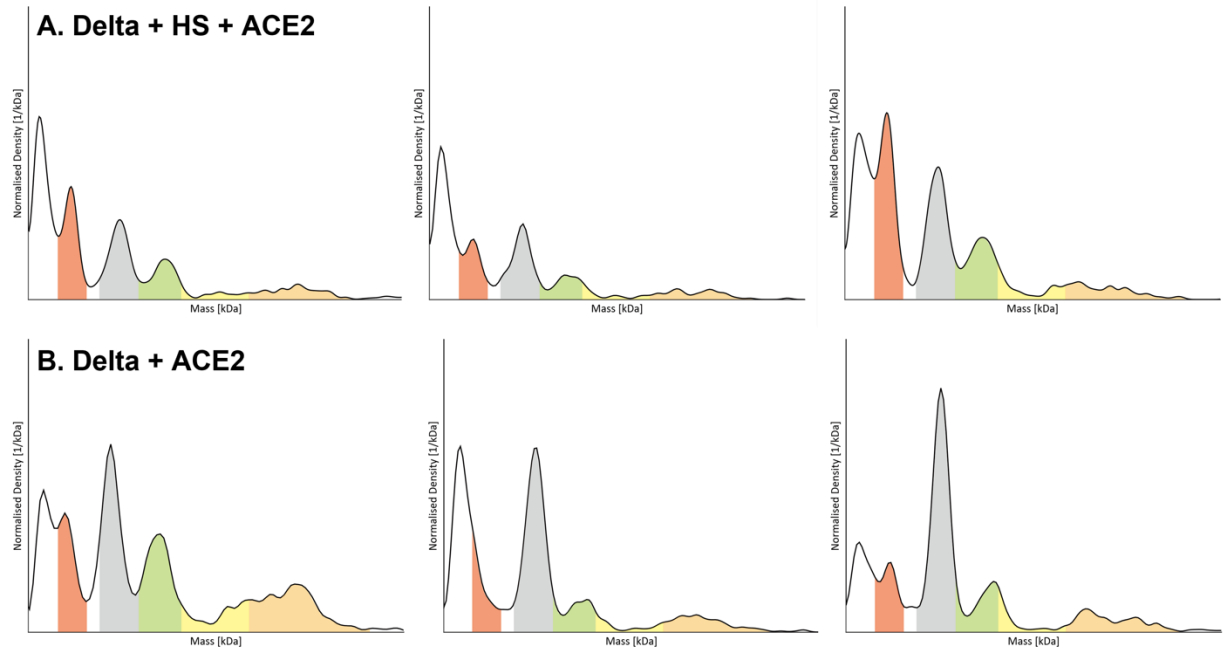

Figure S15: Repetition results of Delta variant mass photometer. Row (A) Delta spike + HS + ACE2, and row (B) Delta spike + ACE2. Mass distribution of Delta spike (mass range highlighted in grey), dACE2 (mass

range highlighted in red), and Possible ternary complexes are grouped in A (green), B (yellow), C (orange) based on their expected mass ranges.

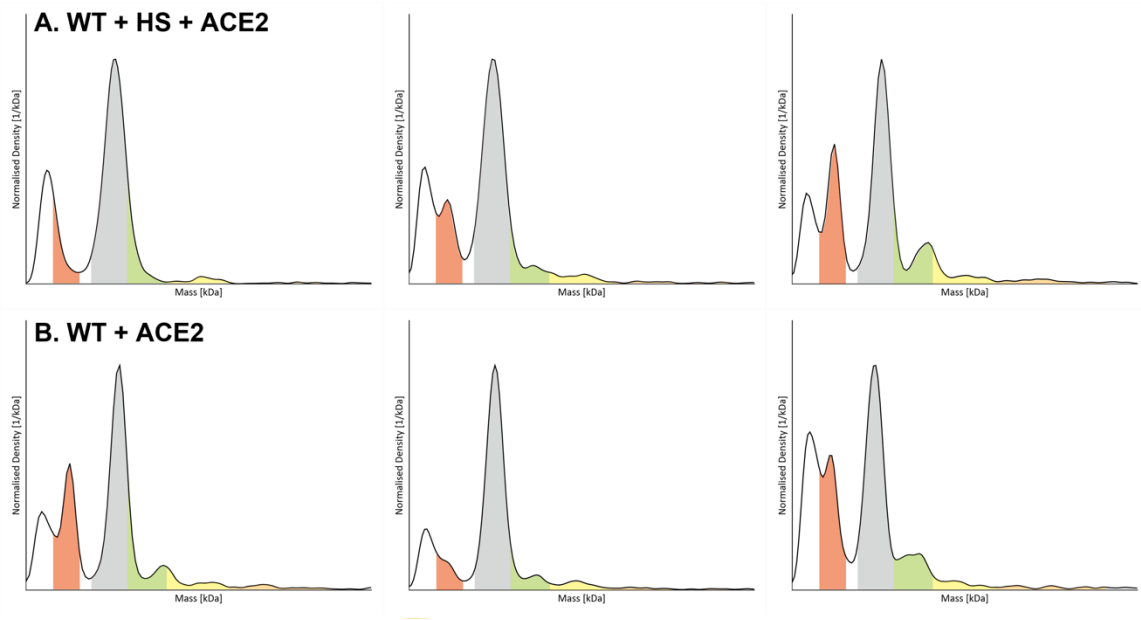

Figure S16: Repetition results of Wild type mass photometer. Row (A) WT spike + HS + ACE2, and row (B) WT spike + ACE2. Mass distribution of WT spike (mass range highlighted in grey), dACE2 (mass range highlighted in red), and Possible ternary complexes are grouped in A (green), B (yellow), C (orange) based on their expected mass ranges.

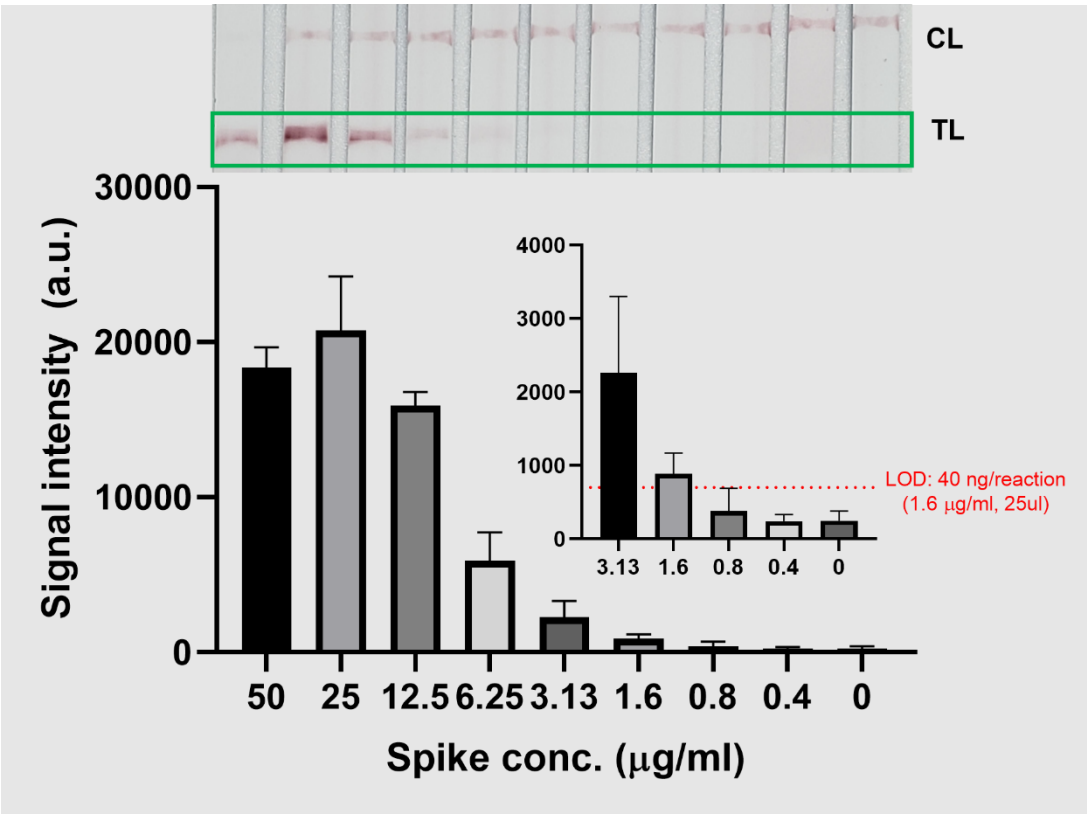

Figure S17: Dose-dependency results of Omicron detection using *GlycoGrip2.0* without signal enhancement in buffer condition. The limit of the detection was calculated by the blank + 3x (Standard deviation of blank). At least three independent tests were performed (n ≥ 3) for *Glycogrip.*

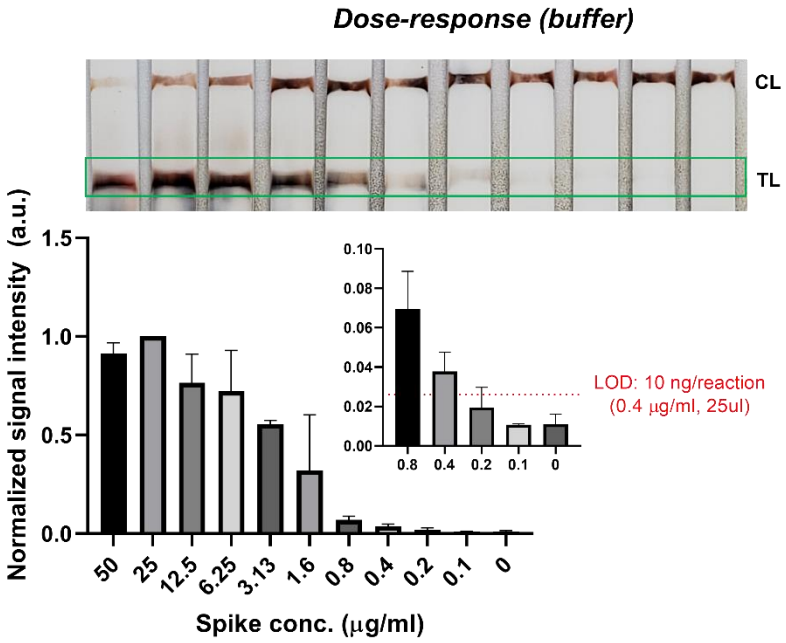

Figure S18: Dose-dependency results of Omicron detection using *GlycoGrip2.0* with signal enhancement in buffer condition. The limit of the detection was calculated by the blank + 3x (Standard deviation of blank). At least three independent tests were performed (n ≥ 3).

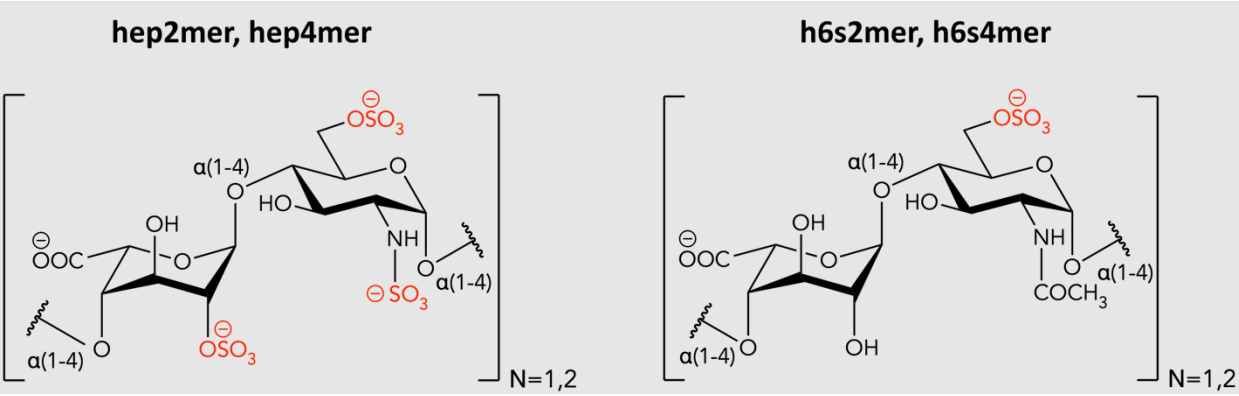

Figure S19: ChemDraws of all molecules modeled and docked in this work. Hep2mer, hep4mer, h6s2mer, h6s4mer.

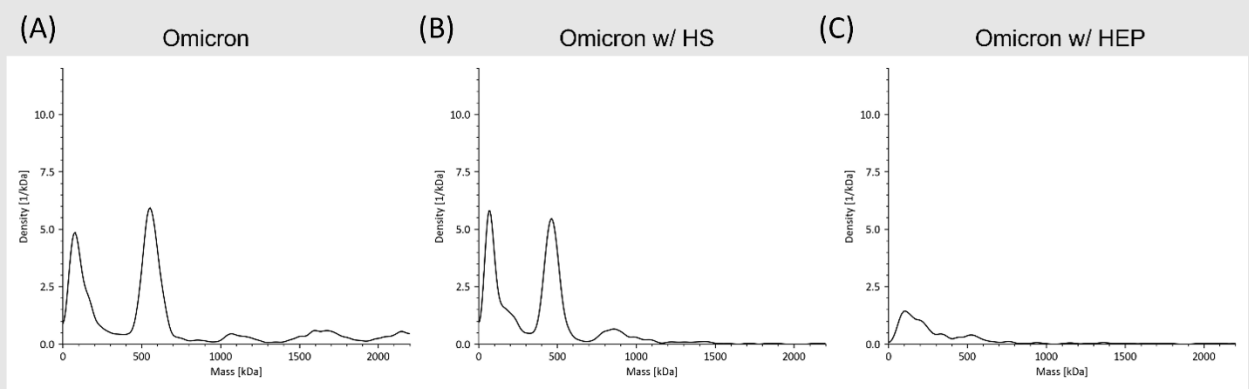

Figure S20: Comparison of the heparin and heparan sulfate for mass photometer. (A) Omicron spike only, (B) Omicron with heparan sulfate, (C) Omicron with heparin. The peak around 500 kDa represent the trimer spike protein. Count number for Omicron only sample at 500 kDa peak was 773, with heparan sulfate was 613, and with heparin was 68 counts.

References:

1. Walls, A.C., Park, Y.-J., Tortorici, M.A., Wall, A., McGuire, A.T., and Veesler, D. (2020). Structure, Function, and Antigenicity of the SARS-CoV-2 Spike Glycoprotein. Cell *181*, 281-292.e286. https://doi.org/10.1016/j.cell.2020.02.058.
2. Bangaru, S., Ozorowski, G., Turner, H.L., Antanasijevic, A., Huang, D., Wang, X., Torres, J.L., Diedrich, J.K., Tian, J.-H., Portnoff, A.D., et al. (2020). Structural analysis of full-length SARS-CoV-2 spike protein from an advanced vaccine candidate. Science *370*, 1089-1094. 10.1126/science.abe1502.
3. Wrapp, D., Wang, N., Corbett, K.S., Goldsmith, J.A., Hsieh, C.-L., Abiona, O., Graham, B.S., and McLellan, J.S. (2020). Cryo-EM structure of the 2019-nCoV spike in the prefusion conformation. Science *367*, 1260-1263. 10.1126/science.abb2507.
4. McCallum, M., Walls, A.C., Sprouse, K.R., Bowen, J.E., Rosen, L.E., Dang, H.V., De Marco, A., Franko, N., Tilles, S.W., Logue, J., et al. (2021). Molecular basis of immune evasion by the Delta and Kappa SARS-CoV-2 variants. Science *374*, 1621-1626. 10.1126/science.abl8506.
5. Gobeil, S.M.C., Henderson, R., Stalls, V., Janowska, K., Huang, X., May, A., Speakman, M., Beaudoin, E., Manne, K., Li, D., et al. (2022). Structural diversity of the SARS-CoV-2 Omicron spike. Molecular Cell *82*, 2050-2068.e2056. https://doi.org/10.1016/j.molcel.2022.03.028.
6. Tortorici, M.A., Beltramello, M., Lempp, F.A., Pinto, D., Dang, H.V., Rosen, L.E., McCallum, M., Bowen, J., Minola, A., Jaconi, S., et al. (2020). Ultrapotent human antibodies protect against SARS-CoV-2 challenge via multiple mechanisms. Science *370*, 950-957. 10.1126/science.abe3354.
7. Casalino, L., Gaieb, Z., Goldsmith, J.A., Hjorth, C.K., Dommer, A.C., Harbison, A.M., Fogarty, C.A., Barros, E.P., Taylor, B.C., McLellan, J.S., et al. (2020). Beyond Shielding: The Roles of Glycans in the SARS-CoV-2 Spike Protein. ACS Central Science *6*, 1722-1734. 10.1021/acscentsci.0c01056.
8. Watanabe, Y., Allen, J.D., Wrapp, D., McLellan, J.S., and Crispin, M. (2020). Site-specific glycan analysis of the SARS-CoV-2 spike. Science *369*, 330-333. 10.1126/science.abb9983.
9. Olsson, M.H.M., Søndergaard, C.R., Rostkowski, M., and Jensen, J.H. (2011). PROPKA3: Consistent Treatment of Internal and Surface Residues in Empirical pKa Predictions. Journal of Chemical Theory and Computation *7*, 525-537. 10.1021/ct100578z.
10. Schrödinger Release 2021-3. Protein Preparation Wizard. Schrödinger, LLC: New York, NY 2021.
11. Humphrey, W., Dalke, A., and Schulten, K. (1996). VMD: Visual molecular dynamics. Journal of Molecular Graphics *14*, 33-38. https://doi.org/10.1016/0263-7855(96)00018-5.
12. Phillips, J.C., Braun, R., Wang, W., Gumbart, J., Tajkhorshid, E., Villa, E., Chipot, C., Skeel, R.D., Kalé, L., and Schulten, K. (2005). Scalable molecular dynamics with NAMD. Journal of Computational Chemistry *26*, 1781-1802. https://doi.org/10.1002/jcc.20289.
13. Phillips, J.C., Hardy, D.J., Maia, J.D.C., Stone, J.E., Ribeiro, J.V., Bernardi, R.C., Buch, R., Fiorin, G., Hénin, J., Jiang, W., et al. (2020). Scalable molecular dynamics on CPU and GPU architectures with NAMD. The Journal of Chemical Physics *153*, 044130. 10.1063/5.0014475.
14. Huang, J., and MacKerell Jr, A.D. (2013). CHARMM36 all-atom additive protein force field: Validation based on comparison to NMR data. Journal of Computational Chemistry *34*, 2135-2145. https://doi.org/10.1002/jcc.23354.
15. Huang, J., Rauscher, S., Nawrocki, G., Ran, T., Feig, M., de Groot, B.L., Grubmüller, H., and MacKerell, A.D. (2017). CHARMM36m: an improved force field for folded and intrinsically disordered proteins. Nature Methods *14*, 71-73. 10.1038/nmeth.4067.
16. Guvench, O., Hatcher, E., Venable, R.M., Pastor, R.W., and MacKerell, A.D., Jr. (2009). CHARMM Additive All-Atom Force Field for Glycosidic Linkages between Hexopyranoses. Journal of Chemical Theory and Computation *5*, 2353-2370. 10.1021/ct900242e.

17. Trott, O., and Olson, A.J. (2010). AutoDock Vina: Improving the speed and accuracy of docking with a new scoring function, efficient optimization, and multithreading. Journal of Computational Chemistry *31*, 455-461. https://doi.org/10.1002/jcc.21334.
18. Morris, G.M., Huey, R., Lindstrom, W., Sanner, M.F., Belew, R.K., Goodsell, D.S., and Olson, A.J. (2009). AutoDock4 and AutoDockTools4: Automated docking with selective receptor flexibility. Journal of Computational Chemistry *30*, 2785-2791. https://doi.org/10.1002/jcc.21256.
19. Michaud-Agrawal, N., Denning, E.J., Woolf, T.B., and Beckstein, O. (2011). MDAnalysis: A toolkit for the analysis of molecular dynamics simulations. Journal of Computational Chemistry *32*, 2319-2327. https://doi.org/10.1002/jcc.21787.
20. Richard J. Gowers, M.L., Jonathan Barnoud, Tyler J. E. Reddy, Manuel N. Melo, Sean L. Seyler, Jan Domański, David L. Dotson, Sébastien Buchoux, Ian M. Kenney, Oliver Beckstein (2016). MDAnalysis: A Python Package for the Rapid Analysis of Molecular Dynamics Simulations. pp. 98–105.
21. Fabian Pedregosa, G.V., Alexandre Gramfort, Vincent Michel, Bertrand Thirion, Olivier Grisel, Mathieu Blondel, Peter Prettenhofer, Ron Weiss, Vincent Dubourg, Jake Vanderplas, Alexandre Passos, David Cournapeau, Matthieu Brucher, Matthieu Perrot, Édouard Duchesnay (2011). Scikit-learn: Machine Learning in Python. Journal of Machine Learning Research *12*, 2825-2830.
22. Kim, S.H., Kearns, F.L., Rosenfeld, M.A., Casalino, L., Papanikolas, M.J., Simmerling, C., Amaro, R.E., and Freeman, R. (2022). GlycoGrip: Cell Surface-Inspired Universal Sensor for Betacoronaviruses. ACS Central Science *8*, 22-42. 10.1021/acscentsci.1c01080.
23. Shrake, A., and Rupley, J.A. (1973). Environment and exposure to solvent of protein atoms. Lysozyme and insulin. Journal of Molecular Biology *79*, 351-371. https://doi.org/10.1016/0022-2836(73)90011-9.
24. Schrodinger Release 2022-3. Induced Fit Docking Protocol. Schrödinger, LLC: New York, NY 2022.
25. Lu, C., Wu, C., Ghoreishi, D., Chen, W., Wang, L., Damm, W., Ross, G.A., Dahlgren, M.K., Russell, E., Von Bargen, C.D., et al. (2021). OPLS4: Improving Force Field Accuracy on Challenging Regimes of Chemical Space. Journal of Chemical Theory and Computation *17*, 4291-4300. 10.1021/acs.jctc.1c00302.
26. Schrödinger Release 2021-3. LigPrep. Schrödinger, LLC: New York, NY 2021.
27. Dolinsky, T.J., Nielsen, J.E., McCammon, J.A., and Baker, N.A. (2004). PDB2PQR: an automated pipeline for the setup of Poisson–Boltzmann electrostatics calculations. Nucleic Acids Research *32*, W665-W667. 10.1093/nar/gkh381.
28. Dolinsky, T.J., Czodrowski, P., Li, H., Nielsen, J.E., Jensen, J.H., Klebe, G., and Baker, N.A. (2007). PDB2PQR: expanding and upgrading automated preparation of biomolecular structures for molecular simulations. Nucleic Acids Research *35*, W522-W525. 10.1093/nar/gkm276.
29. Huber, G.A., and McCammon, J.A. (2010). Browndye: A software package for Brownian dynamics. Computer Physics Communications *181*, 1896-1905. https://doi.org/10.1016/j.cpc.2010.07.022.
30. Huber, G.A., and McCammon, J.A. (2019). Brownian Dynamics Simulations of Biological Molecules. Trends in Chemistry *1*, 727-738. https://doi.org/10.1016/j.trechm.2019.07.008.
31. Jurrus, E., Engel, D., Star, K., Monson, K., Brandi, J., Felberg, L.E., Brookes, D.H., Wilson, L., Chen, J., Liles, K., et al. (2018). Improvements to the APBS biomolecular solvation software suite. Protein Science *27*, 112-128. https://doi.org/10.1002/pro.3280.
32. Baker, N.A., Sept, D., Joseph, S., Holst, M.J., and McCammon, J.A. (2001). Electrostatics of nanosystems: Application to microtubules and the ribosome. Proc National Acad Sci *98*, 10037-10041. 10.1073/pnas.181342398.
33. Holst, M. (2001). Adaptive Numerical Treatment of Elliptic Systems on Manifolds. Advances in Computational Mathematics *15*, 139-191. 10.1023/A:1014246117321.

34. Holst, M.J., and Saied, F. (1995). Numerical solution of the nonlinear Poisson–Boltzmann equation: Developing more robust and efficient methods. Journal of Computational Chemistry *16*, 337-364. https://doi.org/10.1002/jcc.540160308.
35. Bank, R.E., and Holst, M. (2003). A New Paradigm for Parallel Adaptive Meshing Algorithms. SIAM Review *45*, 291-323. 10.1137/S003614450342061.
36. Holst, M., and Saied, F. (1993). Multigrid solution of the Poisson—Boltzmann equation. Journal of Computational Chemistry *14*, 105-113. https://doi.org/10.1002/jcc.540140114.
37. Chavanis, P.-H. (2019). The Generalized Stochastic Smoluchowski Equation. Entropy *21*. 10.3390/e21101006.
38. Votapka, L.W., and Amaro, R.E. (2015). Multiscale Estimation of Binding Kinetics Using Brownian Dynamics, Molecular Dynamics and Milestoning. PLOS Computational Biology *11*, e1004381. 10.1371/journal.pcbi.1004381.
39. Yan, R., Zhang, Y., Li, Y., Xia, L., Guo, Y., and Zhou, Q. (2020). Structural basis for the recognition of SARS-CoV-2 by full-length human ACE2. Science *367*, 1444-1448. 10.1126/science.abb2762.
40. Barros, E.P., Casalino, L., Gaieb, Z., Dommer, A.C., Wang, Y., Fallon, L., Raguette, L., Belfon, K., Simmerling, C., and Amaro, R.E. (2021). The flexibility of ACE2 in the context of SARS-CoV-2 infection. Biophysical Journal *120*, 1072-1084. https://doi.org/10.1016/j.bpj.2020.10.036.
41. Panferov, V.G., Safenkova, I.V., Varitsev, Y.A., Drenova, N.V., Kornev, K.P., Zherdev, A.V., and Dzantiev, B.B. (2016). Development of the sensitive lateral flow immunoassay with silver enhancement for the detection of Ralstonia solanacearum in potato tubers. Talanta *152*, 521-530. https://doi.org/10.1016/j.talanta.2016.02.050.
42. Lee, J.-H., Choi, M., Jung, Y., Lee, S.K., Lee, C.-S., Kim, J., Kim, J., Kim, N.H., Kim, B.-T., and Kim, H.G. (2021). A novel rapid detection for SARS-CoV-2 spike 1 antigens using human angiotensin converting enzyme 2 (ACE2). Biosensors and Bioelectronics *171*, 112715. https://doi.org/10.1016/j.bios.2020.112715.
43. Baker, A.N., Richards, S.-J., Guy, C.S., Congdon, T.R., Hasan, M., Zwetsloot, A.J., Gallo, A., Lewandowski, J.R., Stansfeld, P.J., Straube, A., et al. (2020). The SARS-COV-2 Spike Protein Binds Sialic Acids and Enables Rapid Detection in a Lateral Flow Point of Care Diagnostic Device. ACS Central Science *6*, 2046-2052. 10.1021/acscentsci.0c00855.
44. Lee, J.-H., Lee, Y., Lee, S.K., Kim, J., Lee, C.-S., Kim, N.H., and Kim, H.G. (2022). Versatile role of ACE2-based biosensors for detection of SARS-CoV-2 variants and neutralizing antibodies. Biosensors and Bioelectronics *203*, 114034. https://doi.org/10.1016/j.bios.2022.114034.